



ECOLE DOCTORALE 139 CONNAISSANCE, LANGAGE, MODELISATION
Doctorat en Sciences pour l'Ingénieur
Spécialité Mécanique

Federico Miglioretti

**Développement de un modèle avancé mono dimensionnel et multi
domaine pour l'étude de 'smart wing'**

Thèse dirigée par Pr. Erasmo Carrera, Pr. Olivier POLIT

Soutenue le 11 avril 2013

Jury :

Pr. Erasmo CARRERA
Pr. Olivier POLIT
Pr. Laurent GALLIMARD
Pr. Francesco LAROCCA

Da mettere qualcosa

Acknowledgements

Summary

In the field of aeronautics, shape morphing has been used to identify those aircraft that undergo certain geometrical changes to enhance or adapt to their mission profile. Different from the classical solution the shape morphing required: distributed high-power density actuation, structural mechanization, flexible skins, and control law development. In these scenarios, models able to capture the insertion of new generation sensors and actuators, and able to minimize the computational cost become very interesting. This work tries to address two different aspects of the problem. In the first part the following question has been explored: for a given problem, geometry, loading, boundary condition etc... which is the most accurate model in terms of results fidelity with the lowest computational cost? Two different approaches have been used to give an answer. The Best Plate Theory Diagram (BPTD) has been drawn. Through the BPTD it is possible, for a given problem, to identify those models with the lowest computational time and a good results fidelity. An advanced mono-dimensional multi-field FEM model is presented in the second part of the thesis. The model is able to capture the insertion of piezo-electric elements in composite wings. It has been developed starting from the Carrera Unified Formulation and from the electro-mechanical constitutive equation. Comparison with the bibliography has been done in order to validate the results.

Sommario

Nel campo dell'aeronautica il termine shape morphing identifica quei velivoli in grado di apportare determinati cambiamenti geometrici al fine di adattarsi a diversi profili di missione. Diversamente dalle soluzioni convenzionali la progettazione di velivoli shape morphing richiede : un'attuazione distribuita, uno skin flessibile in grado di permettere le deformazioni e delle leggi di controllo. Divengono quindi di notevole interesse modelli in grado di cogliere l'inserzione di attuatori e sensori di nuova generazione all'interno dell'ala, e di esibire al contempo un basso costo computazionale. Nel lavoro presentato in questa tesi vengono trattati entrambi gli aspetti. Nella prima parte si è andati a dare una risposta alla seguente domanda: per un dato problema, geometria, condizioni di carico, etc..., qual è il modello più accurato, in termini di fedeltà dei risultati, che presenta il minor costo computazionale? Il problema è stato affrontato attraverso due differenti approcci, che hanno portato alla creazione della "Best Plate Theory Curve", attraverso la quale è possibile, per un dato problema, identificare il modello più idoneo in termini di fedeltà dei risultati e di costo computazionale. Nella seconda parte del lavoro viene presentato un modello mono-dimensionale multi-campo avanzato in grado di cogliere l'inserzione di elementi piezo-elettrici in ali in materiale composito. Questo elemento è stato sviluppato partendo dalla Carrera Unified Formulation e dalle equazioni costitutive elettromeccaniche. Sono state effettuate poi delle validazioni attraverso confronti con la bibliografia.

Résumé

Contents

- 1 Smart Wing** **15**
 - 1.1 Introduction 15
 - 1.2 Adaptive Wing Technology 15
 - 1.2.1 Variable camber 18
 - 1.2.2 Complete airfoil adaptation 29
 - 1.2.3 Actuation systems 32
 - 1.3 Present work objectives and outline 34

- 2 Reduced Finite models** **35**
 - 2.1 Introduction 35
 - 2.2 Geometry and material arrays 37
 - 2.3 Carrera Unified Formulation - 2D Formulation 40
 - 2.4 FE Governing Equations 42
 - 2.5 Approach for Evaluating Various Plate Models 44
 - 2.5.1 Influence of each terms. 44
 - 2.5.2 Genetic optimization method 46

- 3 Electro-mechanical formulation** **51**
 - 3.1 Piezoelectri materials 51
 - 3.2 Generalized Hooke’s law 52
 - 3.3 Constitutive equations for piezoelectric problems 56
 - 3.4 Carrera Unified Formulations - 1D Formulations 59
 - 3.4.1 Lagrange polynomial 60
 - 3.5 Finite Element 61
 - 3.5.1 Stiffness Matrix 62
 - 3.5.2 Mass Matrix 63
 - 3.5.3 Loading Vector 66

- 4 Results and discussion** **67**
 - 4.1 Influence of each term 67
 - 4.1.1 Isotropic Plate 67
 - 4.1.2 Orthotropic Plate 85
 - 4.2 Genetic optimization method 107
 - 4.2.1 Laminated Plates 107
 - 4.2.2 Sandwich plate 116

4.3	Piezoelectric analysis	120
5	Conclusion	129
5.0.1	Outline and contribution to the literature	129

Chapter 1

Smart Wing

1.1 Introduction

In the field of aeronautics, shape morphing has been used to identify those aircraft that undergo certain geometrical changes to enhance or adapt to their mission profile. In spite of there is not a clear definition for an enabling shape morphing, it is a general agreement that the conventional hinged control surfaces or high lift device, such as flap or slat that provide discrete geometry changes cannot be considered as morphing. No matter how one would choose to define the wing morphing, Reich and Sanders (1) listed the major challenges of shape morphing aircraft design to be: the requirement for distributed high-power density actuation, structural mechanization, flexible skins, and control law development. In this chapter we focus our attention on adaptive wing schemes of varying complexity including the adaptation of complete wing (airfoils), the adaptation of individual component, such as variable-camber leading and trailing edge. A collecting of articles relating to smart wing solution is presented to illustrate the state of art in this field.

1.2 Adaptive Wing Technology

As it is possible to read in the *Adaptive Structures - Engineering Application book* (2), in the framework of the synthesis of a shape-adaptable structural system, mechanical design deals with the task of choosing the properties and distribution of load-carrying material and actuator in order to fulfil:

- a set of deformability requirements specifying the geometrical changes which system under consideration must be able to perform;
- a set of stiffness requirements which define the allowed deviations from the desired shape under given loads;
- strength requirements which specify the load to be carried by the system without damage;
- activability requirements which state that the desired deformation is achievable by loading through the actuator system; and possibly



Figure 1.1 Smart wing mechanism

- a set of further requirements - mostly coupled with another and related to possible payload requirements - which define boundaries for the system's weight and energy consumption.

Of course, mechanical design as definite above does not constitute a closed task since the exact definition of the single requirements is not a priori available, but is somehow part of the unknowns of the whole synthesis problem. For this reason, mechanical issues cover only a limited portion of the complexity involved in the global design process (essential questions like, for instance, sensor and control design or energy reserve allocation are not considered in this context). Still, the issue of mechanical design is highly representative, since it concerns a component with a strong impact on the overall system weight and therefore involves some crucial challenges of shape-morphing flight. An example of shape-morphing complexity it can possibly find in the case of the classical shape adaptation problem: the realisation of aerofoils with changeable camber for the purpose of regulating lift (see Fig. 1.1). A substantial conflict occurs between the deformability requirements, defining the change in camber which must be allowed by the airfoil, and the stiffness requirement, which limits the shape changes under load. The conventional solution based on an actuated flap implements an almost complete separation between the task of producing the desired geometry changes and that of carrying loads. A rigid-body mechanism (the flap and the fixed part of the airfoil, mutually connected by a hinge) guarantees unrestricted deformability in one single degree of freedom; all the remaining degrees of freedom can then be provided with sufficient load-carrying capabilities (strength and stiffness) without interacting with the system's deformability. In this way, the conflict between load-carrying capabilities and deformability is restricted to the single degree of freedom of the rigid-body mechanism and can be easily solved by providing the actuator with proper strength and (active or passive) stiffness. By coupling a larger number of degrees of freedom and harmonising the contribution of active and passive elements, alternative solutions are possible. Such systems show typically a better performance (in particular, smoother geometry changes and weight savings through load distribution) but are definitely more complex to design. Conciliating the conflicting requirements of deformability, load-carrying capability and low weight is the dominant issue in the mechanical design of shape-adaptable systems. While established technologies and disciplines which successfully deal with the fulfilment of just two out of the three requirements are presently available, the simultaneous accomplishment of all three of them represents a real challenge. Filling this gap is likely to keep busy a large number of researchers in the near future. Even though the coupling with the actuator system can play an important role in this context, in particular with regard to stiffness aspects, the above-addressed challenge concerns primarily the passive part of the system. Let us now look at the diagram in Figure 1.2. The first "binary" discipline is lightweight design, which covers a large spectrum of procedures, criteria and techniques for the analysis and synthesis of structures with a high strength-to-weight ratio. Lightweight structures, however, are typically provided with a low degree of deformability. This is a direct consequence

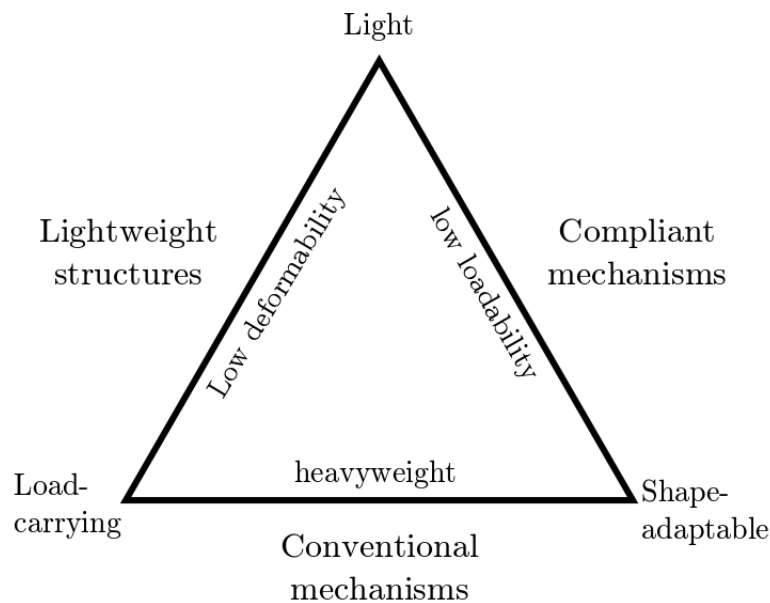


Figure 1.2 Adaptive Structures Diagram

of the key principle of lightweight design, which tends to realise a stress state with mainly membrane loading and to avoid bending and torsion loading of single components. Under certain conditions, maximising stiffness is equivalent to minimising weight and this criterion is often used as the basis of structural optimisation procedures. The second discipline which is capable of joining two of the three above-mentioned requirements is machine engineering, or, in particular, the science of conventional mechanisms. They are highly deformable and able to carry high loads, but far from being lightweight optimised. Finally, a third speciality deals with the remaining couple of requirements: the science of compliant systems, i.e. systems designed to reach a given level of deformability by exploiting structural strain. They offer an excellent combination of deformability and low weight, but are limited, at the present state of the art, in their load-carrying capability: systems with lumped compliance, provided with cut-outs or other kinds of solid-state hinges, typically suffer from stress concentration effects in the compliant regions, whereas systems with spread compliance are more difficult to control owing to their low stiffness in a large number of degrees of freedom. Compliant systems will also be addressed later in more detail, since they are likely to provide the basis for the future development of light, high-load, high-deformability systems. In the course of the history of aeronautics and all the way till today, a large number of inventions were elaborated which aimed at realising smooth shape changes as well as at increasing the number of controllable geometry degrees of freedom on the basis of conventional mechanisms, but they generally turned out not to be feasible. Still, the resulting patent literature offers an excellent insight into how significant this issue has always been to aircraft engineers and which kinds of advantages were expected from airfoils with enhanced geometry management. In the following paragraph we shall accordingly discuss adaptive wing scheme of varying complexity. Emphasis will be placed on the possible structural realization and penalties associate, we also consider the aerodynamic and load control benefits.

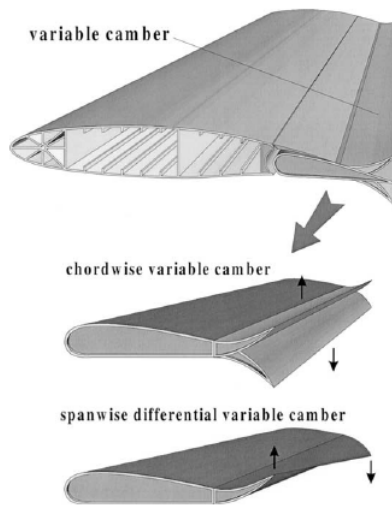


Figure 1.3 Chordwise and spanwise differential camber variation of Fowler flaps with an enhanced cambering function.

1.2.1 Variable camber

Changing the airfoil camber is the most investigated approach of shape morphing. The airfoil camber can be uniformly changed along the span in a similar manner to the rotation of the ailerons. It is of special interest to achieve a chord-wise and span-wise differential camber variation with one structural system providing a smooth contour having no additional gaps. The camber variation concentrates on the trailing edge since under aerodynamic as well as structural aspects this region has the highest efficiency. On civil transport aircraft the Fowler flaps and ailerons are positioned in this region. Therefore, it is important to develop a cambering system that on the one hand can be used to enhance the Fowler flaps by an additional cambering function and on the other hand enables a complete substitution of an aileron. Fig. 1.3 shows this principle for a Fowler flap with enhanced cambering. The cambering system should also be constructed such that during its actuation the structural stiffness does not change. This ensures that sudden changes in loading caused by a gust, for example, lead to failure. When the Fowler flaps are enhanced by an additional cambering function they should still retain their primary function as a high-lift device. If the ailerons are replaced with such a cambering system the actuators have to be positioned inside the structure. In addition, it is important to be able to adapt the profile contour to different types of aerodynamic and geometric requirements for the median line. Considering the remarks made above, the following basic requirements can be defined:

- the structural system has to be suitable for replacement and enhancement of a given flap system;
- a chord wise and span-wise differential camber variation has to be achieved with one structural system;
- a smooth contour having no additional gaps has to be provided;

- the actuators have to be integrated into the flap structure;
- the profile contour has to be able to be adapted to different types of aerodynamic and geometric requirements;
- the structural stiffness is not allowed to change during actuation.

Both chord-wise and span-wise differential camber variation are expected to have various effects on aerodynamic and structural efficiency. The following improvements over fixed geometry wings are expected:

- higher aerodynamic efficiency due to optimized lift/drag (L/D) ratio leads to an extended cruise range and reduction in fuel consumption;
- improved operational flexibility by shifting the maximum L/D ratio to higher values;
- extended buffet boundary enlarges the operative range and reduces structural weight;
- reduction of wing root bending moment leads to a reduction of structural weight;
- increased stretch potential leads to a significant reduction of development costs.

Alternatively, gradual changes of the airfoil camber along the span can create controllable twisting of the wing. The necessary camber change is pursued either by the reconfiguration of the underlying structure (e.g. ribs) or the morphing of the wing skin. Here the following classification is used for the airfoil camber change methods: (a) using internal mechanisms, (b) piezoelectric actuation, and (c) shape memory alloy actuation.

Camber change by using classical kinematics

During the 1980's, the Flight Dynamics Laboratory conducted a flight demonstration program called the Mission Adaptive Wing (MAW), in which a F-111 was retrofitted with wings whose camber could be actively varied using hydraulic actuators (Smith et.al. (3), Powers et.al. (4), and Thornton (5)). Using conventional rigid-link mechanisms and fibreglass flex-panels, adaptive wing geometry proved its aerodynamic superiority over conventional leading and trailing-edge flaps. The flap system consisted of six independent trailing-edge flap segments (three per wing) and two leading edge flap segments (one per wing) providing smooth, continuously variable wing camber by using flexible fibreglass skins on the upper and sliding panels for the lower surface.

MAW results : Drag polar optimization $F_{cruise/maneuver}$ camber control

An extensive wind-tunnel and flight-test program has been performed with the MAW aircraft (AFTI) to predict the aerodynamic performance benefits of the smooth-skin variable camber wing. For the former, test conditions covered a Mach number range of $M = 0.25$ to 2.50 at Reynolds numbers ranging from $Re = 6e6$ to $26e6/m$. Configuration variables included wing sweep, discrete variable-camber flap deflections and angle of attack. Adaptation implies here that at any given lift coefficient there is an optimum camber setting that produces minimum drag. The locus of combined variable-camber leading- and trailing-edge flap deflections providing minimum drag as function of lift constitutes the variable-camber drag polar as shown



NASA Dryden Flight Research Center Photo Collection
<http://www.dfrc.nasa.gov/gallery/photo/index.html>
 NASA Photo: EC86-33385-002 Date: February 27, 1986

AFTI F-111 Mission Adaptive Wing (MAW) in flight

Figure 1.4 The AFT/F-111 in flight with flaps deflected.

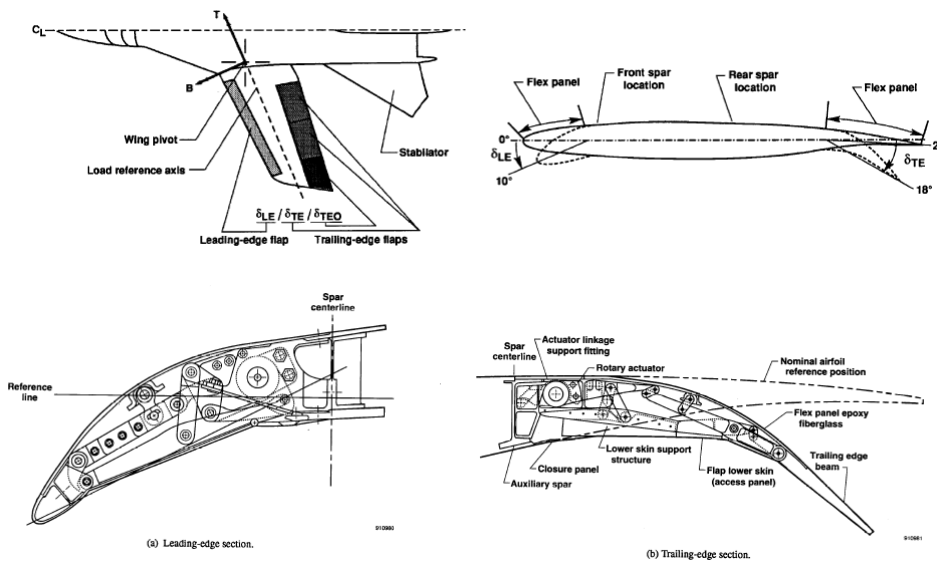


Figure 1.5 MAW Technology

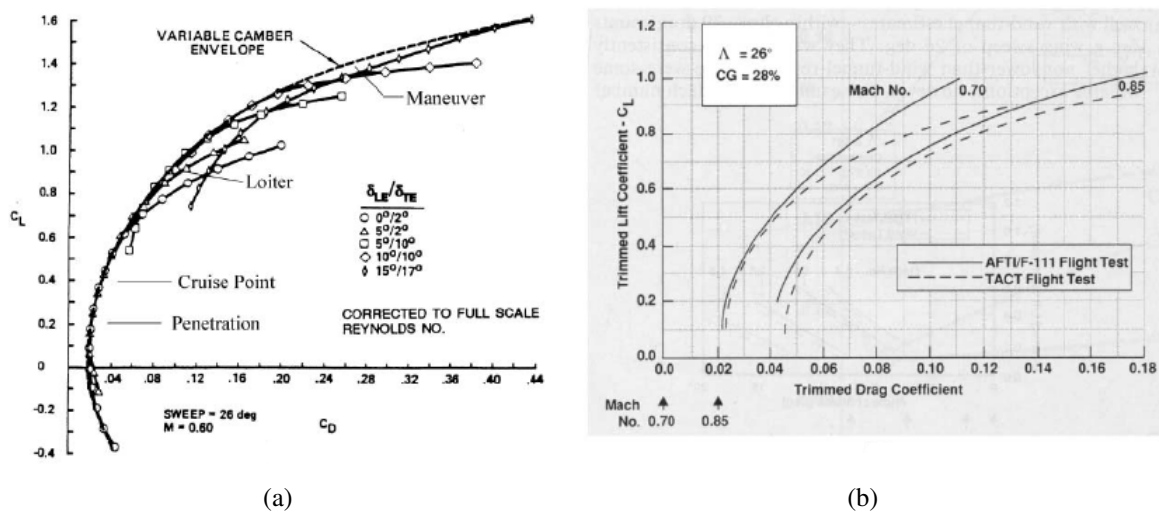


Figure 1.6 Polar

in Figure 1.6 (a): in the present example ($M = 0.60$), there is obviously only little improvement due to variable camber at the lower lift coefficients, $C_L < 0.60$; but noticeable gains at higher lift. Also indicated in Figure 1.6 (a) are lift levels corresponding to the aircraft flight envelope. Especially at manoeuvre conditions, i.e., conditions where the fixed-wing aircraft would be completely stalled, considerable improvements are possible due to variable camber. The improvements are also demonstrated by flight test results obtained for the variable-camber (AFTI/F-111) and the fixed-wing (TACT) aircraft, respectively, at two Mach numbers, Figure 1.6 (b): appreciable drag reductions are possible due to the MAW at the higher lift coefficients. It should be noted that the drag reduction in the cruise regime, i.e., $C_L = 0.40$; $M = 0.85$; is essentially due to the still more refined supercritical airfoil design of the AFTI wing, whereas the large drag reduction at the higher lift coefficients is entirely due to the application of the variable-camber concept.

MAW results : Manoeuvre-load control (MLC)

Manoeuvre-load control is the technique of changing the span-wise lift distribution of the wing to move the center of lift inboard thus reducing the wing bending moments. This can be accomplished by changing the wing span-wise camber distribution, which the AFTI aircraft is well able to do by corresponding deflections of the three independent trailing-edge manoeuvre flaps provided on each wing, Fig. 1.7. Corresponding results obtained in actual flight tests with the AFTI aircraft at $M = 0.80$ are presented in Fig. 1.7 for three flap settings, namely, $\delta LE = \delta TE$ (inboard and mid-span)/ δTE (outboard) = 5/10/10, 5/10/4 and 5/10/ - 1. Here, 5/10/10 corresponds to the base-line (elliptic) configuration. One observes that the wing-root bending moment, which is the most critical parameter in limiting wing loads, is considerably reduced by the load redistribute on assuming the same equivalent load factor 'ge', or, in other words, the load factor can be increased by $\Delta ge = 1$ for the same wing root bending moment noticeably improving manoeuvrability. Such control can, of course, also be applied to a transport aircraft to raise the buffet boundary or to eliminate gust loads.

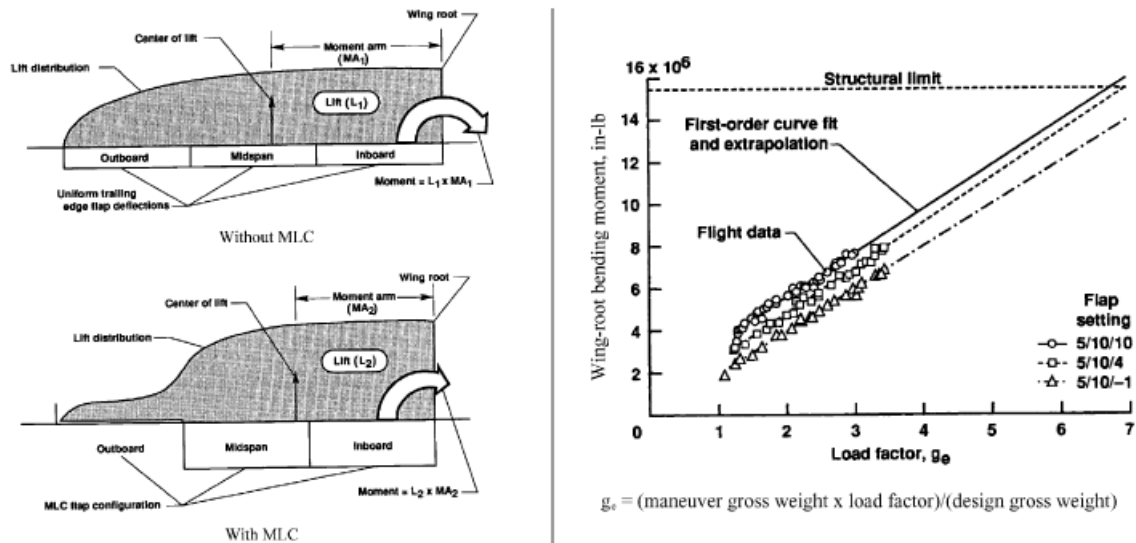


Figure 1.7 Wing root bending moment

Unfortunately, drawbacks in the mechanical design resulted in weight penalties and overall system complexity, significantly offsetting the aerodynamics and load control benefits and prohibited further development.

Recent solutions

In more recent paper new mechanical devices, lighter than the previous, have been developed in order to realize the adaptive wing. In the work of Hans Peter Monner (6), is described the design of a flexible flap system for an adaptive wing to be used in civil transport aircraft that allows both a chord-wise as well as span-wise differential variation of the wing camber for mission duration. As shown in Fig. 1.8, the basic concept for the design of the flexible Fowler flaps consists of replacing the stiff inflexible rib elements reaching into the flexible section (dark gray) by active deformable elements with high stiffness. This means the skin fields must then be able to glide on the flexible ribs. The basic design of the front fixed part (light gray) is changed as little as possible to avoid a totally new design concept for the fixed flap section. The flexible ribs were realized by combining separate plate like elements with revolute joints having the kinematics described in figure 1.9 (a). Figure 1.9 (b) represents one rib of the flexible section. Each rib only has to be actuated at one single point. The rotation of the driven element is transferred gradually from element to element by the kinematics, and this way provides the wanted rib contour. The kinematics will be described by referring to the first three elements (1 to 3): an actuator (7) is supported by the fixed first element (1) which represents the continuation of the rib in the front fixed section. The actuator (7) drives a second element (2) which is attached to the first element (1) by a revolute joint (8). The second element (2), too, is connected to the third element (3) by a revolute joint (9). In addition the third element (3) is connected to the first one (1) by a prismatic joint (13). By putting the actuator (7) into motion the second element (2) rotates about revolute joint (8). Due to revolute joint (9) the third element (3) rotates about revolute joint (8), too, and is supported by the first element (1) in prismatic joint (13). This way the third element

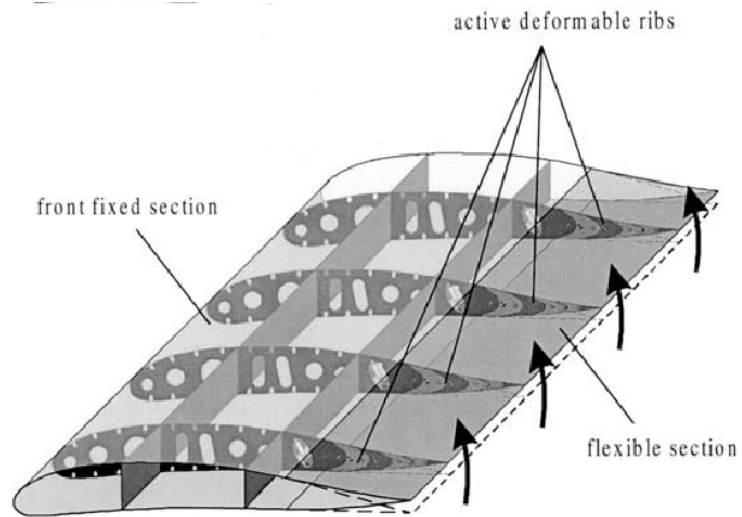


Figure 1.8 Load control by means of variable camber

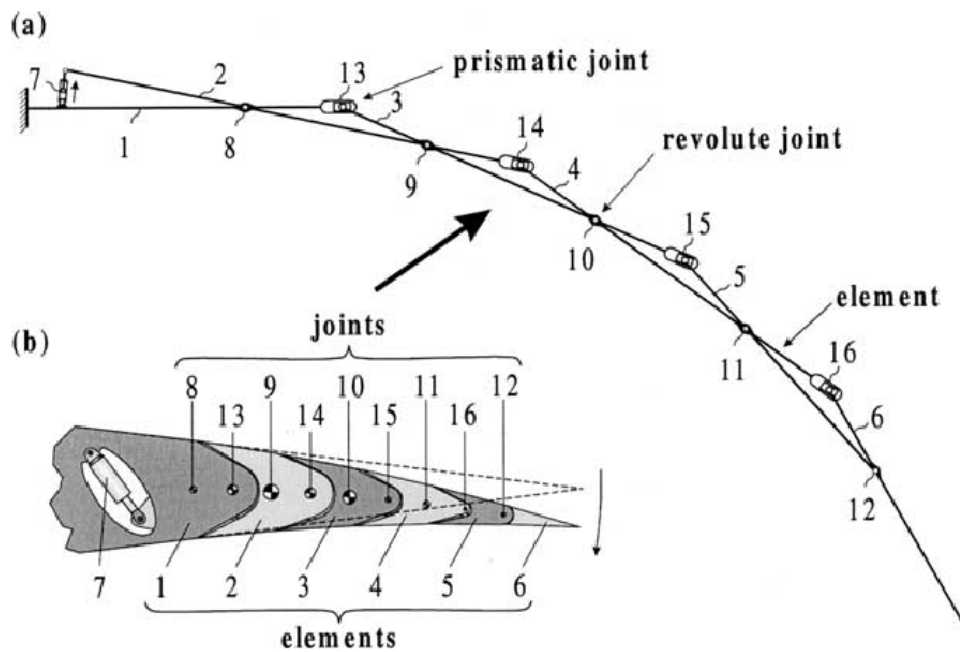


Figure 1.9 Kinematics of active deformable rib.

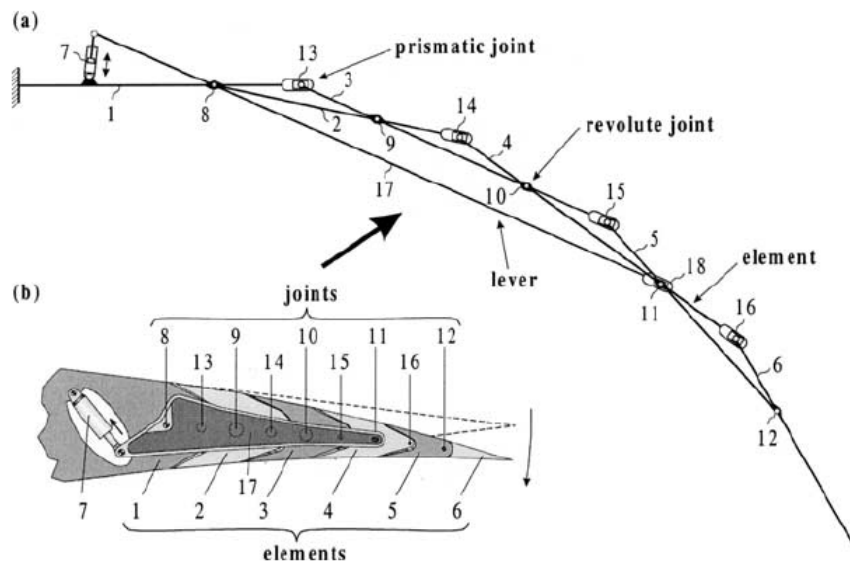


Figure 1.10 Kinematics of flexible rib with additional lever.

(3) is bent towards the second one (2) about revolute joint (9). These kinematics can be applied to an unlimited number of elements. To provide functionality at least three elements must be used. A variation of the individual length between the joints (e.g. the region between the joints (8) and (9), (8) and (13) as well as (9) and (13)) allows a precise adjustment of the rib contour. Figure 1.10 shows a modification of the active deformable rib with an additional lever (17) in order to reduce structural loads and the driving force. The kinematics of the active deformable rib remains the same with the exception that the actuator (7) is attached to lever (17) and not to element (2). The lever is connected to the first element (1) by revolute joint (8) and with element (4) by a prismatic joint (18). To provide functionality at least four elements must be used. The design of the upper and lower skin is presented in figure. As shown in section A-A the stringers are interrupted by a linear slide bearing. At the upper and lower part of the rib elements, counterparts are attached which make up the inside part of the linear slide bearing. These bearings allow a chord-wise displacement between the rib and the upper and lower skin. Simultaneously, a lift-off of the upper and lower skin due to aerodynamic loads is prevented. At the trailing edge the upper and lower skins are combined by a linear slide bearing allowing a chord-wise translation here, too. In addition the trailing edge can easily be replaced if damaged. As described, every rib element is connected to the upper and lower skin by linear slide bearings. These are individually dimensioned and positioned on the skin according to the loading that appears. For reasons of a better description of the kinematics the ribs are driven by a linear actuator. Since with this type of activation every rib has to be driven by an individual actuator, the number of them is quite high. Moreover, the total loading is introduced directly into the actuator requiring a powerful drive. By using a transmission beam together with a wedge system the amount as well as the loading of the actuator can be reduced. In figure 1.12 this drive system is presented with five ribs coupled to each other. The first rib element is provided with an opening where the transmission beam and the wedges are positioned. Since the beam is driven altogether by two actuators, less drives than ribs are needed. The actuators are mounted on the

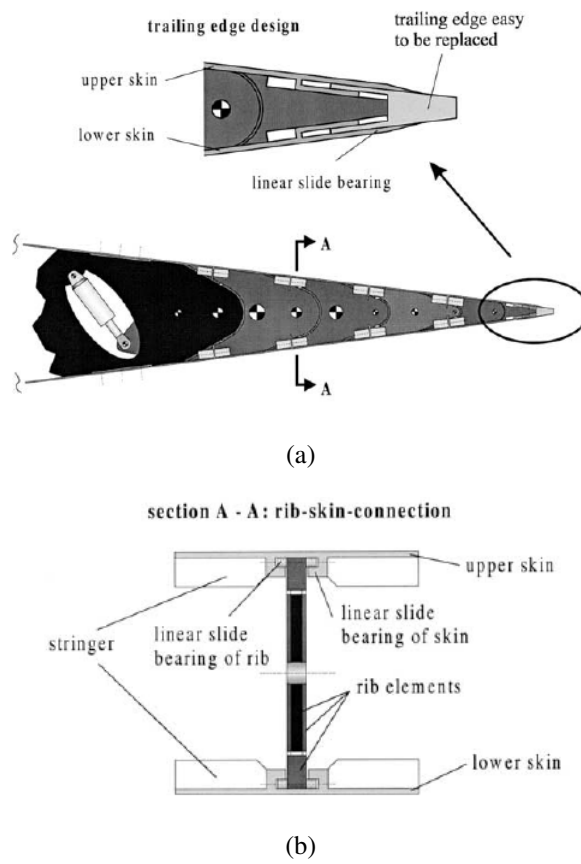


Figure 1.11 Design of upper and lower skin.

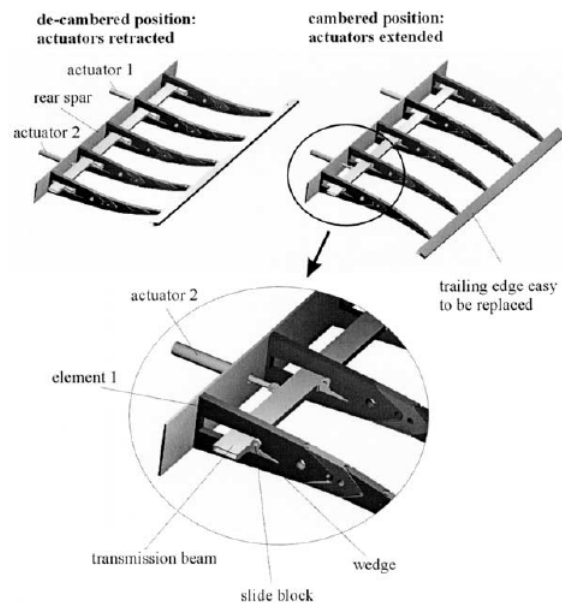


Figure 1.12 Drive system.

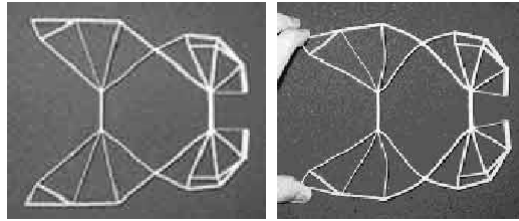


Figure 1.13 A structurally optimized compliant gripper illustrating distributed compliance

rear spar. When they are activated, the transmission beam to which the wedges are attached moves horizontally. This way cambered, an extension results in added camber. When actuated in the opposite direction a span-wise differential cambering is provided.

Camber change by using compliant kinematics

Kota (7) has been active in the field of compliant mechanism. Saggere and Kota (8), (9) designed a wing section with internal compliant system. A compliant mechanism is a class of mechanism that relies on elastic deformation of its constituent elements to transmit motion and/or force. These monolithic structures, an example is shown in Fig. 1.13, are in fact mechanisms without any joints, neither conventional hinges nor flexural hinges. Many practical benefits can be realized by exploiting compliance in engineering design. These include: reduced complexity, zero backlash and wear, sub-micron accuracy, and embedded actuation/sensing. Mechanisms that possess distributed compliance, as opposed to lumped compliance, are much more fatigue resistant and easier to manufacture. Distributed compliant mechanisms derive their flexibility due to the topology and shape of the material continuum rather than concentrated flexion at few regions such as flexural hinges. Several computational approaches have been developed to design compliant mechanisms for desired force-displacement characteristics and more recently for generalized shape change. In addition, these novel mechanisms can be readily integrated with both conventional and unconventional (smart materials) actuation schemes. Because of these advantages, properly designed compliant mechanisms are well suited for shape morphing applications such as variable geometry leading and trailing edge surfaces, engine inlets, and other aircraft components. Their unitized construction makes their manufacture relatively simple, eliminating most complex assembly operations, and in many cases, the absence of joints can offer additional weight savings. Furthermore, problems due to wear, backlash and lubrication are eliminated. Compliant mechanisms can be designed for desired stiffness with a variety of materials including titanium, aluminium, steel, and composites. The primary challenge for compliant shape morphing systems is to create an efficient structure that can distribute local actuation power to the surface of the airfoil to produce a specified shape change. This system must provide the appropriate shape control over the surface while meeting stiffness, power, weight, packaging, and survivability constraints. The work of Kota (8) highlights ongoing work to design novel compliant mechanisms that efficiently morph aircraft structures in order to exploit aerodynamic benefits. It study to different types of morphing systems: (a) variable geometry wing and (b) high-frequency vortex generators for active flow control. In this document has been reported only the system (a). The purpose of the variable geometry leading edge was to challenge compliant mechanism technology to create a camber morphing mechanism that can

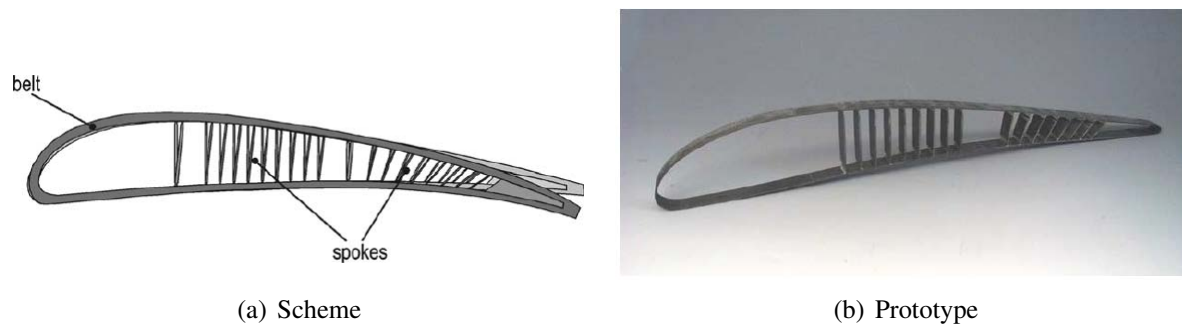


Figure 1.14 The belt rib configuration for the A340 landing flap.

maintain structural integrity under severe loads required by modern fighter aircraft. The design study essentially called for a retro-fit, or replacement, of an existing high performance fighter leading edge flap. This approach was valid to compare baseline power and weight with a baseline conventional flap design. It is desired to make the compliant mechanism flexible enough to undergo intended deformation by expending minimum actuator energy; however, it should be also be stiff enough to withstand the external air loads within structural and aeroelastic constraints. The optimized compliant structure embraces these conflicting design requirements. Effectively, the compliant mechanism is 400 times stiffer relative to external aerodynamic pressure loads (actuators locked) than it is for the actuators to cause intended deformation alone (no pressure load). The optimization algorithm effectively develops a structure that has maximum stiffness relative to external loads and minimum stiffness relative to intended deformation. This ensures that the actuator is primarily working against the reaction forces created by the aerodynamic loads while providing minimal effort deforming the structure. With the same technology a variable geometry trailing edge flap has been developed. The purpose of the variable geometry trailing edge flap was to create a seamless, hingeless flap that could effectively change wing camber and minimize drag over a wide lift range. In comparison, deflecting a conventional flap to try and accomplish this produces flow separation and increased drag. In the works of Kota ((8), (9)) it is possible to read over the benefits in weight and aerodynamic.

Campanile and Sachau (10) investigated another compliant structure called "belt-rib". The belt-rib frame was consisted of a closed shell (belt) reinforced by in-plane stiffeners (spokes). The belt rib concept evolved at DLR in the framework of the Adaptive Wing project (ADIF) with the purpose of reducing or eliminating the above mentioned disadvantages of conventional mechanisms by using flexible components instead of moveable parts. The basic idea of the belt-rib structural concept for airfoils is the replacement of the plate-fashioned rib in the conventional box-girder wing construction with an optimised compliant planar mechanism (see Fig. 1.14). The primary purpose is an active modification of the airfoil section; other modes of deformation, like twisting or bending, can be attained as a secondary effect by exploiting structural or aeroelastic coupling. The airfoil is provided with a closed skin of conventional kind which is bonded to the outer surface of the belt ribs. The belt-rib construction preferably does not include spars; the nose and trailing-edge skin panels are used as shear webs instead. Alternative designs with a single rear spar and/or a compliant fore spar are possible options. A belt-rib airfoil segment Fig. 1.15 (a) is exemplarily shown in the next figure, together with the

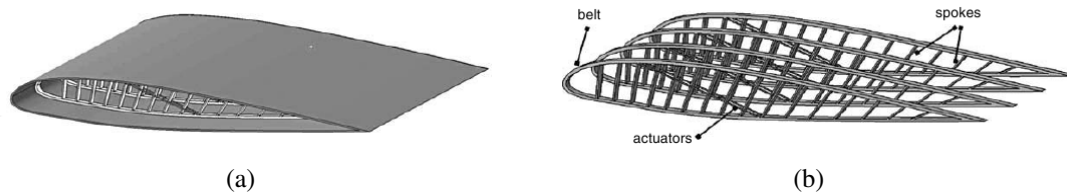


Figure 1.15 Belt-rib airfoil segment

corresponding set of belt ribs Fig. 1.15 (b). The belt-rib airfoil structure is conceived to retain most of the structural qualities of a conventional, fixed-shape wing construction while allowing a substantial degree of deformability. It is devised as a continuous, fully compliance-based, shape-adaptable system without sliding parts. In its basic layout, the belt-rib airfoil is a compliant system of mixed kind. The skin and the outer shell of the ribs (belt) are provided with distributed compliance; the spokes, which are responsible for stiffening the ribs in their plane, are designed as rigid elements; finally the connections between spokes and belt are realized as flexural hinges (lumped compliance). Alternative design options with entirely distributed compliance are conceivable as well. The spokes' configuration is optimised to be compliant to a previously chosen deformation mode, which somehow represents the kinematics of the belt rib as a mechanism. The deformation mode defines the target shape change of the airfoil section but for a single parameter, which can be controlled by a proper actuator. For deflections which are to conform to the deformation mode the belt rib shows virtually the same stiffness as the sole belt, whereas the stiffness related to other deformation components is comparable with that of a conventional plate rib. The belt rib's kinematics is freely configurable; the only limitation which applies to the choice of the deformation mode is the inextensibility condition: to avoid a membrane stress state during activation, only deflection patterns with constant arc length are allowed. The optimisation of the spokes' layout is performed on the basis of a modal procedure specially developed for this purpose. The restriction of the belt-rib's kinematics to virtually one mode (or to a small number of modes, if the above-mentioned layout optimisation is extended to more than one deformation mode) allows a broad choice of options for actuation. Linear actuators obliquely connecting one point on the upper side of the belt with one point on its lower side (see Figure) represent perhaps the simplest option. If externally activated tendons (e.g. Bowden cables) or shape-memory alloys are used, a truss configuration allows working only with tension actuator forces. Alternatively, active material can be embedded into the belt, which can in this way be directly activated in a bending mode. A peculiar characteristic of the belt-rib design philosophy is the absence of a general claim for maximum compliance; on the contrary, stiffness is intentionally kept over a prescribed bound, usually by acting on the belt design. By choosing a higher bending stiffness of the belt, the system's structural redundancy can be enhanced and the forces acting on the actuator in the presence of external loads decreased. Furthermore, a stiffer belt guarantees contour smoothness and reduces undesired deflections under load. The belt-rib interfaces to the rest of the airfoil construction essentially like a conventional rib. The airfoil skin is bonded to the rib and follows its deformation pattern while keeping a closed contour.

Camber change by using bi-stable laminate composite structure

Bistable or multi-stable structures are good candidates to be used as morphing structures because of their ability to remain in natural equilibrium after a shape change occurs. One can actuate such structures from one stable shape to another using device such as piezoceramic, shape memory alloy or conventional actuators. Although multi-stability can be achieved with the traditional isotropic materials, for morphing aerospace structures, fibre-reinforced laminated composites seem to be better suited because of their superior mechanical properties. Moreover, these laminated composites allow one to design their mechanical properties for a particular application by tailoring their laminate configuration. A non-symmetric laminated composite plate can take multiple cylindrical shapes when cooled from an elevated temperature to the room temperature. This structure can snap-through from one cylindrical shape to another by applying moments along the opposite edges of the laminate. The bi-stability phenomenon is a coupling between the residual stresses induced by cooling and the geometric non-linearities given by the large out-of-plane deflections that appear within the structure. Diaconu et al., (11) have considered the use of bi-stable plates to provide the necessary deformations to alter the camber. A square bi-stable composite plate was inserted into the airfoil section along the chord (see Fig 1.16 (a)). The leading edge side of the bi-stable composite plate was clamped to the airfoil at its spar connection. On the other side, the trailing edge of the plate is hinged to the airfoil surface in order to allow relative movement of the skin during actuation. The top skin is allowed to slide over the bottom skin during actuation. By actuating the bi-stable plate, the airfoil section is morphed between two different stable shapes (see Fig. 1.16 (b)). The transition between the two stable configurations in the presence of applied load was not discussed in their paper.

1.2.2 Complete airfoil adaptation

The most complex adaptation to changing flight conditions involves adjusting the entire wing geometry or changing the air foil section geometry in response to a change in lift coefficient, for instance, due to fuel-burn, or a scheduled or inadvertent change in cruise Mach number (Fig. 1.17). Varying the airfoil geometry can be accomplished by a set of discrete actuators capable of moving the surface while paying attention to keep the geometry changes or surface deflections small so as not to overstress the surface skin and avoid interfering with the landing/take-off high-lift devices. In addition, it is desired to utilize a minimum number of actuators to facilitate surface changes and to keep the weight of the active control devices, hence installation penalties, low. Several researchers have explored the ways to alter the aerodynamic properties of the wing by the reshaping of the airfoil profile (without significant change of its camber), Table 1.1. To do so the upper and/or lower camber of the airfoil is changed without major changes of the mean camber line. Variable length trusses were examined by Austin et al. (12) to reshape the airfoil. They attached linear displacement actuators inside the wing section in a diagonal manner (Fig. 1.18). The airfoil shape could therefore be modified by the expansion or contraction of the actuators. They constructed a model of an adaptive rib with 14 mechanical ball-screw actuators to demonstrate their shape-control concept. A theoretical model was developed, and validated, which could be implemented to determine the optimal airfoil shape for various flight conditions. Joo and Sanders (13) outlined an approach to change the airfoil shape by connecting internal mechanisms to a compliant skin material. Their method could be used

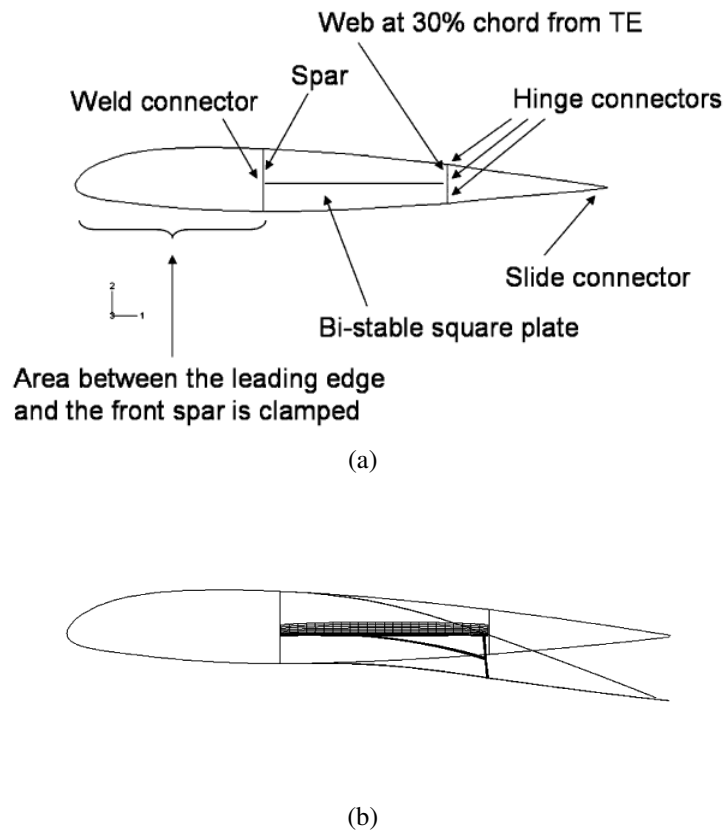


Figure 1.16 Stable shapes for camber change of airfoil section.

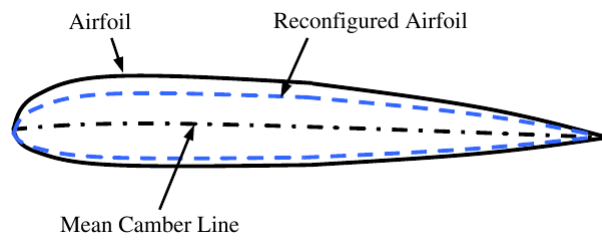


Figure 1.17 Airfoil adaptation.



Figure 1.18 Mechanisms

Table 1.1 Reshaping of airfoil profile studies.

Author	Morphed Geometry	Actuator	Skin	Prototype	Wind Tunnel Test	Flight test
Austin et al. (12)	Airfoil	Conventional	Flexible	y	n	n
Joo and Sanders (13)	Airfoil	Conventional	Flexible	y	n	n
Strelec et al. (14)	Airfoil	SMA	Flexible	y	n	n
Dong et al. (15)	Airfoil	SMA	Flexible	y	n	n
Georges et al. (16)	Airfoil	SMA	Flexible	n	n	n
Pinkerton et al. (17)	Airfoil	PZT	Flexible	y	y	n

to find appropriate compliant structures capable of achieving target profile shapes. To do so, they synthesized a mechanism that could be reconfigured to meet a set of target profile shapes while keeping the actuator loads under a certain limit. The patent database and aircraft design archives contain many similar airfoil adjustment concepts which require conventional actuators. Such mechanical systems in general result in significant weight penalty and are therefore not considered in this paper any further. The suitability of SMA (Shaper Memory Alloy) actuation for morphing of aircraft wing has been first demonstrated by the designs that changed the airfoil profile. A prominent sample is the design by Strelec et al. (14). They attached SMA wire actuators to points at the inside of an airfoil. By the actuation of the SMA wires, the airfoil could be reshaped. They developed an optimization method to determine the proper placement of the SMA wire actuators within the wing. The results from the structural, thermal, and aerodynamic analysis could be put into their global optimization method to find the best configuration for the SMA wires placement. A prototype of a reconfigurable wing was fabricated by them to assess the predicted structural and aerodynamic responses for optimality. Wind tunnel tests indicated that an increase in the lift is feasible for a given flow velocity and angle of attack by activating the SMA wire actuators. In an alternate approach Dong et al. (15) placed SMA springs between the wing skin and its supporting wing-box. The wing-box in their design consisted of rigid steel ribs and spars. The covering skin was allowed to slide over a cushion at the leading edge spar. The resizing of the SMA spring length upon heating and cooling could alter the wing thickness. In another concept developed by Georges et al. (16), SMA linear actuators were connected to a flexible skin through a cam based transmission system. Contraction of the SMA wire upon heating could rotate the cam and transfer the displacement of the SMA wire to a flexible skin by means of a crank. The flexible structure of the morphing wing could create the biasing force which is necessary for the reversible actuation of the compliant SMA system. Although they did not fabricate a prototype of an actuated wing, they examined the performance properties of SMA actuators. Pinkerton et al. (17) used an out-of-plane piezoelectric actuator (PZT), called thin layer composite-unimorph ferroelectric driver and sensor (THUNDER) (18), to reshape the airfoil. One end of the actuator at the trailing edge side was fixed to the airfoil to permit relatively free expansion and contraction under an applied voltage. Out of plane deformations of up to 2.5 mm was achieved for a sub-scale 125 mm long airfoil at 400 V. After testing for two weeks in the wind tunnel, the overall displacement performance of the THUNDER wafer began to degrade, noticeably.

1.2.3 Actuation systems

In this paragraph will be analysed only the new generation actuation systems, piezoelectric materials and shape memory alloy, that allowed a reduction of weight respect the classical actuation systems. The reduction of the actuation system weight is very important in the field of smart wing. In fact the need for a distributed actuation system requires a larger number of actuators respect the conventional control surface. In the following paragraphs will be analysed different works which dealing about piezoelectric and SMA actuation systems.

Piezoelectric actuation

Wang et al. (19) report that PZT actuation was considered for the *Smart Wing 2 program* by DARPA for high-rate actuation of hingeless control surfaces. The concept relied on the bending moment distribution by means of piezoelectric stacks. The stacks were mounted locally between two reacting "vertebrae" which provided the necessary arm to convert the linear extension of the stack into local moments. While this concept initially seemed promising, it was quickly found to be inappropriate because the targeted deflection was unachievable with the small induced strain of the best known PZT stacks. Although using mechanical amplifiers with multiple levers were exploited to address the limited stroke of the PZT actuators, such concepts were later discarded because of the space limitation and the high flexural stresses at the mechanical amplification linkage. They also considered using fluidic amplifiers, but eventually the PZT-based designs were not pursued in the *Smart Wing program*. In another effort, Vos et al. (20) investigated the use of PZT to deform the center plate of a prototype wing. Their approach was different from the Smart Wing program in that they used stretchable skin to enhance the deformations. The PZT actuators in their design were used to deform a post-buckled plate (PBP). The PBP actuator consisted of two conventional piezoelectric sheets bonded to either side of a structurally stiff center plate. Asymmetrical electrical potential was applied to the two piezoelectric sheets to expand one and contract the other to cause the center plate to bend. They achieved trailing-edge deflections of ± 3.1 . Wind tunnel and flight tests showed that the post-buckled pre-compressed morphing wing increased the roll control authority of a UAV (with 1.4 m span), and also reduced power consumption. Lim et al. (21) used lightweight PZT composite actuators called LIPCA to deform the trailing edge of an airfoil section. The LIPCA actuators in their design were embedded between three glass/epoxy and graphite/epoxy layers in a non-symmetric stacking sequence. Two models were made. In the first, only the top layer was active, while for the second design both top and bottom layers were active. They achieved 5 of trailing edge deformation at 300 V input at load-free condition. The effect of out-of-plane aerodynamic forces on the trailing edge should have been investigated for any shape morphing application. Heinze and Karpel (22) also explored the application of a Lead Zirconate Titanate biomorph PZT plate to rotate a tab for aeroelastic positioning of a trailing edge flap. The tab occupied the rear 25% of a free-floating trailing edge flap. The actuator mechanism was fixed to a frame inside the flap. Voltage excitation of the bi-morph actuator resulted in the vertical displacement of the actuator tip, located halfway between the flap hinge and the tab axis, leading to the rotation of the tab. Flap deflection of 4.6 was obtained by a -2.5 tab rotation. The research demonstrated the feasibility of piezoelectric materials for aeroelastic shape control of control surfaces.

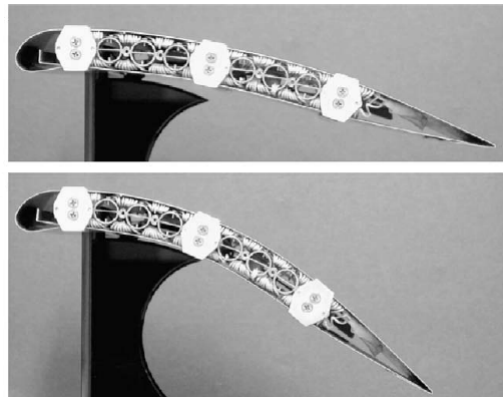


Figure 1.19 Shape morphing aero control surface in two configurations.

Shape memory alloy actuation

Shape memory alloy was also a candidate actuating material for the *DARPA Smart Wing program* (Wang et al. (19)). Two SMA linear actuators were connected to tip of a flexible trailing edge in their concept. The other ends were connected to the top and bottom of the trailing edge spar in an antagonistic way. The contraction of the actuators could bend the trailing edge respectively. Wang reports that the gained deformations were not satisfactory because the ability of the actuator to displace the trailing edge tip was reduced as a result of wasting of the shape memory recovery force due to the undesired in-plane compression of the center sheet. To address the above issue, Sofla et al. (23) (24) developed a series of SMA-actuated flexural structures which could be used to deform wing sections. Their actuated structures were based on a concept called antagonistic flexural unit cell (AFC) in which a pair of one-way SMA actuators were placed at either side of a highly flexible unit core structure (with large in-plane stiffness). The contraction of one SMA actuator upon heating, results in the extension of the opposing SMA actuator mechanically. The contraction by heating of the now-extended actuator, later in the cycle, reverses the actuation. High authority shape morphing beams can be made by the linear replication of the AFCs. Such actuated beams (Elzey et. al. (25) , (26)) can be used in the making of reconfigurable wing boxes for shape morphing wing structures. Fig. 1.19 shows a wing section prototype capable of undergoing camber changes (Elzey et. al. (26)). Although the slow cooling rate of the SMA actuation is not appropriate for the flight control applications, the achievable aerodynamic changes are still suitable for in-flight mission adaptation of the wing. The AFC based actuated structures are attractive for wing morphing applications because: (1) the distributed SMA actuators carry aerodynamic load and therefore reduce the weight penalty, and (2) the new wing shapes after the cooling of each SMA actuator are retained without requiring power, which can eventually result in saving fuel and increasing the aircraft endurance. Berton (27) also used SMA wire in an antagonistic manner to rotate a flap, but the wires were connected in a linear set up (different from the AFC concept). One end of the two wires in their prototype was connected together with a simple joint and the other ends were fixed inside the wing-box. Contraction of one wire due to the heating displaced the joint between the two wires. This displacement was then transmitted to the trailing edge by means of a linkage. The flap could rotate 45 for the overall length of SMA wires of 1200 mm. A major disadvantage of the

system is the relative complexity of the transmission mechanism which consisted of several linkages. In a compliant approach for SMA actuation, Yang et al. (28) attached the SMA wires to the bottom skin of a wing. Contraction by heating of the SMA actuators could deform the wing. The wing could restore its initial shape upon cooling of the SMA. The main disadvantage of the compliant SMA actuation is that the new shape is retained until the temperature of the SMA wire is maintained above its Martensite start transformation temperature. The compliant SMA actuation method is not therefore suitable for long term applications. Liu et al. (29) also used a SMA wire to deform a compliant wing section, in which the top skin was fixed to the spar while the bottom skin could slide into the spar to accommodate the rotation of the trailing edge. In their design one end of the SMA wire was fixed in the wing-box, and the other end was attached to a point next to the trailing edge. The trailing edge could therefore be rotated by the contraction of the SMA wire. The reliance of their concept on the compliance of the top skin to return the trailing edge to the original shape is questionable.

1.3 Present work objectives and outline

The field of shape morphing aircraft has attracted the attention of hundreds of research groups during the past century. Although many interesting concepts have been synthesized, only a handful of such reconfigurable planes have been ever produced (all of them supersonic and consisted of pivoting wings). Although several conceptual designs of small or low speed aircraft has made it to the wind tunnel testing stage, only very limited number of such shape morphing prototypes have ever been fabricated or flight tested. The explosive growth of satellite services during the past few years has made the UAVs the technology of choice for many routine applications such as border patrol, environmental monitoring, meteorology, military operations and search and rescue. In addition, the recent advances in smart materials research including the developments in the actuation technology, constitutive law and modelling, optimization and control, and failure prediction, demands more purposeful steps in the progress of variable geometry small aircraft. In general, any successful wing morphing scenario must overcome the weight penalty due to the added actuation systems. Compared to supersonic aircraft, the small or low speed planes require more dramatic wing variations for a noticeable and practical change in their aerodynamic properties. This points us to the crux of the development of low speed/small shape morphing planes which is the large weight penalty over gross weight ratio. To address the above challenge, any successful conceptual design for shape morphing of low speed/small aircraft should:

- Undergo large geometry changes.
- Use smart materials for actuation.
- Use the smart material actuators for supporting part of the aerodynamic loads.
- Have integrated and distributed actuators to avoid transmission mechanisms.
- Use advanced light-weight composites for the fixed structure and the skin.

This work is aimed to the development of a multifield formulation based on higher-order structural models. CUF 1D models are exploited for the structural modeling.

Chapter 2

Reduced Finite models

2.1 Introduction

Laminated shell/plate structures such as traditional composite and sandwich panels are found frequently in aerospace vehicles applications. High transverse shear and normal deformability as well as discontinuity of physical properties make the use of structural models difficult. Accurate stress and strain fields evaluation demand the development of ad hoc theories for the analysis of these non traditional structures. So-called C_z^0 requirements (Carrera (30)) could be considered for the development of appropriate theories for layered structures. Many excellent review papers are available on multilayered structure modelling, which refer to the following relevant articles and books, Lekhnitskii (31), Ambartsumian (32–35), Grigolyuk and Kogan (36), Leissa (37), Librescu and Reddy (38), Grigoliuk and Kulikov(39), Kapania and Raciti(40), Kapania (41), Vasiliev and Lure(42), Noor and Burton (43; 44), Noor et al. (45), Jemlelita (46), Reddy and Robbins(47), Lure and Shumova(48), Grigorenko (49), Grigorenko and Vasilenko(50), Altenbach (51), Carrera (30; 52), Reddy (53), Qatu (54). The above articles and monographs cover the state of the art of layered theories and computational methods for plates and shells, including mixed theories and Zig-Zag models. In most of the applications the constituent layer show in-plane orthotropic behavior whose orientation in each layer is a result of an optimization process (the so-called tailoring design of laminated composites). Furthermore, the layered construction introduces, by definition, transverse anisotropy. As a result the transverse anisotropy is always accomplished by in-plane anisotropic behaviour. In-plane and out-of-plane anisotropy introduce further complications due to the solution of governing equations related to given structural problems involving laminates (bending, vibration, buckling, dynamic response etc). Closed form solutions are available only in very few cases and the use of computational methods such as Finite Element Methods (FEM) becomes mandatory in practical problems. A large amount of two-dimensional models and finite element implementation can be obtained by combining the available laminated theories (see the reviews in Kapania and Raciti(40), Kapania (41), Noor and Burton (43; 44), Noor and Burton and Bert (45) and Carrera (55)). In the case of layered structures the so-called Zig-Zag (ZZ) theories are particularly noteworthy since they include the ZZ effect through-the-thickness variation and the Interlaminar Continuity (IC) of transverse shear and normal stresses within the equivalent single layer approach. A historical overview(52) has established that the ZZ theories can be

grouped as: Lekhnitskii's Multilayered Theories (LMTs); Ambartsumian's Multilayered Theories (AMTs) and Reissner's Multilayered Theories (RMTs).

Refined plate theories offer significant advantages in terms of accuracy of the solution and detection of non-classical effects. The drawback of these theories is that a higher computational cost is incurred because of the presence of a large number of displacement variables. Such an increase could become prohibitive in the case of the application of computational methods such as the Finite Element Method. To control the behaviour of an actuated wing are necessary model with a low computational time. In fact the computational time must be lower than the characteristic time of the controlled phenomenon.

The smart wing field required to giving an answer to the following question: for a given problem (geometry, loading, boundary conditions, lamination lay-out) what is the most accurate theory in terms of a fixed accuracy with the lowest computational time?

An effective comparison of resulting theories could be done if and only if it would a possibility to 'run' the various theories for an assigned problem (materials, geometry, lamination lay-out, boundary conditions) at the same time. For this purpose the Carrera has proposed in the last decade the Carrera Unified Formulation (CUF) (56),(57),(58), with some finite element applications provided in (59), (60) and (55). CUF permits the formulation/comparison of Equivalent Single Layer or Layer-Wise, linear, parabolic and higher expansion orders. Classical theories such as CLT and FSDT can be retrieved as particular cases. In their work, Carrera and Petrolo (61) analysed the effect of various parameters like geometry, lamination, material, boundary and loading conditions on the accuracy of a given theory. The focus was on closed form solutions and effects and orthotropic simply supported plates loaded by harmonic distribution of transverse loading. In their work the contribution of each term to the accuracy of the solution has been evaluated, introducing the so-called mixed axiomatic/asymptotic method, which is able to recognize the effectiveness of each displacement variable of an arbitrary refined plate theory. It can be stated that the choice of the plate model which suits the accuracy requirements for a given problem is dominated by :

1. the length-to-thickness ratio
2. the orthotropic ratio
3. the lamination sequence.

It has also been found that each displacement/stress component would require its own plate model (which differs according to the change in outputs) to obtain exact results. Moreover, the accuracy of the solution also depends on the thickness coordinate z . From the work of Carrera and Petrolo (61) following points need to be mentioned:

- The number of retained variables is very closely related to the geometrical/mechanical configuration of the considered problem.
- Remarkable benefits, in terms of total amount of problem variables, are obtained for thin plates or for symmetrical laminations.
- The use of full models is mandatory when a complete set of results is needed.

CUF has shown to be well able to deal with a method that could be stated as a mixed asymptomatic/asymptotic structural analysis of different plate structures. Its usage has made it possible to consider the plate theory as well as the structural configuration as free parameters of the analysis. Two main benefits can be obtained using CUF:

- It permits the accuracy of each problem variable to be evaluated by comparing the results with more detailed analyses (also provided by CUF); no mathematical/variational techniques are needed as in the case of asymptotic-type analyses.
- It offers the possibility of considering the accuracy of the results as an input, whereas the output is represented by the set of displacement variables which are able to fulfill the requirement.

Starting from the work of Carrera and Petrolo (61) a more general method able to evaluate the effectiveness of each terms is developed. In order to evaluate to study more configuration than Carrera and Petrolo (61) the Finite Element Method is used. As in the Carrera and Petrolo (61) work only plate theories with generalized displacement variables are considered. These theories can be divided on the basis of the variables description:

1. Layer-Wise Models (LWMs) in which the number of unknown variable depend upon the number of layers.
2. Equivalent Single Layer Models (ESLMs) in which a laminate plate is reduced to a single lamina of "equivalent" characteristics.

These theories can further be classified according to the expansion adopted for the unknown displacement variables in the plate/layer thickness directions:

1. classical models with linear expansion such as Classical lamination theories CLT and First order shear deformation theories FSDT, based on Kirchhoff (62) and Reissner-Mindlin (63), (64) assumptions, respectively.
2. Refined models with higher order expansions of the displacement components on the reference surface.

Examples of these theories can be found in the previously mentioned review works.

2.2 Geometry and material arrays

The coordinate reference frame is shown in Fig. 4.9, where x and y are the in-plane coordinates while z is the thickness coordinate. The displacement vector, \mathbf{u}^k , of a single layer is defined as:

$$\mathbf{u}^k(x, y, z) = \left\{ u_x^k \quad u_y^k \quad u_z^k \right\}^T \quad (2.1)$$

The superscript "T" represents the transpose operator. Stress and strain components are grouped as follows:

$$\begin{aligned} \boldsymbol{\sigma}_p^k &= \left\{ \sigma_{xx}^k \quad \sigma_{yy}^k \quad \sigma_{xz}^k \right\}^T & \boldsymbol{\epsilon}_p^k &= \left\{ \epsilon_{xx}^k \quad \epsilon_{yy}^k \quad \epsilon_{xz}^k \right\}^T \\ \boldsymbol{\sigma}_n^k &= \left\{ \sigma_{xz}^k \quad \sigma_{yz}^k \quad \sigma_{zz}^k \right\}^T & \boldsymbol{\epsilon}_n^k &= \left\{ \epsilon_{xz}^k \quad \epsilon_{yz}^k \quad \epsilon_{zz}^k \right\}^T \end{aligned} \quad (2.2)$$

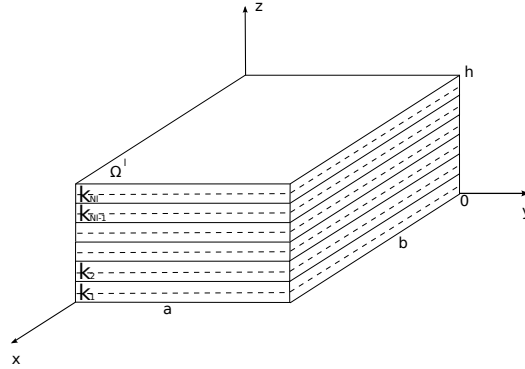


Figure 2.1 Plate geometry

where p indicates the in-plane components and n the out-of-plane components. Linear strain-displacement relations are defined as:

$$\begin{aligned}\epsilon_p^k &= \mathbf{D}_p \mathbf{u}^k \\ \epsilon_n^k &= \mathbf{D}_n \mathbf{u}^k = (\mathbf{D}_{n\Omega} + \mathbf{D}_{nz}) \mathbf{u}^k\end{aligned}\quad (2.3)$$

where:

$$\mathbf{D}_p = \begin{bmatrix} \frac{\partial}{\partial x} & 0 & 0 \\ 0 & \frac{\partial}{\partial y} & 0 \\ \frac{\partial}{\partial y} & \frac{\partial}{\partial x} & 0 \end{bmatrix} \quad \mathbf{D}_{n\Omega} = \begin{bmatrix} 0 & 0 & \frac{\partial}{\partial x} \\ 0 & 0 & \frac{\partial}{\partial y} \\ 0 & 0 & 0 \end{bmatrix} \quad \mathbf{D}_{nz} = \begin{bmatrix} \frac{\partial}{\partial z} & 0 & 0 \\ 0 & \frac{\partial}{\partial z} & 0 \\ 0 & 0 & \frac{\partial}{\partial z} \end{bmatrix}\quad (2.4)$$

The stress components in the material reference coordinates are obtained by the constitutive law:

$$\sigma_m^k = \mathbf{C} \epsilon_m^k \quad (2.5)$$

where \mathbf{C} , σ_m and ϵ_m are written in the material coordinates (see Fig. 2.2) and \mathbf{C} is defined as

$$\mathbf{C} = \begin{bmatrix} C_{11} & C_{12} & 0 & 0 & 0 & C_{13} \\ C_{12} & C_{22} & 0 & 0 & 0 & C_{23} \\ 0 & 0 & C_{66} & 0 & 0 & 0 \\ 0 & 0 & 0 & C_{55} & 0 & \\ 0 & 0 & 0 & C_{44} & 0 & \\ C_{13} & C_{23} & 0 & 0 & 0 & C_{33} \end{bmatrix}\quad (2.6)$$

with

$$\begin{aligned}C_{11} &= E_1 \frac{1 - \nu_{23}\nu_{32}}{\Delta} & C_{12} &= E_1 \frac{\nu_{21} + \nu_{31}\nu_{23}}{\Delta} = E_2 \frac{\nu_{12} + \nu_{32}\nu_{13}}{\Delta} \\ C_{22} &= E_2 \frac{1 - \nu_{13}\nu_{31}}{\Delta} & C_{13} &= E_1 \frac{\nu_{31} + \nu_{21}\nu_{32}}{\Delta} = E_3 \frac{\nu_{13} + \nu_{12}\nu_{23}}{\Delta} \\ C_{33} &= E_3 \frac{1 - \nu_{12}\nu_{21}}{\Delta} & C_{23} &= E_2 \frac{\nu_{32} + \nu_{12}\nu_{31}}{\Delta} = E_3 \frac{\nu_{23} + \nu_{21}\nu_{13}}{\Delta} \\ C_{44} &= G_{23} & C_{55} &= G_{13} & C_{66} &= G_{12} \\ \Delta &= 1 - \nu_{12}\nu_{21} - \nu_{23}\nu_{32} - \nu_{31}\nu_{13} - 2\nu_{12}\nu_{32}\nu_{13}\end{aligned}\quad (2.7)$$

For every layer a rotation matrix is obtained as

$$T^k = \begin{bmatrix} \cos^2 \theta & \sin^2 \theta & -\sin 2\theta & 0 & 0 & 0 \\ \sin^2 \theta & \cos^2 \theta & \sin 2\theta & 0 & 0 & 0 \\ \sin \theta \cos \theta & -\sin \theta \cos \theta & \cos^2 \theta - \sin^2 \theta & 0 & 0 & 0 \\ 0 & 0 & 0 & \cos \theta & -\sin \theta & 0 \\ 0 & 0 & 0 & \sin \theta & \cos \theta & 0 \\ 0 & 0 & 0 & 0 & 0 & 1 \end{bmatrix} \quad (2.8)$$

where θ is the angle between the 1-coordinate and the x-coordinate. It is possible to write the

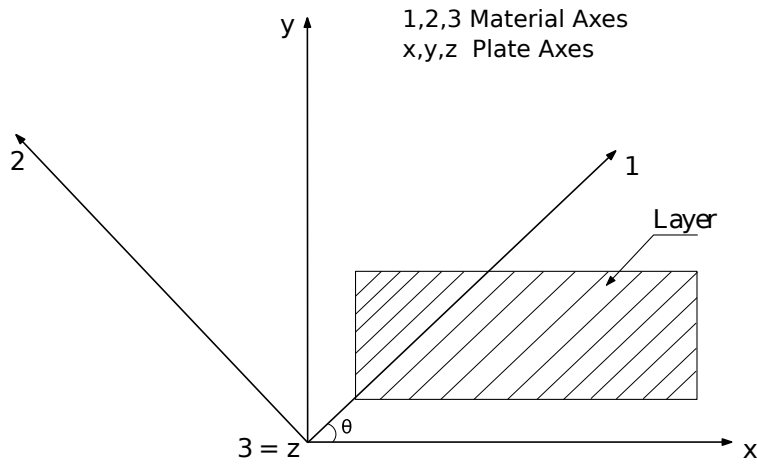


Figure 2.2 Material coordinates and plate coordinates.

stresses and the strains in the plate coordinates

$$\boldsymbol{\sigma} = \mathbf{T} \boldsymbol{\sigma}_m \quad \boldsymbol{\epsilon} = \mathbf{T}^T \boldsymbol{\epsilon}_m \quad (2.9)$$

Using equation 2.9, equation 2.5 becomes

$$\boldsymbol{\sigma} = \mathbf{TCT}^T \boldsymbol{\epsilon} \quad (2.10)$$

Denoting $\tilde{\mathbf{C}}$ as

$$\tilde{\mathbf{C}} = \mathbf{TCT}^T \quad (2.11)$$

it is possible to rewrite the constitutive law in plate coordinates as

$$\boldsymbol{\sigma} = \tilde{\mathbf{C}} \boldsymbol{\epsilon} \quad (2.12)$$

or (according to Eq. 3.19),

$$\begin{aligned} \sigma_p^k &= \tilde{\mathbf{C}}_{pp}^k \epsilon_p^k + \tilde{\mathbf{C}}_{pn}^k \epsilon_n^k \\ \sigma_n^k &= \tilde{\mathbf{C}}_{np}^k \epsilon_p^k + \tilde{\mathbf{C}}_{nn}^k \epsilon_n^k \end{aligned} \quad (2.13)$$

The material matrices can be grouped as

$$\tilde{\mathbf{C}}_{pp}^k = \begin{bmatrix} \tilde{C}_{11} & \tilde{C}_{12} & \tilde{C}_{16} \\ \tilde{C}_{21} & \tilde{C}_{22} & \tilde{C}_{26} \\ \tilde{C}_{61} & \tilde{C}_{62} & \tilde{C}_{66} \end{bmatrix}^k \quad \tilde{\mathbf{C}}_{nm}^k = \begin{bmatrix} \tilde{C}_{55} & \tilde{C}_{54} & 0 \\ \tilde{C}_{45} & \tilde{C}_{44} & 0 \\ 0 & 0 & \tilde{C}_{33} \end{bmatrix}^k \quad \tilde{\mathbf{C}}_{pn}^k = \tilde{\mathbf{C}}_{np}^{kT} = \begin{bmatrix} 0 & 0 & \tilde{C}_{13} \\ 0 & 0 & \tilde{C}_{23} \\ 0 & 0 & \tilde{C}_{36} \end{bmatrix}^k \quad (2.14)$$

For the sake of brevity, the expression of the coefficient \tilde{C}_{ij}^k are not reported here, but can be found in the books by Tsai (65)

2.3 Carrera Unified Formulation - 2D Formulation

In the framework of the Carrera Unified Formulation, the displacement components u_x^k , u_y^k and u_z^k of the k -layers (the total number of layers is indicated by N_l) are postulated, in the z -direction, according to the expansion

$$\begin{aligned} u_x^k &= F_t u_{xt}^k + F_r u_{xr}^k + F_b u_{xb}^k \\ u_y^k &= F_t u_{yt}^k + F_r u_{yr}^k + F_b u_{yb}^k \\ u_z^k &= F_t u_{zt}^k + F_r u_{zr}^k + F_b u_{zb}^k \end{aligned} \quad r = 2, 3, \dots, N \quad (2.15)$$

The subscript t and b denote values related to the top and bottom layer surfaces, respectively. F_t, F_r , and F_b are base functions of z . Through the model (2.15) the continuity of the displacement can be imposed to the layer interfaces. Equation (2.15) can be written in a compact manner as

$$\mathbf{u}^k = F_t \mathbf{u}_t^k + F_r \mathbf{u}_r^k + F_b \mathbf{u}_b^k = F_\tau \mathbf{u}_\tau^k \quad \tau = t, r, b; \quad r = 2, 3, N \quad (2.16)$$

where the components of \mathbf{u}_τ^k are

$$\mathbf{u}_t^k = \begin{Bmatrix} u_{xt}^k \\ u_{yt}^k \\ u_{zt}^k \end{Bmatrix} \quad \mathbf{u}_r^k = \begin{Bmatrix} u_{xr}^k \\ u_{yr}^k \\ u_{zr}^k \end{Bmatrix} \quad \mathbf{u}_b^k = \begin{Bmatrix} u_{xb}^k \\ u_{yb}^k \\ u_{zb}^k \end{Bmatrix} \quad (2.17)$$

From (2.15) any-order displacement fields, Layer Wise (LW) and Equivalent Single Layer (ESL), can be adopted. Imposing the conditions

$$\begin{aligned} u_{xt}^k &= u_{x1} & u_{xr}^k &= u_{xr} & u_{xb}^k &= u_{x_{N+1}} & F_t &= 1 \\ u_{yt}^k &= u_{y1} & u_{yr}^k &= u_{yr} & u_{yb}^k &= u_{y_{N+1}} & F_r &= z^{r-1} \\ u_{zt}^k &= u_{z1} & u_{zr}^k &= u_{zr} & u_{zb}^k &= u_{z_{N+1}} & F_b &= z^N \end{aligned} \quad (2.18)$$

and discarding k it is possible to obtain an ESL displacement field. For example if $N = 4$ it is possible to obtain the following displacement field

$$\begin{aligned} u_x &= u_{x1} + z u_{x2} + z^2 u_{x3} + z^3 u_{x4} + z^4 u_{x5} \\ u_y &= u_{y1} + z u_{y2} + z^2 u_{y3} + z^3 u_{y4} + z^4 u_{y5} \\ u_z &= u_{z1} + z u_{z2} + z^2 u_{z3} + z^3 u_{z4} + z^4 u_{z5} \end{aligned} \quad (2.19)$$

Classical plate theories can also be obtained. The Reissner-Mindlin plate model approximation (see Reissner and Mindlin (63; 64)), also known as First Order Shear Deformation Theory, FSDT, in the case of laminates, requires two conditions: 1) First-order approximation kinematic fields, 2) the displacement component u_z has to be constant above the cross-section, i.e. $u_{z2} = 0$. The resultant displacement model is:

$$\begin{aligned} u_x &= u_{x1} + z u_{x2} \\ u_y &= u_{y1} + z u_{y2} \\ u_z &= u_{z1} \end{aligned} \quad (2.20)$$

The Kirchhoff-type approximation (see Kirchhoff (62)), also known as Classical Laminate Theory or CLT, can also be obtained using a penalty technique for the shear correction factor. First-order models require the use of reduced material stiffness coefficients to correct the thickness locking (see Carrera and Brischetto (66; 67)). Higher-order theories from open literature can also be obtained via CUF. Some of these models are considered in this paper for comparison purposes. They are obtained via CUF. According to Pandya (see Pandya (68)), the displacement components are given by:

$$\begin{aligned} u_x &= u_{x1} + z u_{x2} + z^2 u_{x3} + z^3 u_{x4} \\ u_y &= u_{y1} + z u_{y2} + z^2 u_{y3} + z^3 u_{y4} \\ u_z &= u_{z1} \end{aligned} \quad (2.21)$$

Kant (see Kant (69)) also expanded the displacement component $u_z(x, y, z)$ in Taylor's series of the thickness coordinate (hereinafter referred to as Kant-1):

$$\begin{aligned} u_x &= u_{x1} + z u_{x2} + z^2 u_{x3} + z^3 u_{x4} \\ u_y &= u_{y1} + z u_{y2} + z^2 u_{y3} + z^3 u_{y4} \\ u_z &= u_{z1} + z u_{z2} + z^2 u_{z3} + z^3 u_{z4} \end{aligned} \quad (2.22)$$

A further theory by Kant (see Kant (70)) is considered in this work (hereinafter referred to as Kant-2):

$$\begin{aligned} u_x &= z u_{x2} + z^3 u_{x4} \\ u_y &= z u_{y2} + z^3 u_{y4} \\ u_z &= u_{z1} + z^2 u_{z3} \end{aligned} \quad (2.23)$$

It is important to underline that CUF allows us to choose the higher-order terms to be included with no restrictions. For instance, one can consider a plate theory where incomplete fourth-order expansions are adopted:

$$\begin{aligned} u_x &= +z u_{x2} + +z^3 u_{x4} + z^4 u_{x5} \\ u_y &= +z u_{y2} + z^2 u_{y3} + +z^4 u_{y5} \\ u_z &= u_{z1} + z u_{z2} + z^2 u_{z3} + +z^4 u_{z5} \end{aligned} \quad (2.24)$$

2.4 FE Governing Equations

The shape functions, N_i , and the nodal displacement vector, $\mathbf{q}_{\tau i}^k$, are introduced to rewrite the displacement vector \mathbf{u}^k :

$$\mathbf{q}_{\tau i}^k = \{q_{u_{x\tau i}}^k \ q_{u_{y\tau i}}^k \ q_{u_{z\tau i}}^k\}^T \quad (2.25)$$

$$\mathbf{u}^k = N_i F_{\tau} \mathbf{q}_{\tau i}^k \quad (2.26)$$

For the sake of brevity, the shape functions are not reported here. The four node plate element with an assumed shear strain field concept of MITC4 type (see Bathe and Dvorkin (71)) is adopted in this paper. The extension of the MITC4 element to the Unified Formulation has already been discussed in Carrera et al.(72).

Upon substitution of Eq. (2.26) in Eq. (2.3) it is possible to obtain:

$$\begin{aligned} \epsilon_p^k &= F_{\tau} \mathbf{D}_p (N_i \mathbf{I}) \mathbf{q}_{\tau i}^k \\ \epsilon_n^k &= F_{\tau} \mathbf{D}_{n\Omega} (N_i \mathbf{I}) \mathbf{q}_{\tau i}^k + F_{\tau,z} N_i \mathbf{q}_{\tau i}^k \end{aligned} \quad (2.27)$$

where \mathbf{I} stands for the identity matrix. The element stiffness matrix and the vector of external loadings, which are consistent with the model, are obtained via the Principle of Virtual Displacements:

$$\delta L_{int}^k = \int_V (\delta \epsilon_p^{kT} \sigma_p^k + \delta \epsilon_n^{kT} \sigma_n^k) dV = \delta L_{ext}^k \quad (2.28)$$

where L_{int}^k stands for the strain energy, and L_{ext}^k is the work of the external loadings. δ stands for the virtual variation. The virtual variation of the strain energy is rewritten in compact form using Eqs. (2.3), (2.13) and (2.26) as

$$\delta L_{int}^k = \delta \mathbf{q}_{\tau i}^{kT} \mathbf{K}^{k\tau s i j} \mathbf{q}_{s j}^k \quad (2.29)$$

where $\mathbf{K}^{i j \tau s}$ is the stiffness matrix in the form of the fundamental nuclei. The fundamental nuclei form allows us to obtain finite element matrices in a form that does not depend on the plate theory adopted,(see Carrera (56),(57),(58)). The following notation is introduced to indicate the line integrals along the thickness direction:

$$\begin{aligned} (\mathbf{Z}_{pp}^{k\tau s}, \mathbf{Z}_{pn}^{k\tau s}, \mathbf{Z}_{np}^{k\tau s}, \mathbf{Z}_{nn}^{k\tau s}) &= (\tilde{\mathbf{C}}_{pp}^k, \tilde{\mathbf{C}}_{pn}^k, \tilde{\mathbf{C}}_{np}^k, \tilde{\mathbf{C}}_{nn}^k) E_{\tau s} \\ (\mathbf{Z}_{pn}^{k\tau s,z}, \mathbf{Z}_{nn}^{k\tau s,z}, \mathbf{Z}_{np}^{k\tau s,z}, \mathbf{Z}_{nn}^{k\tau s,z}, \mathbf{Z}_{nn}^{k\tau s,z,z}) &= (\tilde{\mathbf{C}}_{pn}^k E_{\tau s,z}, \tilde{\mathbf{C}}_{nn}^k E_{\tau s,z}, \tilde{\mathbf{C}}_{np}^k E_{\tau,z,s}, \tilde{\mathbf{C}}_{nn}^k E_{\tau,z,s}, \tilde{\mathbf{C}}_{nn}^k E_{\tau,z,s,z}) \\ (E_{\tau s}, E_{\tau s,z}, E_{\tau,z,s}, E_{\tau,z,s,z}) &= \int_{A_k} (F_{\tau} F_s, F_{\tau} F_{s,z}, F_{\tau,z} F_s, F_{\tau,z} F_{s,z}) dz \end{aligned} \quad (2.30)$$

The compact expression of the stiffness matrix is then outlined:

$$\begin{aligned} \mathbf{K}^{k\tau s i j} &= \mathbf{D}_p^T (N_i \mathbf{I}) \left[\mathbf{Z}_{pp}^{k\tau s} \mathbf{D}_p (N_j \mathbf{I}) + \mathbf{Z}_{pn}^{k\tau s} \mathbf{D}_{n\Omega} (N_j \mathbf{I}) + \mathbf{Z}_{pn}^{k\tau s,z} N_j \right] + \\ &+ \mathbf{D}_{n\Omega}^T (N_i \mathbf{I}) \left[\mathbf{Z}_{np}^{k\tau s} \mathbf{D}_p (N_j \mathbf{I}) + \mathbf{Z}_{nn}^{k\tau s} \mathbf{D}_{n\Omega} (N_j \mathbf{I}) + \mathbf{Z}_{nn}^{k\tau s,z} N_j \right] + \\ &+ N_i \left[\mathbf{Z}_{np}^{k\tau s,z} \mathbf{D}_p (N_j \mathbf{I}) + \mathbf{Z}_{nn}^{k\tau s,z} \mathbf{D}_{n\Omega} (N_j \mathbf{I}) + \mathbf{Z}_{nn}^{k\tau s,z,z} N_j \right] \mathbf{D}_{\Omega} \end{aligned} \quad (2.31)$$

The symbols $\triangleleft \dots \triangleright_{\Omega}$ were introduced to denote integrals on Ω^e . The matrix $\mathbf{K}^{\tau sij}$ has 3×3 components and the 9 terms of $\mathbf{K}^{\tau sij}$ are:

$$\begin{aligned}
 \mathbf{K}_{xx}^{k\tau sij} &= \tilde{\mathbf{Z}}_{pp11}^{k\tau s} \triangleleft N_{i,x} N_{j,x} \triangleright_{\Omega} + \tilde{\mathbf{Z}}_{pp16}^{k\tau s} \triangleleft N_{i,y} N_{j,x} \triangleright_{\Omega} + \tilde{\mathbf{Z}}_{pp16}^{k\tau s} \triangleleft N_{i,x} N_{j,y} \triangleright_{\Omega} + \\
 &\quad + \tilde{\mathbf{Z}}_{pp66}^{k\tau s} \triangleleft N_{i,y} N_{j,y} \triangleright_{\Omega} + \tilde{\mathbf{Z}}_{nn55}^{k\tau, z^s, z} \triangleleft N_i N_j \triangleright_{\Omega} \\
 \mathbf{K}_{xy}^{k\tau sij} &= \tilde{\mathbf{Z}}_{pp12}^{k\tau s} \triangleleft N_{i,x} N_{j,y} \triangleright_{\Omega} + \tilde{\mathbf{Z}}_{pp26}^{k\tau s} \triangleleft N_{i,y} N_{j,y} \triangleright_{\Omega} + \tilde{\mathbf{Z}}_{pp16}^{k\tau s} \triangleleft N_{i,x} N_{j,x} \triangleright_{\Omega} + \\
 &\quad + \tilde{\mathbf{Z}}_{pp66}^{k\tau s} \triangleleft N_{i,y} N_{j,x} \triangleright_{\Omega} + \tilde{\mathbf{Z}}_{nn45}^{k\tau, z^s, z} \triangleleft N_i N_j \triangleright_{\Omega} \\
 \mathbf{K}_{xz}^{k\tau sij} &= \tilde{\mathbf{Z}}_{pn13}^{k\tau s, z} \triangleleft N_{i,x} N_j \triangleright_{\Omega} + \tilde{\mathbf{Z}}_{pn36}^{k\tau s, z} \triangleleft N_{i,y} N_j \triangleright_{\Omega} + \tilde{\mathbf{Z}}_{nn55}^{k\tau, z^s} \triangleleft N_i N_{j,x} \triangleright_{\Omega} + \\
 &\quad + \tilde{\mathbf{Z}}_{nn45}^{k\tau, z^s} \triangleleft N_i N_{j,y} \triangleright_{\Omega} \\
 \mathbf{K}_{yx}^{k\tau sij} &= \tilde{\mathbf{Z}}_{pp12}^{k\tau s} \triangleleft N_{i,y} N_{j,x} \triangleright_{\Omega} + \tilde{\mathbf{Z}}_{pp16}^{k\tau s} \triangleleft N_{i,x} N_{j,x} \triangleright_{\Omega} + \tilde{\mathbf{Z}}_{pp26}^{k\tau s} \triangleleft N_{i,y} N_{j,y} \triangleright_{\Omega} + \\
 &\quad + \tilde{\mathbf{Z}}_{pp66}^{k\tau s} \triangleleft N_{i,x} N_{j,y} \triangleright_{\Omega} + \tilde{\mathbf{Z}}_{nn45}^{k\tau, z^s, z} \triangleleft N_i N_j \triangleright_{\Omega} \\
 \mathbf{K}_{yy}^{k\tau sij} &= \tilde{\mathbf{Z}}_{pp22}^{k\tau s} \triangleleft N_{i,y} N_{j,y} \triangleright_{\Omega} + \tilde{\mathbf{Z}}_{pp26}^{k\tau s} \triangleleft N_{i,x} N_{j,y} \triangleright_{\Omega} + \tilde{\mathbf{Z}}_{pp26}^{k\tau s} \triangleleft N_{i,y} N_{j,x} \triangleright_{\Omega} + \\
 &\quad + \tilde{\mathbf{Z}}_{pp66}^{k\tau s} \triangleleft N_{i,x} N_{j,x} \triangleright_{\Omega} + \tilde{\mathbf{Z}}_{nn44}^{k\tau, z^s, z} \triangleleft N_i N_j \triangleright_{\Omega} \\
 \mathbf{K}_{yz}^{k\tau sij} &= \tilde{\mathbf{Z}}_{pn23}^{k\tau s, z} \triangleleft N_{i,y} N_j \triangleright_{\Omega} + \tilde{\mathbf{Z}}_{pn36}^{k\tau s, z} \triangleleft N_{i,x} N_j \triangleright_{\Omega} + \tilde{\mathbf{Z}}_{nn45}^{k\tau, z^s} \triangleleft N_i N_{j,x} \triangleright_{\Omega} + \\
 &\quad + \tilde{\mathbf{Z}}_{nn44}^{k\tau, z^s} \triangleleft N_i N_{j,y} \triangleright_{\Omega} \\
 \mathbf{K}_{zx}^{k\tau sij} &= \tilde{\mathbf{Z}}_{nn55}^{k\tau s, z^k} \triangleleft N_{i,x} N_j \triangleright_{\Omega} + \tilde{\mathbf{Z}}_{nn45}^{k\tau s, z^k} \triangleleft N_{i,y} N_j \triangleright_{\Omega} + \tilde{\mathbf{Z}}_{np13}^{k\tau, z^s} \triangleleft N_i N_{j,x} \triangleright_{\Omega} + \\
 &\quad + \tilde{\mathbf{Z}}_{np36}^{k\tau, z^s} \triangleleft N_i N_{j,y} \triangleright_{\Omega} \\
 \mathbf{K}_{zy}^{k\tau sij} &= \tilde{\mathbf{Z}}_{nn45}^{k\tau s, z^k} \triangleleft N_{i,x} N_j \triangleright_{\Omega} + \tilde{\mathbf{Z}}_{nn44}^{k\tau s, z^k} \triangleleft N_{i,y} N_j \triangleright_{\Omega} + \tilde{\mathbf{Z}}_{np23}^{k\tau, z^s} \triangleleft N_i N_{j,y} \triangleright_{\Omega} + \\
 &\quad + \tilde{\mathbf{Z}}_{np36}^{k\tau, z^s} \triangleleft N_i N_{j,x} \triangleright_{\Omega} \\
 \mathbf{K}_{zz}^{k\tau sij} &= \tilde{\mathbf{Z}}_{nn55}^{k\tau sk} \triangleleft N_{i,x} N_{j,x} \triangleright_{\Omega} + \tilde{\mathbf{Z}}_{nn45}^{k\tau sk} \triangleleft N_{i,y} N_{j,x} \triangleright_{\Omega} + \tilde{\mathbf{Z}}_{nn45}^{k\tau sk} \triangleleft N_{i,x} N_{j,y} \triangleright_{\Omega} + \\
 &\quad + \tilde{\mathbf{Z}}_{nn44}^{k\tau sk} \triangleleft N_{i,y} N_{j,y} \triangleright_{\Omega} + \tilde{\mathbf{Z}}_{nn33}^{k\tau, z^s, z} \triangleleft N_i N_j \triangleright_{\Omega}
 \end{aligned} \tag{2.32}$$

It should be noted that no assumptions on the approximation order were made. It is therefore possible to obtain refined plate models without changing the formal expression of the fundamental nuclei.

The loading vector, which is variationally consistent with the model, is derived in the case of a generic concentrate load \mathbf{P} :

$$\mathbf{P}^k = \left\{ P_{u_x}^k \quad P_{u_y}^k \quad P_{u_z}^k \right\} \tag{2.33}$$

Any other loading condition can be similarly treated as is usual in FE applications. The virtual work due to \mathbf{P} is :

$$\delta L_{ext}^k = \mathbf{P}^k \delta \mathbf{u}^{kT} \tag{2.34}$$

Substituting Eq. (2.26), the previous equation becomes:

$$\delta L_{ext}^k = F_{\tau} N_i \mathbf{P}^k \delta \mathbf{q}_{\tau i}^{kT} \tag{2.35}$$

The latter equation permits the identification of the components of the nuclei which have to be loaded. In the case of a first-order expansion and \mathbf{P} applied to a node and acting along the x direction, the virtual external work is:

$$\delta L_{ext}^k = P_{u_x} \delta u_{x1}^k + z_p P_{u_x} \delta u_{x2}^k \quad (2.36)$$

where z_p is the thickness coordinate of the loading application point.

2.5 Approach for Evaluating Various Plate Models

Using the Carrera Unified Formulation and starting from the work of Carrera and Petrolo (61) it is possible to build for a given problem reduced theories. These theories are able to preserve the accuracy of the refined model with a lower computational cost. Starting from the refined model it is possible to follow two different ways to build reduced plate theories:

- Evaluate the influence of each term.
- Genetic optimization method.

In the following paragraph the two methods will be described.

2.5.1 Influence of each term.

The aim of this method is to better understand the influence of each term of the Taylor expansion in order to evaluate which variables are needed and which are not. The models on which the investigation has been carried out are Equivalent Single Layer. The effectiveness of each term is investigated as follows:

1. The problem data are fixed (i.e. geometry, boundary conditions, loadings, materials).
2. A set of output variables is chosen (e.g. maximum displacement, stress/displacement component at a given point).
3. A theory is chosen, that is, the terms that have to be considered in the expansion of u_x , u_y and u_z are established.
4. A reference solution is used to establish the accuracy (the current $N = 4$ Layer Wise case is assumed as the best-reference result).
5. CUF is used to generate the finite element solution for the theories considered.
6. The effectiveness of each term is numerically established by measuring the error produced with respect to the reference solution.
7. Any term which does not give any contribution to the computation of the mechanical response is not considered as effective in the plate model.

8. The most suitable plate model is then detected for a given structural layout, in other words, the plate model requiring the lowest number of terms to accomplish a given accuracy is built.

A graphic and numerical notation is introduced to make the representation of the obtained results more readable. Table 2.1 shows all the 15 terms of the expansion. Table 2.2 present the numerical representation of the different terms. The fourth-order model, $N = 4$, is related to the following expression:

$$\begin{aligned}
 u_x &= u_{x1} + z u_{x2} + z^2 u_{x3} + z^3 u_{x4} + z^4 u_{x5} \\
 u_y &= u_{y1} + z u_{y2} + z^2 u_{y3} + z^3 u_{y4} + z^4 u_{y5} \\
 u_z &= u_{z1} + z u_{z2} + z^2 u_{z3} + z^3 u_{z4} + z^4 u_{z5}
 \end{aligned}
 \tag{2.37}$$

The first three terms are constant (the 1st column), the second three terms are linear (the 2nd

Table 2.1 Locations of the displacement.

$N = 0$	$N = 1$	$N = 2$	$N = 3$	$N = 4$
u_{x1}	u_{x2}	u_{x3}	u_{x4}	u_{x5}
u_{y1}	u_{y2}	u_{y3}	u_{y4}	u_{y5}
u_{z1}	u_{z2}	u_{z3}	u_{z4}	u_{z5}

Table 2.2 Numeric representation of the displacement terms

1	4	7	10	13
2	5	8	11	14
3	6	9	12	15

Table 2.3 Symbolic representation of the reduced kinematic model with u_{y3} discarded.

●	●	●	●	●
●	●	○	●	●
●	●	●	●	●

column), the third three terms are parabolic (the 3rd column), the fourth three terms are cubic (the 4th column) and the last three terms are fourth-order displacement variables (the 5th column). A set of symbols are used to denote the active and inactive terms. Each adopted symbol is related to a given structural case. The black colour indicates that the term is active, that is, the displacement variable is exploited to compute the results while the white color indicates that the term is inactive, that is, the displacement variable is removed from the displacement model. Table 2.3 shows the case where the parabolic term of the in-plane displacement of the

expansion in the y -direction is discarded. The explicit displacement model related to Table 2.3 is:

$$\begin{aligned} u_x &= u_{x1} + z u_{x2} + z^2 u_{x3} + z^3 u_{x4} + z^4 u_{x5} \\ u_y &= u_{y1} + z u_{y2} + \quad \quad \quad + z^3 u_{y4} + z^4 u_{y5} \\ u_z &= u_{z1} + z u_{z2} + z^2 u_{z3} + z^3 u_{z4} + z^4 u_{z5} \end{aligned} \quad (2.38)$$

The elimination of a term, as well as the evaluation of its effectiveness in the analysis, can be obtained either by rearranging the rows and columns of the stiffness matrix or by exploiting a penalty technique. The accuracy of a reduced model is evaluated by computing the errors E_u and E_σ . These quantities are defined according to the following formulas:

$$E_{u_z} = \left\| \frac{u_z - u_{zref}}{u_{zref}} \right\| \times 100 \quad E_{\sigma_{zz}} = \left\| \frac{\sigma_{zz} - \sigma_{zzref}}{\sigma_{zzref}} \right\| \times 100 \quad (2.39)$$

where u_{zref} and σ_{zzref} denote the transversal displacement and stress values computed through a Layer Wise Fourth-Order model. A displacement variable of the expansion is considered to be non-effective with respect to a specific output component when, if discarded (removed from the formulation), it does not introduce an error in the results according to an accepted error value. The value of the accepted error is chosen as the error committed by the Equivalent Single Layer model with all fifteen terms active with respect to the reference model, that is, the Layer Wise Fourth-Order model.

$$E_{u_z}^A = \left\| \frac{u_{zN4} - u_{zref}}{u_{zref}} \right\| \times 100 \quad E_{\sigma_{zz}}^A = \left\| \frac{\sigma_{zzN4} - \sigma_{zzref}}{\sigma_{zzref}} \right\| \times 100 \quad (2.40)$$

where u_{zN4} and σ_{zzN4} represent the value determined through the Equivalent Single Layer model with all fifteen terms active. The approach described allows us to build plate models which are equivalent to a full Layer Wise higher-order model ($N = 4$ Layer Wise in this paper) (59) having a lower number of displacement variables. A further analysis is then conducted on the reduced models by varying the accepted error. This allows us to build a diagram consisting of a "number of terms vs. error" curve which can be useful to determine the effectiveness of a given theory in terms of accuracy and computational cost.

2.5.2 Genetic optimization method

The aim of this method is to apply an optimization process in order to identify the refined plate theories. The refined plate model have been compute as follows:

1. The problem data are fixed (i.e. geometry, boundary conditions, loadings, materials).
2. A set of output variables is chosen (e.g. maximum displacement, stress/displacement component at a given point).
3. A theory is chosen, that is, the terms that have to be considered in the expansion of u_x , u_y and u_z are established.

4. A reference solution is used to establish the accuracy (the current $N = 4$ Layer Wise case is assumed to be the best-reference result).
5. CUF is used to generate the finite element solution for the theories considered.
6. The accuracy of each model is numerically established by measuring the error produced with respect to the reference solution.
7. An evolutionary multi-objective optimization process has been used.

The genetic algorithms are inspired by the evolution theory explained in "The origin of species". In nature, weak and unfit individuals within their environment are faced with extinction by natural selection. The strong ones have a greater opportunity to pass their genes down to future generations via reproduction. In the long run, the species carrying the correct combination in their genes become dominant in their population. Sometimes, during the slow process of evolution, random changes may occur in the genes. If these changes provide additional advantages within the challenge of survival, new species evolve from the old ones. Unsuccessful changes are eliminated by natural selection. In genetic algorithm terminology, a solution vector $\mathbf{x} \in \mathbf{X}$, where \mathbf{X} is the solution space, is called *individual* or *chromosome*. Chromosomes are made of discrete units called *genes*. Each gene controls one or more features of the chromosome. Genetic algorithms use two operators to generate new solutions from existing ones : *crossover* and *mutation*. The crossover operation is the most important operator of genetic algorithms. In crossover, generally two chromosomes, called *parents*, are combined together to form a new chromosome called *offspring*. The parents are selected among existing chromosomes in the population with the preferences towards fitness, so that the offspring is expected to inherit the good genes which make the parents fit. The mutation operators introduce random changes into the characteristics of the chromosome. Mutation is generally applied at gene level. Having chosen the crossover and mutation operator, it is necessary to identify a method to rank the individuals in order to reward the best and kill the worst. Each plate theory has been considered as an individual. The genes are the terms of the expansion along the thickness of the three displacements. Each gene can be active or not active to identify different displacement fields in this manner. The deactivation of a term can be obtained, either by rearranging the rows and columns of the stiffness matrix or by exploiting a penalty technique. A graphical notation is introduced to make the representation of the plate theories more readable. Fig. 2.3 shows all the 15 terms of the expansion. The fourth-order model, $N = 4$, is related to expression (2.41)

$$\begin{aligned}
 u_x &= u_{x0} + z u_{x1} + z^2 u_{x2} + z^3 u_{x3} + z^4 u_{x4} \\
 u_y &= u_{y0} + z u_{y1} + z^2 u_{y2} + z^3 u_{y3} + z^4 u_{y4} \\
 u_z &= u_{z0} + z u_{z1} + z^2 u_{z2} + z^3 u_{z3} + z^4 u_{z4}
 \end{aligned} \tag{2.41}$$

The first three terms are constant (the first column), the second three terms are linear (the 2nd column), the third three terms are parabolic (the 3rd column), the fourth three terms are cubic (the 4th column) and the last three terms are fourth-order displacement variables (the 5th column). The total number of expansion terms is 15. The matrix representation has been changed in a vectorial representation (see Fig. 2.3) in order to simplify the explanation of the operations

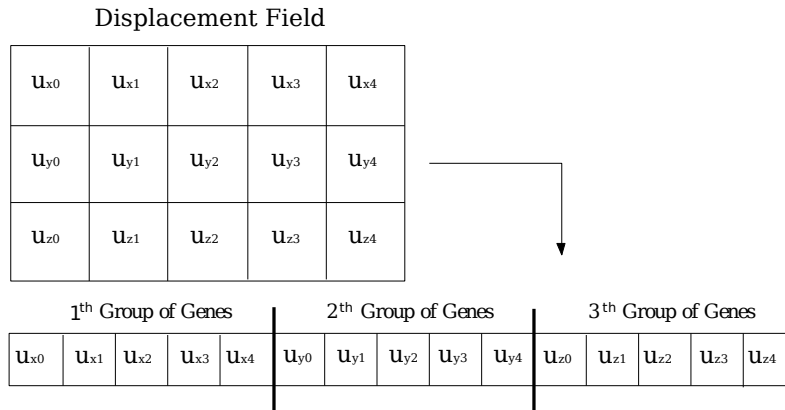


Figure 2.3 Graphical representation of a plate theory

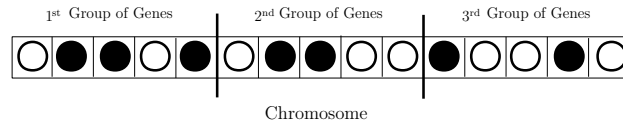


Figure 2.4 Genetic representation of a plate theory

of crossover and mutation and in order to better identify the single chromosome and the single genes. A set of symbols are used to denote the active and inactive terms. The black color indicates that the term is active, that is, the displacement variable is exploited to compute the results while the white color indicates that the term is inactive, that is, the displacement variable is removed from the displacement model. In Fig. 2.4 the following plate theory is represented:

$$\begin{aligned}
 u_x(x, y, z) &= zu_{x1}(x, y) + z^2u_{x2}(x, y) + z^4u_{x4} \\
 u_y(x, y, z) &= zu_{y1}(x, y) + z^2u_{y2}(x, y) \\
 u_z(x, y, z) &= u_{z0}(x, y) + z^3u_{z3}(x, y)
 \end{aligned}
 \tag{2.42}$$

In Fig. 2.5 the reproduction of two chromosomes is represented, in order to better illustrate the crossover operator. The two chromosome parents generate their offspring by exchanging the group of genes. The individual genes have been divided into three groups of five genes. In Fig. 2.5 the vertical bars show where the parents have been cut for the reproduction process. The sons are formed by the casual recombination of the parent group of genes. This procedure leads to the birth of twins. A control algorithm has been developed in order to find and kill the twins, because copies of the same individual increase the computational times without advantages. The mutation operates on the single chromosome at gene level with random modification. The mutation operator makes minimal changes. In Fig. 2.6 the mutation of a chromosome is represented. The two arrows show which genes have been modified. The original chromosome indicates the displacement field of equation (2.42) while the mutated chromosome represents the following plate theories:

$$\begin{aligned}
 u_x(x, y, z) &= zu_{x1}(x, y) + z^2u_{x2}(x, y) + z^3u_{x3} + z^4u_{x4} \\
 u_y(x, y, z) &= zu_{y1}(x, y) + z^2u_{y2}(x, y) + z^4u_{y4} \\
 u_z(x, y, z) &= u_{z0}(x, y) + z^3u_{z3}(x, y)
 \end{aligned}
 \tag{2.43}$$

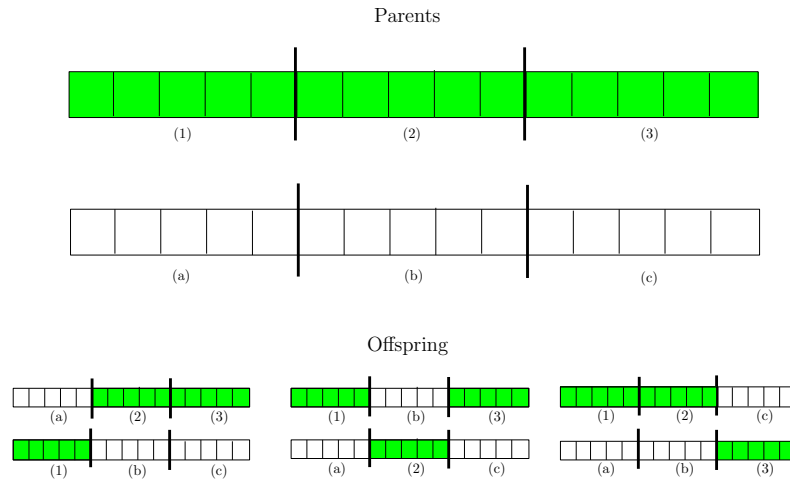


Figure 2.5 Reproduction of two individuals.

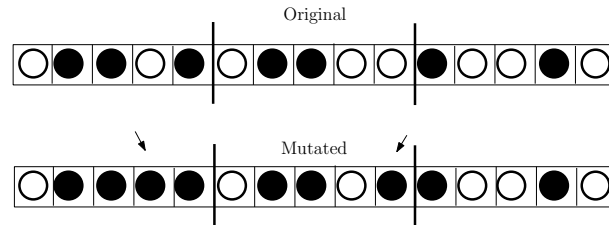


Figure 2.6 Mutation

The mutation operator introduces a certain degree of genetic variability in the population which is useful to explore the solution space more efficiently. In fact, it forces a new genetic configuration into the population which can be potentially better than the existing one. The mutation operator acts randomly, modifying a number of individuals in each generation. The mutation intensity, which determines the number of mutations for each individual, varies randomly for each generation from a minimum of one to a maximum of five in order to increase the convergence velocity. Each individual created by the forementioned methodology reported before is characterized by the number of active terms and by an error committed in computing the required output. The error of individuals, that is, the error of the reduced models is evaluated through the following formulas:

$$E_{\sigma_{xx}} = \frac{\sum_0^h \|\sigma_{xx_z} - \sigma_{xx_{refz}}\|}{N} \quad (2.44)$$

where $\sigma_{xx_{ref}}$ denote stress values computed through a Layer Wise Fourth-Order model and N the number of points used to discretized the stress along the thickness. The error computed has been adimensionalised through $\sigma_{xx_{refmax}}$. The reduced model population can be represented by using the number of active terms and the error (see Fig. 2.7 (a)). Each plate theory has a fitness value based on its rank in the population, not its actual objective function value. Note that herein all objectives are assumed to be minimized. The population is ranked according

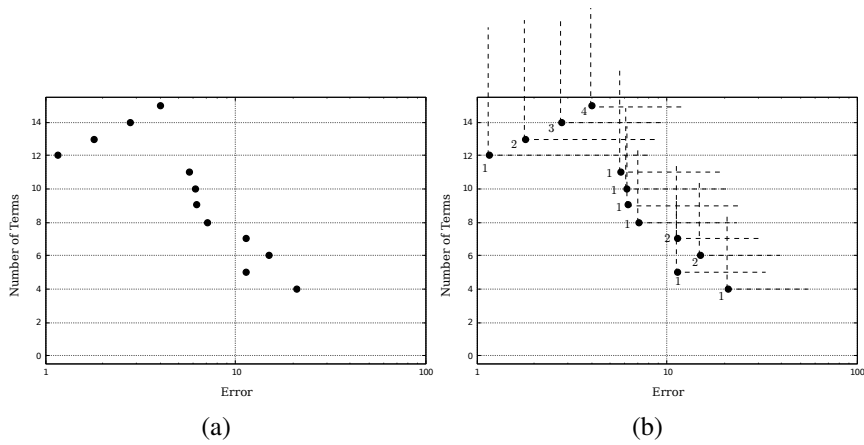


Figure 2.7 An example of population representation

to dominance rule (Fonseca (73)). The fitness of each chromosome is evaluated through the following formula :

$$r_i(\mathbf{x}_i, t) = 1 + nq(\mathbf{x}_i, t) \quad (2.45)$$

where $nq(\mathbf{x}, t)$ is the number of solutions dominating solution \mathbf{x} at generation t . In Fig. 2.7 (b) the dominance area of each individual and its fitness is presented. Each individual has a dominance area, the dot line, and the fitness of a single chromosome is related to the number of dominance areas in which it is through equation (2.45). A lower rank corresponds to a better solution. The fitness of each chromosome determines the number of sons that the chromosome is able to generate in order to reward the best chromosome and penalize the worst. In fact the number of sons that a chromosome can generate is inversely proportional to its fitness. The individuals with the highest fitness are the ones on the Pareto front. In the present example the solution space is bi-dimensional, that is number of terms versus error in computing a single variable, in order to better explain the methodology. It can become n-dimensional in order to identify the best reduced models able to compute different outputs at the same time.

Chapter 3

Electro-mechanical formulation

3.1 Piezoelectric materials

Piezoelectric materials have the ability to convert mechanical energy into electrical energy, and vice versa, the ability to convert electrical energy into mechanical energy. In 1880 Pierre and Jacques Curie discovered that certain crystals produce an electrical charge under deformation, where the amount of charge depends on the deformation magnitude. This effect, which is shown in Fig. 3.1, is called the direct piezoelectric effect. The inverse of the direct effect, the so-called converse piezoelectric effect, was demonstrated by the Curie brothers in 1881, after Gabriel Lippman deduced it from thermodynamic principles. The converse effect is that such a crystal is deformed when an electric field is applied. The crystalline materials that show

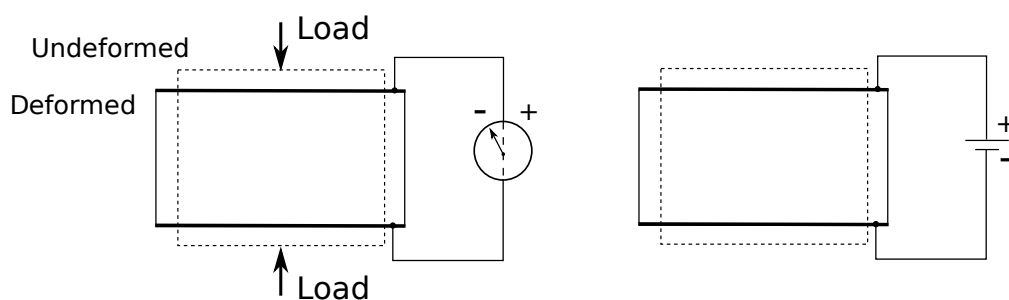


Figure 3.1 The direct and converse piezoelectric effects

piezoelectric properties can be divided in two classes. First are the natural crystals, e.g. Quartz (SiO_2), Rochelle Salt ($KNa(C_4H_4O_6) \times 4H_2O$) or Tourmaline ($SiO_2 + B, Al$) and second are the manufactured ceramics of which typical representants are Barium Titanate ($BaTiO_3$) and Lead Zirconate Titanate (PZT). The latter group usually offers a much higher piezoelectric response than the natural crystals and are today commonly considered for application. A second group is built by the piezoelectric polymers, semi-crystalline polymers with ferroelectric properties, the most commonly used representative of which is polyvinylidene fluoride (PVDF). The polymer materials generally show lower elastic and lower piezoelectric coefficients. Thus these

Table 3.1 Material properties of selected piezoelectric ceramics (PZT) and polymer (PVDF)

		PZT-5H	PZT-5A	PVDF
E_{11}	<i>GPa</i>	71	69	2
E_{33}	<i>GPa</i>	111	106	2
ν	–	0.31	–	–
ρ	<i>Kg/m³</i>	7450	7700	1800
ϵ_{11}/ϵ_0	–	–	1700	12
ϵ_{33}/ϵ_0	–	3400	1730	12
d_{33}	<i>m/V</i> $\times 10^{-12}$	593	374	–33
d_{31}	<i>m/V</i> $\times 10^{-12}$	–274	–171	23
d_{15}	<i>m/V</i> $\times 10^{-12}$	741	585	–

materials are preferably used for sensor applications. Furthermore they show a high pyroelectricity, an electric reaction depending to the temperature. This effect is not covered in this work. Table 1.1 shows the basic parameters of typical representants of state-of-the-art piezoceramics (PZT) and as a comparison the values for the piezoelectric polymer PVDF. Listed are the elastic moduli E_{11} and E_{33} , the Poisson ratio ν , the density ρ , the relative permittivity ϵ_{11}/ϵ_0 and ϵ_{33}/ϵ_0 with $\epsilon_0 = 8.85 \times 10^{12} \text{ As/Vm}$, the piezoelectric coefficients d_{33} , d_{31} and d_{15} and the Curie temperature TC. The data is taken from (74), not all parameters are available. An extensive description of piezoelectric materials, including the influence of the different crystal configurations can be found in Ikeda (75). The piezoelectric effect is related to a polarization of the crystalline material. In untreated condition, the piezoelectric materials are not polarized and thus do not show piezoelectric reactions. Although on the microscopic level polarized domains exist, their directions are randomly distributed. To activate the materials, an external polarization is necessary. If a sufficiently high electric field, expressed by the potential ϕ_P , is applied on the crystalline material, the domains reorder more or less in the same direction and the macroscopic polarization is produced. In the process of the polarization, in industry often referred to as poling, the material experiences a deformation. After the poling the material has a remanent polarization and a remanent elongation. In this activated state, any applied potential lower than the polarization potential ϕ_P leads to a temporary deformation and vice versa.

3.2 Generalized Hooke's law

In a three-dimensional Cartesian coordinate system, it is customary to describe the state of deformation by six components of strain and stress (see Fig. 3.2). A linear relation between the six stresses and six strain is known as the generalized Hook's law, and it can be expressed as,

$$\sigma_k = C_{kj}\epsilon_j \quad k = 1, 2, \dots, 6 \quad (3.1)$$

In the homogeneous materials C_{kj} is constant throughout the material. C_{kj} are entries in the k – th row and j – th column of a 6×6 square matrix, but C_{kj} are not components of a second-order tensor. The single subscript notation for stress and strain components is based on the

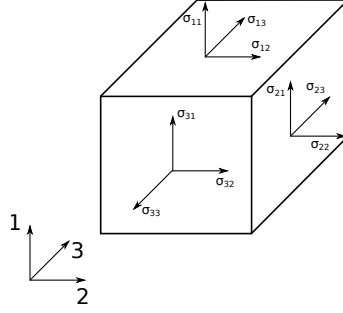


Figure 3.2 Components of stress in a rectangular cartesian coordinate systems

convention,

$$\begin{aligned} \sigma_1 &= \sigma_{11}, \quad \sigma_2 = \sigma_{22}, \quad \sigma_3 = \sigma_{33}, \quad \sigma_4 = \sigma_{12}, \quad \sigma_5 = \sigma_{13}, \quad \sigma_6 = \sigma_{23} \\ \epsilon_1 &= \epsilon_{11}, \quad \epsilon_2 = \epsilon_{22}, \quad \epsilon_3 = \epsilon_{33}, \quad \epsilon_4 = 2\epsilon_{12}, \quad \epsilon_5 = 2\epsilon_{13}, \quad \epsilon_6 = 2\epsilon_{23} \end{aligned} \quad (3.2)$$

$(\sigma_1, \sigma_2, \sigma_4)$ are the section stresses and $(\sigma_3, \sigma_5, \sigma_6)$ are out of section stresses. Similar terminology is used for the strain components. The thirty six coefficients C_{ij} are not all independent of each other. The number of independent constants depends no the material constitution. For material for which the strain energy density function U_0 is such that

$$\frac{\partial U_0}{\partial \epsilon_k} = \sigma_k \quad (3.3)$$

the coefficient $C_{kj} = C_{jk}$. The strain energy density of the material may be expressed as

$$U_0 = \int_0^{\epsilon_k} \sigma_k d\epsilon_k \quad (3.4)$$

Substituting Eq. 3.1 into Eq. 3.4 and integrating

$$U_0 = \frac{1}{2} C_{kj} \epsilon_k \epsilon_j \quad (3.5)$$

substituting for U_0 from Eq. 3.5 into Eq. 3.3, we arrive at the expression

$$\sigma_k = \frac{1}{2} (C_{kj} + C_{jk}) \epsilon_j \quad (3.6)$$

By comparing expression 3.6 and 3.1 it is possible to conclude that $C_{kj} = C_{jk}$. Because of this symmetry, there are only twenty-one independent elastic constants for anisotropic materials. In matrix form equation 3.1 can be expressed as

$$\begin{Bmatrix} \sigma_1 \\ \sigma_2 \\ \sigma_3 \\ \sigma_4 \\ \sigma_5 \\ \sigma_6 \end{Bmatrix} = \begin{bmatrix} C_{11} & C_{12} & C_{13} & C_{14} & C_{15} & C_{16} \\ & C_{22} & C_{23} & C_{24} & C_{25} & C_{26} \\ & & C_{33} & C_{34} & C_{35} & C_{36} \\ & & & C_{44} & C_{45} & C_{46} \\ & & & & C_{55} & C_{56} \\ & & & & & C_{66} \end{bmatrix} \begin{Bmatrix} \epsilon_1 \\ \epsilon_2 \\ \epsilon_3 \\ \epsilon_4 \\ \epsilon_5 \\ \epsilon_6 \end{Bmatrix} \quad (3.7)$$

sym.

It is understood from Eq. 3.7 that, in general, the elastic coefficients C_{ij} relating the Cartesian components of stress and strain depend on the coordinates systems (x_1, x_2, x_3) used. Referred to another Cartesian coordinate system $(\bar{x}_1, \bar{x}_2, \bar{x}_3)$, the elastic coefficient are \bar{C}_{ij} , and in general $\bar{C}_{ij} \neq C_{ij}$. If $\bar{C}_{ij} = C_{ij}$ then they are independent of the coordinate systems and the material is said to be isotropic.

Monoclinic materials Some anisotropic materials may possess material symmetries and their constitutive behaviour can be described with fewer than twenty-one constants. When the elastic coefficients at a point have the same values for every pair of coordinates systems which are mirror images of each other in a certain plane, that plane is called a plane of elastic symmetry for the material at that point. Material with one plane of symmetry are called monoclinic materials, and the number of elastic coefficients for such materials reduce to thirteen. If the plane of symmetry is $x_3 = 0$, the constitutive equation relations become:

$$\begin{pmatrix} \sigma_1 \\ \sigma_2 \\ \sigma_3 \\ \sigma_4 \\ \sigma_5 \\ \sigma_6 \end{pmatrix} = \begin{bmatrix} C_{11} & C_{12} & C_{13} & 0 & 0 & C_{16} \\ & C_{22} & C_{23} & 0 & 0 & C_{26} \\ & & C_{33} & 0 & 0 & C_{36} \\ & & & C_{44} & C_{45} & 0 \\ & & & & C_{55} & 0 \\ & & sym. & & & C_{66} \end{bmatrix} \begin{pmatrix} \epsilon_1 \\ \epsilon_2 \\ \epsilon_3 \\ \epsilon_4 \\ \epsilon_5 \\ \epsilon_6 \end{pmatrix} \quad (3.8)$$

Orthotropic materials If the material systems has three mutually perpendicular planes of elastic symmetry, then the number of independent elastic coefficients can be reduced to nine. Such material are referred as orthotropic. The stress-strain relations for an orthotropic materials are given by

$$\begin{pmatrix} \sigma_1 \\ \sigma_2 \\ \sigma_3 \\ \sigma_4 \\ \sigma_5 \\ \sigma_6 \end{pmatrix} = \begin{bmatrix} C_{11} & C_{12} & C_{13} & 0 & 0 & 0 \\ & C_{22} & C_{23} & 0 & 0 & 0 \\ & & C_{33} & 0 & 0 & 0 \\ & & & C_{44} & 0 & 0 \\ & & & & C_{55} & 0 \\ & & sym. & & & C_{66} \end{bmatrix} \begin{pmatrix} \epsilon_1 \\ \epsilon_2 \\ \epsilon_3 \\ \epsilon_4 \\ \epsilon_5 \\ \epsilon_6 \end{pmatrix} \quad (3.9)$$

The stiffness coefficient C_{ij} for an orthotropic material may be expressed in terms of the engineering constants

$$\begin{aligned} C_{11} &= \frac{E_1(1-\nu_{23}\nu_{32})}{\Delta}; & C_{12} &= \frac{E_1(\nu_{21}+\nu_{23}\nu_{31})}{\Delta}; & C_{13} &= \frac{E_1(\nu_{31}+\nu_{21}\nu_{32})}{\Delta}; \\ C_{21} &= \frac{E_2(\nu_{12}+\nu_{13}\nu_{32})}{\Delta}; & C_{22} &= \frac{E_2(1-\nu_{13}\nu_{31})}{\Delta}; & C_{23} &= \frac{E_2(\nu_{32}+\nu_{12}\nu_{31})}{\Delta}; \\ C_{31} &= \frac{E_3(\nu_{13}+\nu_{12}\nu_{23})}{\Delta}; & C_{32} &= \frac{E_3(\nu_{23}+\nu_{13}\nu_{21})}{\Delta}; & C_{33} &= \frac{E_3(1-\nu_{12}\nu_{21})}{\Delta}; \\ C_{44} &= G_{12} & C_{55} &= G_{13} & C_{66} &= G_{23} \end{aligned}$$

$$\Delta = 1 - \nu_{12}\nu_{21} - \nu_{13}\nu_{32} - \nu_{23}\nu_{32} - \nu_{12}\nu_{23}\nu_{31} - \nu_{13}\nu_{21}\nu_{32}$$

(3.10)

where E_i denotes Young's moduli in the i th-material direction, ν_{ij} is the Poisson's ratio for transverse strain in the j -th direction when stressed in the i -th direction

$$\nu_{ij} = -\frac{\epsilon_j}{\epsilon_i} \quad (3.11)$$

and (G_{23}, G_{31}, G_{12}) are the shear moduli in the 2-3, 3-1, and 2-1 planes, respectively. The three material directions (x_1, x_2, x_3) are taken perpendicular to the three planes of elastic symmetry.

Isotropic materials For an isotropic material there are infinite number of planes of elastic symmetry (or no preferred direction), and it can be described in terms of two elastic coefficients. The stress-strain relations for an isotropic material have the form,

$$\begin{Bmatrix} \sigma_1 \\ \sigma_2 \\ \sigma_3 \\ \sigma_4 \\ \sigma_5 \\ \sigma_6 \end{Bmatrix} = \begin{bmatrix} C_{33} & C_{23} & C_{23} & 0 & 0 & 0 \\ & C_{33} & C_{23} & 0 & 0 & 0 \\ & & C_{33} & 0 & 0 & 0 \\ & & & \widehat{C} & 0 & 0 \\ & & & & \widehat{C} & 0 \\ & & & & & \widehat{C} \end{bmatrix} \begin{Bmatrix} \epsilon_1 \\ \epsilon_2 \\ \epsilon_3 \\ \epsilon_4 \\ \epsilon_5 \\ \epsilon_6 \end{Bmatrix} \quad (3.12)$$

where $\widehat{C} = 0.5(C_{33} - C_{23})$. These two coefficients are related to Young's Modulus E and Poisson's ratio ν by

$$C_{33} = \frac{E(1 - \nu)}{(1 + \nu)(1 - 2\nu)} \quad C_{23} = \frac{\nu E}{(1 + \nu)(1 - 2\nu)} \quad (3.13)$$

Transformation of material coefficients The constitutive relations in the previous paragraph for an orthotropic material were written in terms of stress and strain components that are referred to a coordinates systems which coincides with the principal material coordinate system (x_1, x_2, x_3) . But in the problem formulation the employed coordinates system does not coincide with the principal material one, for example in composite laminates each layer has it material coordinate system, and these have different orientations with respect to the most general laminate coordinates called problem coordinate system (x, y, z) . In Fig. 3.3 the material coordinate

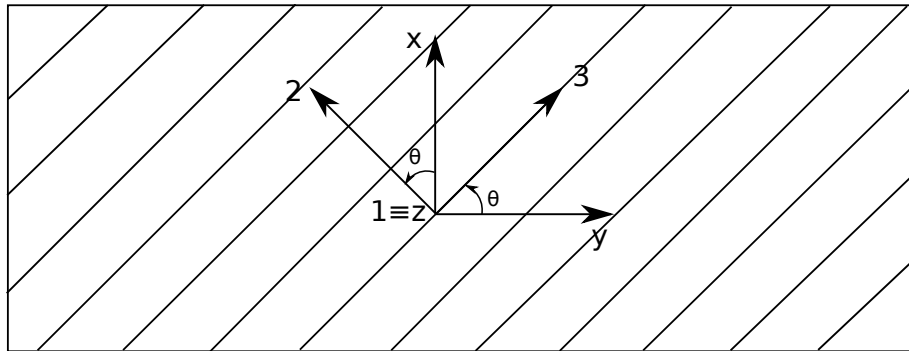


Figure 3.3 Fibre orientation angle

system and the problem coordinates system are clearly indicate for a laminate. The angle θ between the material coordinates (x_1, x_2, x_3) and the problem coordinates (x, y, z) is considered counter-clockwise, the third coordinates coincide $(x_1 = z)$. Each quantity related to material reference systems is indicates by the subscript m , those related to problem reference system by

the subscript p . The stress tensor can be transformed according to:

$$\begin{pmatrix} \sigma_{zz} \\ \sigma_{xx} \\ \sigma_{yy} \\ \sigma_{xz} \\ \sigma_{yz} \\ \sigma_{xy} \end{pmatrix} = \begin{bmatrix} 1 & 0 & 0 & 0 & 0 & 0 \\ 0 & \cos(\theta)^2 & \sin(\theta)^2 & 0 & 0 & -2\cos(\theta)\sin(\theta) \\ 0 & \sin(\theta)^2 & \cos(\theta)^2 & 0 & 0 & 2\cos(\theta)\sin(\theta) \\ 0 & 0 & 0 & \cos(\theta) & -\sin(\theta) & 0 \\ 0 & 0 & 0 & \sin(\theta) & \cos(\theta) & 0 \\ 0 & \cos(\theta)\sin(\theta) & -\sin(\theta)\cos(\theta) & 0 & 0 & \cos(\theta)^2 - \sin(\theta)^2 \end{bmatrix} \begin{pmatrix} \sigma_1 \\ \sigma_2 \\ \sigma_3 \\ \sigma_4 \\ \sigma_5 \\ \sigma_6 \end{pmatrix} \quad (3.14)$$

The Eq. 3.14 in a compact form can be expressed as:

$$\{\sigma\}_p = [T] \{\sigma\}_m \quad (3.15)$$

The same procedure can be applied for the transformation of strain components. Through the matrix $[T]$ it is possible to perform the transformation from the coordinates system to the problem coordinates. The material stiffness C_{ij} can be easily obtain as

$$\{\sigma\}_p = [T] \{\sigma\}_m = [T][C]_m \{\epsilon\}_m = [T][C]_m [T]^T \{\epsilon\}_p = [C]_p \{\epsilon\}_p \quad (3.16)$$

where $[C]_m$ is the 6×6 material stiffness matrix in the material coordinates and $[T]$ is the transformation matrix in Ed. 3.14. It is possible to define $[\tilde{C}]$ as

$$[\tilde{C}] = [T][C][T]^T \quad (3.17)$$

In the case of orthotropic materials the stress-strain relations in the problem coordinates is

$$\begin{pmatrix} \sigma_{zz} \\ \sigma_{xx} \\ \sigma_{zx} \\ \sigma_{zy} \\ \sigma_{xy} \\ \sigma_{yy} \end{pmatrix} = \begin{bmatrix} \tilde{C}_{11} & \tilde{C}_{12} & 0 & 0 & \tilde{C}_{16} & \tilde{C}_{13} \\ \tilde{C}_{21} & \tilde{C}_{22} & 0 & 0 & \tilde{C}_{26} & \tilde{C}_{23} \\ 0 & 0 & \tilde{C}_{44} & \tilde{C}_{45} & 0 & 0 \\ 0 & 0 & \tilde{C}_{54} & \tilde{C}_{55} & 0 & 0 \\ \tilde{C}_{61} & \tilde{C}_{62} & 0 & 0 & \tilde{C}_{66} & \tilde{C}_{63} \\ \tilde{C}_{31} & \tilde{C}_{32} & 0 & 0 & \tilde{C}_{36} & \tilde{C}_{33} \end{bmatrix} \begin{pmatrix} \epsilon_{zz} \\ \epsilon_{xx} \\ \epsilon_{zx} \\ \epsilon_{zy} \\ \epsilon_{xy} \\ \epsilon_{yy} \end{pmatrix} \quad (3.18)$$

where the stress and strain component are reordered in order to divide the in section components and the out of section components according the the system reference of Fig. 3.4.

3.3 Constitutive equations for piezoelectric problems

The coordinate reference frame is shown in Fig. 3.4. In pure mechanical cases the stress, σ , and strain, ϵ , components are grouped as

$$\begin{aligned} \sigma &= \left\{ \sigma_{zz} \ \sigma_{xx} \ \sigma_{zx} \ \sigma_{zy} \ \sigma_{xy} \ \sigma_{yy} \right\}^T \\ \epsilon &= \left\{ \epsilon_{zz} \ \epsilon_{xx} \ \epsilon_{zx} \ \epsilon_{zy} \ \epsilon_{xy} \ \epsilon_{yy} \right\}^T \end{aligned} \quad (3.19)$$

and are related via the Hooke's law

$$\sigma = \tilde{C} \epsilon \quad (3.20)$$

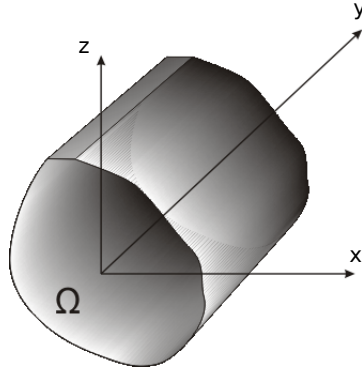


Figure 3.4 Reference systems

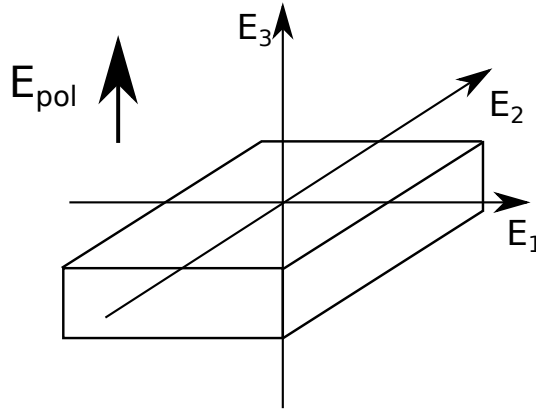


Figure 3.5 Polarization Axes

where \tilde{C} is the elasticity tensor of the materials in the problem reference systems. The electric problem can be described by the electric field strength \mathbf{E} and the dielectric displacement \mathbf{D} . In Fig. 3.5 are reported the polarization axes and the external polarization field used to build the piezo-material. The electrical properties of the piezo-material are expressed in function of the polarization axes of Fig. 3.5.

$$\mathbf{D}_e = \{D_1 \ D_2 \ D_3\}^T \quad \mathbf{E} = \{E_1 \ E_2 \ E_3\}^T \quad (3.21)$$

Their relation in the uncoupled electrical case states is

$$\mathbf{D}_e = \chi \mathbf{E} \quad (3.22)$$

where χ dielectric permittivity tensor of the materials.

$$\chi = \begin{bmatrix} \chi_{11} & \chi_{12} & 0 \\ \chi_{21} & \chi_{22} & 0 \\ 0 & 0 & \chi_{33} \end{bmatrix} \quad (3.23)$$

In the case of piezoelectric materials, the mechanical and the electrical systems are coupled. Therefore the two uncoupled constitutive equations 3.20 and 3.22 have to be extended with coupling terms.

The coupled constitutive equations can take different forms, depending on the used combinations of the variables. The strains can be expressed in terms of the electric field and the dielectric displacement in terms of the stresses using the piezoelectric coefficients d and is thus called d – form:

$$\begin{aligned}\epsilon &= \tilde{\mathbf{S}}\sigma - d^T \mathbf{E} \\ \mathbf{D}_e &= d\sigma + \chi \mathbf{E}\end{aligned}\quad (3.24)$$

where d is :

$$\mathbf{d} = \begin{bmatrix} 0 & 0 & 0 & d_{15} & 0 & 0 \\ 0 & 0 & d_{24} & 0 & 0 & 0 \\ d_{33} & d_{31} & 0 & 0 & 0 & d_{32} \end{bmatrix}\quad (3.25)$$

The most often used formulation is the so called e-form, which relates the mechanic stresses to the electric field and the dielectric displacement to the mechanical strains via the piezoelectric stiffness coefficients e :

$$\begin{aligned}\sigma &= \tilde{\mathbf{C}}\epsilon - e^T \mathbf{E} \\ \mathbf{D}_e &= e\epsilon + \chi \mathbf{E}\end{aligned}\quad (3.26)$$

$\tilde{\mathbf{S}}$ is the compliance tensor, which is the inverse of the elasticity tensor $\tilde{\mathbf{S}} = \tilde{\mathbf{C}}^{-1}$. The piezoelectric coefficient tensor d and the piezoelectric stiffness tensor e have following relation

$$\mathbf{e} = \tilde{\mathbf{C}}\mathbf{d}\quad (3.27)$$

The matrix e is:

$$\mathbf{e} = \begin{bmatrix} 0 & 0 & e_{14} & e_{15} & 0 & 0 \\ 0 & 0 & e_{24} & e_{25} & 0 & 0 \\ e_{33} & e_{32} & 0 & 0 & e_{36} & e_{32} \end{bmatrix}\quad (3.28)$$

where

$$\begin{aligned}e_{33} &= d_{31}\tilde{\mathbf{C}}_{13} + d_{31}\tilde{\mathbf{C}}_{12} + d_{33}\tilde{\mathbf{C}}_{11} \\ e_{31} &= d_{32}\tilde{\mathbf{C}}_{23} + d_{31}\tilde{\mathbf{C}}_{22} + d_{33}\tilde{\mathbf{C}}_{21} \\ e_{36} &= d_{32}\tilde{\mathbf{C}}_{63} + d_{31}\tilde{\mathbf{C}}_{62} + d_{33}\tilde{\mathbf{C}}_{61} \\ e_{32} &= d_{32}\tilde{\mathbf{C}}_{33} + d_{31}\tilde{\mathbf{C}}_{32} + d_{33}\tilde{\mathbf{C}}_{31} \\ e_{14} &= d_{15}\tilde{\mathbf{C}}_{45} & e_{24} &= d_{24}\tilde{\mathbf{C}}_{44} \\ e_{15} &= d_{15}\tilde{\mathbf{C}}_{55} & e_{25} &= d_{24}\tilde{\mathbf{C}}_{54}\end{aligned}\quad (3.29)$$

Both tensors of piezoelectric coefficients have the form 3×6 because they couple the six components of the mechanical strains or stresses to the three components of the electric field or dielectric displacement.

In this work it used the e – form 3.26. Mixing together the strain and stress tensors 3.19 with the electric field and electric displacement tensor 3.21 it is possible to write the constitutive

equation in a compact manner (it is necessary to change the sign in order to be coherent with the 3.26)

$$\bar{\sigma} = \tilde{H}\bar{\epsilon} \quad (3.30)$$

where

$$\begin{aligned} \bar{\sigma} &= \{\sigma_{zz} \ \sigma_{xx} \ \sigma_{zx} \ -D_1 \ -D_3 \ \sigma_{zy} \ \sigma_{xy} \ \sigma_{yy} \ -D_2\}^T \\ \bar{\epsilon} &= \{\epsilon_{zz} \ \epsilon_{xx} \ \epsilon_{zx} \ E_1 \ E_3 \ \epsilon_{zy} \ \epsilon_{xy} \ \epsilon_{yy} \ E_2\}^T \end{aligned} \quad (3.31)$$

and \tilde{H} mix together mechanical constants, electrical constants, and electro-mechanical constants:

$$\tilde{H} = \begin{bmatrix} \tilde{C}_{11} & \tilde{C}_{12} & 0 & 0 & -e_{33} & 0 & \tilde{C}_{16} & \tilde{C}_{13} & 0 \\ \tilde{C}_{21} & \tilde{C}_{22} & 0 & 0 & -e_{31} & 0 & \tilde{C}_{26} & \tilde{C}_{23} & 0 \\ 0 & 0 & \tilde{C}_{44} & -e_{14} & 0 & \tilde{C}_{45} & 0 & 0 & -e_{24} \\ 0 & 0 & -e_{14} & -\chi_{11} & 0 & -e_{15} & 0 & 0 & \chi_{12} \\ -e_{33} & -e_{31} & 0 & 0 & -\chi_{33} & 0 & -e_{36} & -e_{32} & 0 \\ 0 & 0 & \tilde{C}_{54} & -e_{15} & 0 & \tilde{C}_{55} & 0 & 0 & -e_{25} \\ \tilde{C}_{61} & \tilde{C}_{62} & 0 & 0 & -e_{36} & 0 & \tilde{C}_{66} & \tilde{C}_{63} & 0 \\ \tilde{C}_{31} & \tilde{C}_{32} & 0 & 0 & -e_{32} & 0 & \tilde{C}_{36} & \tilde{C}_{33} & 0 \\ 0 & 0 & -e_{24} & -\chi_{12} & 0 & -e_{25} & 0 & 0 & -\chi_{22} \end{bmatrix} \quad (3.32)$$

The strains and the electric field are obtained as:

$$\bar{\epsilon} = D\mathbf{u} \quad (3.33)$$

where

$$\mathbf{u} = \{u_x, u_y, u_z, \phi\} \quad (3.34)$$

and

$$D = \begin{bmatrix} 0 & 0 & \delta_z & 0 \\ \delta_x & 0 & 0 & 0 \\ \delta_z & 0 & \delta_x & 0 \\ 0 & 0 & 0 & -\delta_x \\ 0 & 0 & 0 & -\delta_z \\ 0 & \delta_z & \delta_y & 0 \\ \delta_y & \delta_x & 0 & 0 \\ 0 & \delta_y & 0 & 0 \\ 0 & 0 & 0 & -\delta_y \end{bmatrix} \quad (3.35)$$

3.4 Carrera Unified Formulations - 1D Formulations

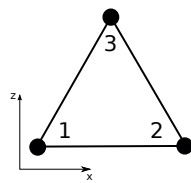
The unified formulation of the beam cross-section unknowns are described by an expansion of generic functions, F_τ ,

$$\mathbf{u} = F_\tau \mathbf{u}_\tau \quad \tau = 1, 2, \dots, M \quad (3.36)$$

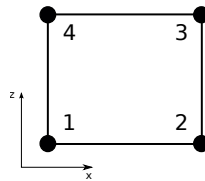
where F_{tau} are the function of the cross-sections coordinates x and z , \mathbf{u}_τ is the unknowns vector, and M stand for the number of the terms expansion. According to the Einstein notation, the

Table 3.2 L3 cross-section element point natural coordinates.

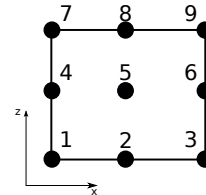
Points	r	s
1	0	0
2	1	0
3	0	1



(a) L3 element.



(b) L4 element



(c) L9 element

Figure 3.6 Cross-section element in actual reference.

repeated subscripted τ indicates summations. The choice of F_{tau} and M is arbitrary, that is, different based functions of any-order can be taken into account to model the unknowns of a beam above the cross-section. Taylor-type expansion have been exploited in the works of Carrera and Giunta (77), Carrera and Petrolo (78), and Carrera et. al (79–82). The Euler-Bernoulli (EBBM) and Timoshenko (TBM) classical theories are derived from the linear Taylor-type expansion. For the electro-mechanical problem the Lagrange polynomial expansion are not a good choice. Lagrange polynomial are herein used to describe the cross-section unknowns.

3.4.1 Lagrange polynomial

Three-,L3, four-,L4 and nine-,L9, polynomials are adopted. L3 polynomials are defined on a triangular domain which is identified by three points. These points define the element that is used to model the displacement field above the cross-section. Similarly, L4 and L9 cross-section elements are defined on quadrilateral domains. The isoperimetrical formulations is exploited. In the case of L3 elements, the interpolation functions are given by Onate (83):

$$F_1 = 1 - r - s \quad F_2 = r \quad F_3 = s \quad (3.37)$$

where r and s belong to the triangular domain defined by the points in Table 3.2. Fig. 3.6 a shows the point locations in actual coordinates. The L4 elements interpolation functions are given by:

$$F_\tau = \frac{1}{4}(1 + rr_\tau)(1 + ss_\tau) \quad \tau = 1, 2, 3, 4 \quad (3.38)$$

where r and s vary from -1 to 1 . Fig. 3.6 b shows the point locations and Table 3.3 reports the point natural coordinates. In the case of a L9 element the interpolation functions are given by:

Table 3.3 L4 cross-section element point natural coordinates.

Points	r	s
1	-1	-1
2	1	-1
3	1	1
4	-1	1

Table 3.4 L4 cross-section element point natural coordinates.

Points	r	s
1	-1	-1
2	0	-1
3	1	-1
4	1	0
5	1	1
6	0	1
7	-1	1
8	-1	0
9	0	0

$$\begin{aligned}
F_\tau &= \frac{1}{4}(r^2 + rr_\tau)(s^2 + ss_\tau) \quad \tau = 1, 3, 5, 7 \\
F_\tau &= \frac{1}{2}s_\tau^2(s^2 - ss_\tau)(1 - r^2) + \frac{1}{2}r_\tau^2(r^2 - rr_\tau)(1 - s^2) \quad \tau = 2, 4, 6, 8 \\
F_\tau &= (1 - r^2)(1 - s^2) \quad \tau = 9
\end{aligned} \tag{3.39}$$

where r and s from 1 to +1. Fig. 3.6 c shows the point locations and Table 3.4 reports the point natural coordinates. The cross-section unknowns given by an L4 element are:

$$\begin{aligned}
u_x &= F_1u_{x1} + F_2u_{x2} + F_3u_{x3} + F_4u_{x4} \\
u_y &= F_1u_{y1} + F_2u_{y2} + F_3u_{y3} + F_4u_{y4} \\
u_z &= F_1u_{z1} + F_2u_{z2} + F_3u_{z3} + F_4u_{z4} \\
\phi &= F_1\phi_1 + F_2\phi_2 + F_3\phi_3 + F_4\phi_4
\end{aligned} \tag{3.40}$$

where u_{x1} , ..., u_{z4} are the displacement variables of the problem and they represent the translational displacement components of each of the four points of the L4 element and ϕ_1 , ..., ϕ_4 are the voltage component of the problem and they represent the voltage component of each of the four points of the L4 elements. The cross-section can be discretized by means of several L-elements. Fig. 3.7 shows the assembly of 2 L9 which share a common edge and three points. The discretization along the beam axis is conducted via a classical finite element approach.

3.5 Finite Element

The unknowns vector is given by:

$$\mathbf{u}_\tau = N_i F_\tau \mathbf{q}_{\tau i} \tag{3.41}$$

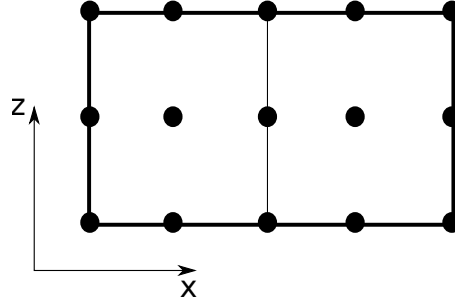


Figure 3.7 Two assembled L9 elements.

where N_i stands for the shape functions and $\mathbf{q}_{\tau i}$ for the nodal unknowns vector:

$$\mathbf{q}_{\tau i} = \{q_{u_{x_{\tau i}}}, q_{u_{y_{\tau i}}}, q_{u_{z_{\tau i}}}, q_{\phi_{\tau i}}\} \quad (3.42)$$

Beam elements with two, B2, three, B3, and four, B4, nodes are here considered whose shape functions are

$$\begin{aligned} N_1 &= \frac{1}{2}(1-r), & N_2 &= \frac{1}{2}(1+r), & \{r_1 = -1, r_2 = 1\} \\ N_1 &= \frac{1}{2}r(r-1), & N_2 &= \frac{1}{2}r(r+1), & N_3 &= -(1+r)(1-r), & \{r_1 = -1, r_2 = 1, r_3 = 0\} \\ N_1 &= -\frac{9}{16}(r + \frac{1}{3})(r - \frac{1}{3})(r - 1), & N_2 &= \frac{9}{16}(r + \frac{1}{3})(r - \frac{1}{3})(r + 1), \\ & & & & & \{r_1 = -1, r_2 = +1, r_3 = -\frac{1}{3}, r_4 = +\frac{1}{3}\} \\ N_3 &= \frac{27}{16}(r+1)(r-\frac{1}{3})(r-1), & N_4 &= -\frac{27}{16}(r+1)(r-\frac{1}{3})(r-1) \end{aligned} \quad (3.43)$$

where the natural coordinate, r , varies from -1 to $+1$ and r_i indicates the position of the node within the natural beam boundaries. The beam model order is given by the expansion on the cross-section, and the number of nodes per each element is related to the approximation along the longitudinal axis. An N -order beam model is therefore a theory that exploits an N -order Lagrange polynomial to describe the kinematics of the beam cross-section.

3.5.1 Stiffness Matrix

The first step in assembling finite element arrays is represented by the use of a proper variational statement. The principle of virtual displacements (PVD) is here exploited

$$\delta L_{int} = \int_V (\delta \boldsymbol{\epsilon}^T \boldsymbol{\sigma}) dV = \delta L_{ext} \quad (3.44)$$

where L_{int} stands for the strain energy, L_{ext} is the work of the external loadings, and δ stands for the virtual variation. Introducing equations 3.30, 3.33, and 3.41 equation 3.44 become

$$\delta L_{int} = \delta \mathbf{q}_{\tau i}^T \int_V (N_i \mathbf{I} F_\tau)^T \mathbf{D}^T \tilde{\mathbf{H}} \mathbf{D} (N_j \mathbf{I} F_s) dV \mathbf{q}_{s j} = \delta L_{ext} \quad (3.45)$$

where

$$\mathbf{I} = \begin{bmatrix} 1 & 0 & 0 & 0 \\ 0 & 1 & 0 & 0 \\ 0 & 0 & 1 & 0 \\ 0 & 0 & 0 & 0 \end{bmatrix} \quad (3.46)$$

From equation 3.45 it is possible to obtain the stiffness matrix written in the form of the fundamental nuclei

$$\mathbf{K}^{ijrs} = \int_V (N_i \mathbf{I} F_\tau)^T \mathbf{D}^T \tilde{\mathbf{H}} \mathbf{D} (N_j \mathbf{I} F_s) dV \quad (3.47)$$

The unified form of the virtual variation of the strain energy can be write as follow.

$$\delta L_{int} = \delta \mathbf{q}_{\tau i}^T \mathbf{K}^{ijrs} \mathbf{q}_{s j} \quad (3.48)$$

Superscripts indicate the four indexes exploited to assemble the matrix: i and j are related to the shape functions, τ and s are related to the expansion functions. The component of the stiffness matrix are reported in the Appendix (mettere riferimento). The fundamental nucleus is a 4×4 array which is formally independent of the order of the beam model and on the choice of the F_τ expansion polynomials.

These are the key-point of CUF which permits, with only nine FORTRAN statements, to implement any-order of multiple class theories. The assembly procedure of the stiffness matrix is based on the use of the four indexes τ , s , i , and j which are opportunely exploited to implement the FORTRAN statements. The core indexes are those related to the expansion functions F_τ and F_s , and the fundamental nucleus is computed by varying τ and s , as shown in Fig. 3.8 where the construction of the so-called τ s -Block, which coincides with the node stiffness matrix, can be observed. Each τ s -Block is then inserted into the element stiffness matrix, as shown in Fig. 3.10. The element stiffness matrix is derived from the assembly of all the ij -Blocks, as shown in Fig. 3.6 Any-order beam theory can be computed since the definition of the order acts on the τ s -loop.

3.5.2 Mass Matrix

The virtual variation of the work of the inertial loadings is

$$\delta L_{ine} = \int_V \rho \ddot{\mathbf{u}} \delta \mathbf{u}^T dV \quad (3.49)$$

where ρ stands for the density of the material, and $\ddot{\mathbf{u}}$ is the acceleration vector. Equation 3.49 can now be rewritten using Eqs. 3.33 and 3.41,

$$\delta L_{ine} = \delta \mathbf{q}_{\tau i}^T \int_V N_i (F_\tau \mathbf{I}) \rho (F_s \mathbf{I}) N_j dV \ddot{\mathbf{q}}_{s j} \quad (3.50)$$

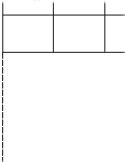


Figure 3.8 Graphic assembly procedure of the node stiffness matrix.

Figure 3.9 Graphic assembly procedure of the element stiffness matrix.

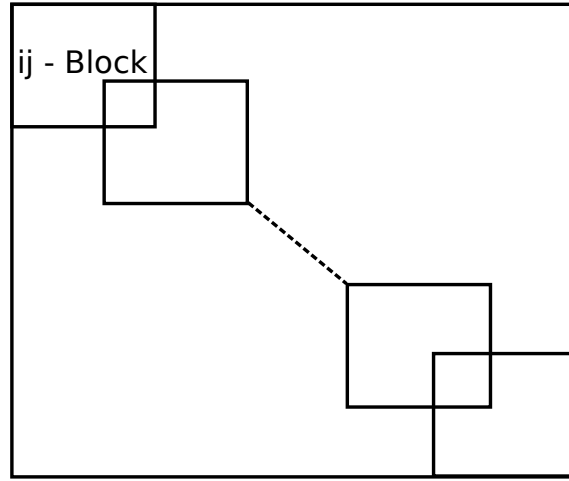


Figure 3.10 Graphic assembly procedure of the element stiffness matrix.

where $\ddot{\mathbf{q}}$ is the nodal acceleration vector and \mathbf{I} is

$$\mathbf{I} = \begin{bmatrix} 1 & 0 & 0 & 0 \\ 0 & 1 & 0 & 0 \\ 0 & 0 & 1 & 0 \\ 0 & 0 & 0 & 0 \end{bmatrix} \quad (3.51)$$

because L_{ine} is not affected by electrical components. The last equation can be rewritten in the following compact manner:

$$\delta L_{ine} = \delta \mathbf{q}_{\tau i}^T \mathbf{M}^{ij\tau s} \ddot{\mathbf{q}}_{s j} \quad (3.52)$$

where $\mathbf{M}^{ij\tau s}$ is the mass matrix in the form of the fundamental nucleus. The dimension of the array is 4×4 . The non-zero components of the matrix are:

$$\mathbf{M}_{11}^{ij\tau s} = \mathbf{M}_{22}^{ij\tau s} = \mathbf{M}_{33}^{ij\tau s} = \rho \int_{\Omega} F_{\tau} F_s d\Omega \int_l N_i N_j dy \quad (3.53)$$

It is possible to see that the fourth terms on the matrix diagonal is zero, because the electrical part is neglected in the mas matrix. The undamped dynamic problem can be written as follows:

$$\mathbf{M}\ddot{\mathbf{a}} + \mathbf{K}\mathbf{a} = \mathbf{p} \quad (3.54)$$

where \mathbf{a} is the vector of the nodal unknowns and \mathbf{p} is the loading vector. Introducing harmonic solutions, it is possible to compute the natural frequencies, ω_i , for the homogenous case, by solving an eigenvalue problem,

$$(-\omega_i^2 \mathbf{M} + \mathbf{K})\mathbf{a}_i = 0 \quad (3.55)$$

where \mathbf{a}_i is the i -th eigenvector.

3.5.3 Loading Vector

The loading vector that is variationally coherent to the model, in the case of a generic concentrated load \mathbf{P} , is

$$\mathbf{P} = \{P_{u_x} P_{u_y} P_{u_z} 0\} \quad (3.56)$$

the virtual work due to \mathbf{P} is

$$\delta L_{ext} = \mathbf{P} \delta \mathbf{u}^T \quad (3.57)$$

the virtual variation of \mathbf{u} in the framework of CUF is

$$\delta L_{ext} = F_\tau \mathbf{P} \delta \mathbf{u}_\tau^T \quad (3.58)$$

by introducing the nodal displacements and the shape functions, the previous equation becomes

$$\delta L_{ext} = F_\tau N_i \mathbf{P} \delta \mathbf{u}_{\tau i}^T \quad (3.59)$$

Chapter 4

Results and discussion

4.1 Influence of each term

4.1.1 Isotropic Plate

An isotropic plate is considered. The Young modulus, E , is equal to 73 [GPa] and the Poisson ratio, ν , is equal to 0.34. The geometry of the plate is shown in Fig. 4.9, where a is 0.1 [m], and b is equal to a . u_z , σ_{xx} , σ_{yy} , and σ_{zz} are computed at $[a/2, b/2, 0]$, while σ_{xz} is computed at $[0, b/2, h/2]$ and σ_{yz} is computed at $[a/2, 0, h/2]$. Stresses are computed through Hooke's laws. Four-node plate elements have been used, and a uniform mesh of 15×15 elements has been adopted after a convergence study.

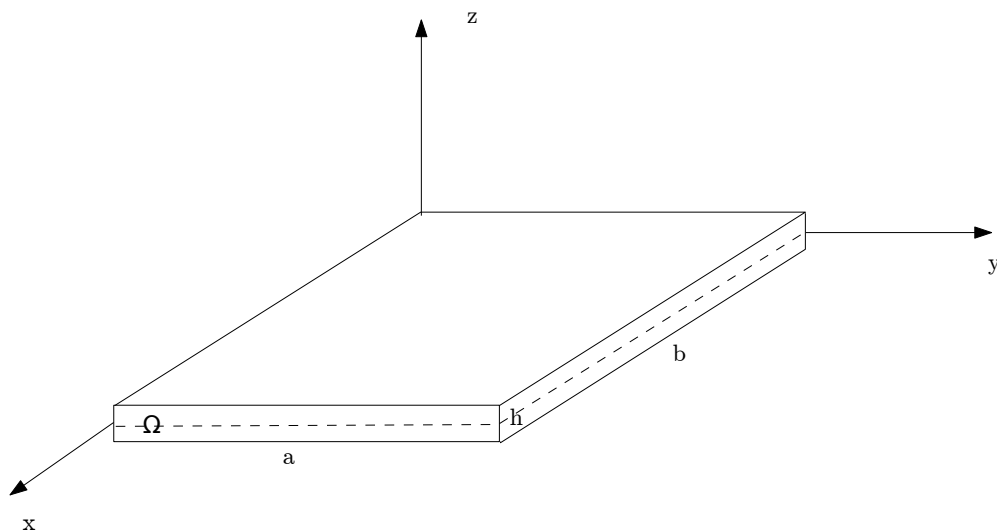


Figure 4.1 Plate geometry.

Boundary Condition Effects The investigation of the role of each displacement variable under different boundary conditions is conducted as a first assessment. Four different boundary condition sets are considered:

1. *ssss*, four simply-supported edges;
2. *cfcf*, two clamped and two free edges;
3. *cccc*, four clamped edges;
4. *scsc*, two simply-supported and two clamped edges.

Fig. 4.2 shows each set and Table 4.1 presents the relative symbolic representation, which is exploited to report the results in a compact manner. A bi-sinusoidal transverse distributed load

Table 4.1 Symbols that indicate the status of a displacement variable for different boundary conditions: clamped, 'c', simply-supported, 's', free, 'f'.

Active term	Inactive term	
▲	△	<i>ssss</i>
■	□	<i>cfcf</i>
▼	▽	<i>cccc</i>
◆	◇	<i>scsc</i>

is applied at the top surface. Its expression is:

$$P_z = p_z \sin\left(\frac{mx}{a}\right) \cos\left(\frac{ny}{b}\right) \quad (4.1)$$

Where p_z is the amplitude and is equal to 1 [kPa]; m and n are the wave numbers in the two in-plane plate directions, both of them are equal to 1. A 3D solution is used to identify which order of the expansion has to be used to obtain 3D-like results, that is, which higher-order plate model is needed to detect a 3D exact solution. Table 4.2 shows the comparison of the 3D solution and the fourth-order FEM one. The fourth-order model solution, $N = 4$,

Table 4.2 Comparison of the the 3D model and the fourth order FEM model solutions in the case of simply-supported plate with a distributed load. $\bar{u}_z = u_z \frac{100E_T h^3}{p_z a^4}$. $\bar{\sigma}_{xx} = \frac{\sigma_{xx}}{\bar{p}_z(a/h)}$. $\bar{\sigma}_{xz} = \frac{\sigma_{xz}}{\bar{p}_z(a/h)^2}$. $\bar{\sigma}_{zz} = \frac{\sigma_{zz}}{\bar{p}_z(a/h)}$.

	$\bar{u}_{zN=4FEM}$	\bar{u}_{z3D}	$\bar{\sigma}_{xxN=4FEM}$	$\bar{\sigma}_{xx3D}$	$\bar{\sigma}_{xzN=4FEM}$	$\bar{\sigma}_{xz3D}$	$\bar{\sigma}_{zzN=4FEM}$	$\bar{\sigma}_{zz3D}$
$a/h = 100$	2.7134	2.7248	0.2040	0.2037	0.2390	0.2387	0.0866	0.0100
$a/h = 10$	2.8255	2.8345	0.2070	0.2068	0.2386	0.2383	0.1041	0.1000
$a/h = 5$	3.1978	3.2056	0.2172	0.2168	0.2378	0.2371	0.2024	0.2002
$a/h = 2$	7.3840	7.3826	0.3171	0.3145	0.2308	0.2277	0.5099	0.5000

offers an excellent match with the exact solution for about all the length-to-thickness ratios and considered outputs, therefore it has been chosen as the reference for the following analyses. The effectiveness of each term is investigated for each set of boundary conditions. Table 4.3 shows the analysis of a moderately thick simply-supported plate. The first column shows the plate models considered. The remaining columns report model accuracies in determining a given output variable compared to a full fourth-order model. Table 4.4 has been obtained by exploiting Table 4.3: the sets of displacement variables which are needed to exactly detect various output variables are given. Each row refers to an output variable. Each column considers a different set of boundary conditions. M_e indicates the number of terms (i.e. the computational cost) of the models that are equivalent to the fourth-order one. The last row shows the expansion terms needed to detect all the considered outputs. The latter combined models are used to build Table 4.5 which shows a comparison with the accuracies given by CPT, FSDT, and Kant-2 plate models. Table 4.6 summarizes the combined displacement fields which are needed to detect the exact solution for all the considered boundary conditions. The results which have been shown so far give us the reduced plate models which detect a 3D-like solution. Starting from these reduced models, it is possible to determine further theories which provide solutions with a certain degree of error compared to the full fourth-order one. Fig. 4.3 and Fig. 4.4 shows the number of terms which are needed to detect an output variable with a given error. The corresponding plate models are also indicated. For the linear models, the results are reported with and without the correction of the thickness locking. Models from the open literature have also been included. The accepted error range varies from 0 % to 10 %. The analyses undertaken suggest what follows.

1. The reduced plate models which are equivalent to a fourth-order theory vary significantly if different output variables are considered.
2. The influence of boundary conditions is not high.
3. Classical models are inadequate to deal with shear stresses.
4. A significant computational cost reduction is obtained only if a limited number of output variables has to be detected.
5. The number of terms vs. error diagram shows that all the theories derived from the present approach are able to satisfy a given error requirement with a lower computational cost than the open literature models considered. This shows the strength of the present technique for detecting the possible best theories for a given structural problem.

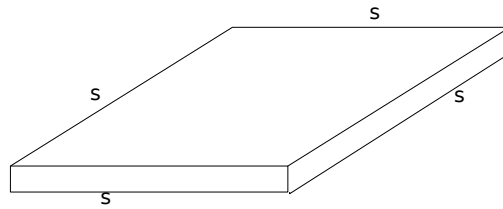
Loading Effects The effect of the loading conditions is herein investigated. A simply-supported plate is considered. Three different loading conditions are taken into account:

1. a bi-sinusoidal distributed load (Fig. 4.5 (a));
2. a point load (Fig. 4.5 (b));
3. four point loads (Fig. 4.5 (c)).

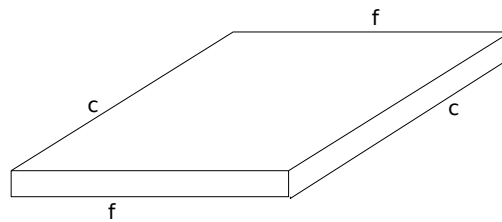
The point load which is applied at the top surface of the plate has an intensity of 10 N while the four point loads have an intensity of 2.5 N each. Table 4.7 reports the symbolic representation of each loading set. Table 4.8 shows the fourth-order FEM solution for the point load condition. Table 4.2 values are used for the distributed loading case. The sets of displacement variables which are needed to detect various outputs precisely are given in Table 4.9. Each row refers to a different output variable. Each column considers a different loading condition. M_e indicates the number of terms of the models that are equivalent to the fourth-order one. The last row shows the plate models which are needed to detect all the considered outputs precisely. The latter combined models are used to build Table 4.10 which shows a comparison of the accuracies given by CPT, FSDT, and Kant-2 plate models. Table 4.11 summarizes the combined displacement fields which are able to detect the exact solution for all the considered loading conditions. Fig. 4.6 shows the number of terms which are needed to compute an output variable with a given error. The corresponding plate models are also indicated together with models retrieved from open literature. For the linear models, the results are reported with and without the thickness locking correction. The accepted error range varies from 0 % to 10 %. No differences between the one point load case and the four point load one have been observed, therefore the graphs related to the four point load are not reported. The following remarks arise from the analyses carried out.

1. The sets of effective displacement variables vary if distributed or concentrated loads are considered, whereas there are no differences if one or multiple point loads are used.
2. The effect of the considered output variable is significant in the case of distributed load, it is almost negligible if point loads are considered.
3. The validity of the number of terms vs. error diagram for providing guidelines for the construction of plate theories accomplishing a given accuracy is confirmed. As the error is fixed, the theories derived generally lie beneath classical and other refined models, that is, the proposed models are able to fulfil a certain accuracy demand with a lower computational cost.

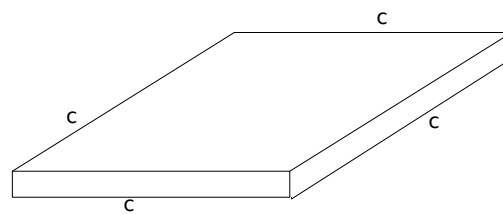
Boundary Condition, and Thickness Effects The combined effect of loading and boundary conditions is considered. The influence of the length-to-thickness ratio, a/h , is also investigated. The loading sets considered are the same as those seen in the previous analyses. Each output variable is associated to a symbol as shown in Table 4.12. A thin plate is first considered by assuming a/h equals 100. Table 4.13 shows the sets of displacement variables which are needed to detect various output variables previously. Each row refers to a different loading condition, each column to different boundary conditions. Table 4.14 reports the plate models that precisely detect all the considered outputs for all the considered boundary and loading conditions. Tables 4.15 to 4.18 report the same type of results for a/h equal to 10 and 5, respectively. The obtained plate models are summarized in



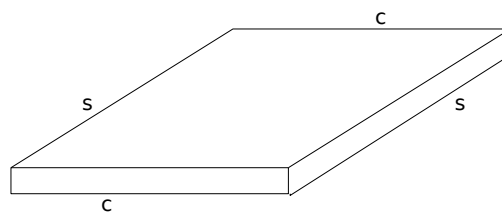
(a) Simply-supported.



(b) Two clamped and two free edges.



(c) Four clamped edges.



(d) Two simply-supported and two clamped edges.

Figure 4.2 Adopted boundary conditions.

Table 4.3 Influence of each displacement variable of a fourth order model on the solution. Simply-supported plate with a distributed load, $a/h= 10$.

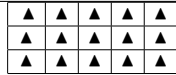
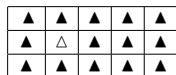
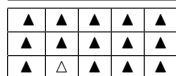
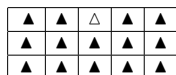
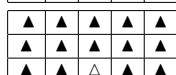
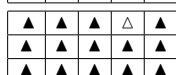
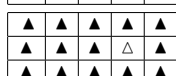
	δ_{u_z} [%]	$\delta_{\sigma_{xx}}$ [%]	$\delta_{\sigma_{xz}}$ [%]	$\delta_{\sigma_{zz}}$ [%]
	100.0	100.0	100.0	100.0
	100.0	100.5	100.0	100.1
	100.0	99.9	100.0	100.1
	0.13	1.18	1.27	75.59
	19.5	14.7	269.3	93.9
	19.5	18.8	16.11	93.90
	100.0	101.4	100.0	136.3
	100.0	100.0	100.0	100.1
	100.0	100.0	100.0	100.1
	95.4	76.6	101.6	-598.1
	99.7	99.7	72.2	100.0
	99.7	99.7	99.9	100.0
	100.0	100.0	100.0	100.5
	100.0	100.0	100.0	100.0
	100.0	100.0	100.0	100.0
	100.0	100.7	100.0	125.7

Table 4.4 Comparison of the sets of effective terms for a plate with a distributed load with different boundary conditions, $a/h = 10$.

	<i>ssss</i>	<i>cfcf</i>	<i>cccc</i>	<i>scsc</i>
	$M_e = 6$	$M_e = 7$	$M_e = 7$	$M_e = 7$
u_z				
	$M_e = 10$	$M_e = 10$	$M_e = 10$	$M_e = 9$
σ_{xx}				
	$M_e = 10$	$M_e = 10$	$M_e = 10$	$M_e = 10$
σ_{yy}				
	$M_e = 6$	$M_e = 6$	$M_e = 7$	$M_e = 6$
σ_{xz}				
	$M_e = 6$	$M_e = 7$	$M_e = 7$	$M_e = 6$
σ_{yz}				
	$M_e = 11$	$M_e = 12$	$M_e = 13$	$M_e = 12$
σ_{zz}				
	$M_e = 13$	$M_e = 13$	$M_e = 13$	$M_e = 13$
<i>COMBINED</i>				

Table 4.5 Accuracy of different models for a plate with a distributed load, $a/h=10$.

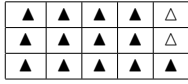
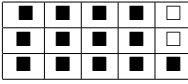
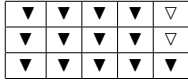
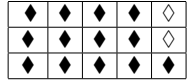
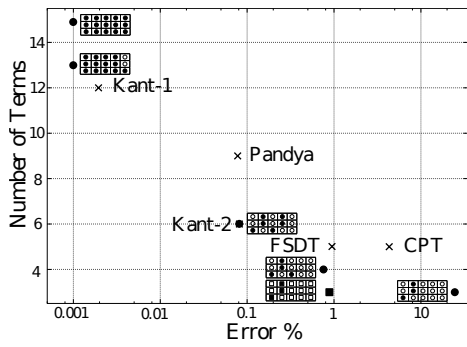
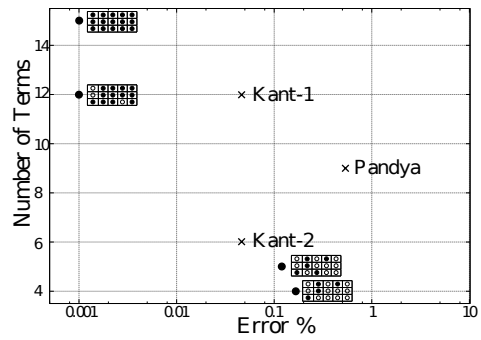
	δ_{u_z} [%]	$\delta_{\sigma_{xx}}$ [%]	$\delta_{\sigma_{yy}}$ [%]	$\delta_{\sigma_{xz}}$ [%]	$\delta_{\sigma_{yz}}$ [%]	$\delta_{\sigma_{zz}}$ [%]
SSSS						
	100.0	100.0	100.0	100.0	100.0	100.0
CPT	96.1	98.4	98.4	66.8	66.8	1974.2
FSDT	100.9	98.4	98.4	66.8	66.8	1974.2
Kant-2	99.9	100.2	100.2	100.0	100.0	79.4
cfcf						
	100.0	100.0	100.0	100.0	100.0	100.0
CPT	91.2	98.3	94.9	239.5	-67.86	1171.3
FSDT	103.1	98.7	97.2	83.2	65.4	1183.7
Kant-2	99.9	100.0	101.0	98.8	99.7	80.4
cccc						
	100.0	100.0	100.0	100.0	100.0	100.0
CPT	88.4	96.2	96.2	87.5	87.5	1074.0
FSDT	102.8	97.1	97.1	81.4	81.4	1084.8
Kant-2	99.8	99.9	99.9	98.9	98.9	80.0
spsc						
	100.0	100.0	100.0	100.0	100.0	100.0
CPT	90.2	94.6	97.7	66.1	84.7	1281.1
FSDT	102.4	98.3	97.9	67.3	81.8	1304.3
Kant-2	99.8	100.6	100.0	100.0	98.9	79.8

Table 4.6 Sets of effective terms for all the considered boundary conditions.

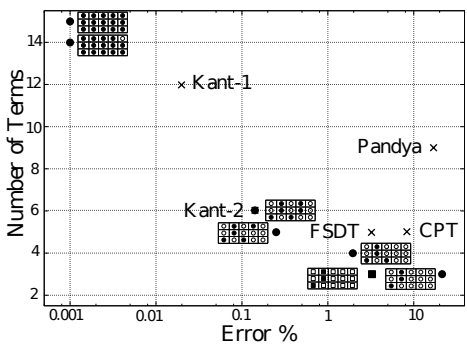
▲■▼◆	▲■▼◆	▲■▼◆	▲■▼◆	△□▽◇
▲■▼◆	▲■▼◆	▲■▼◆	▲■▼◆	△□▽◇
▲■▼◆	▲■▼◆	▲■▼◆	▲■▼◆	▲■▼◆



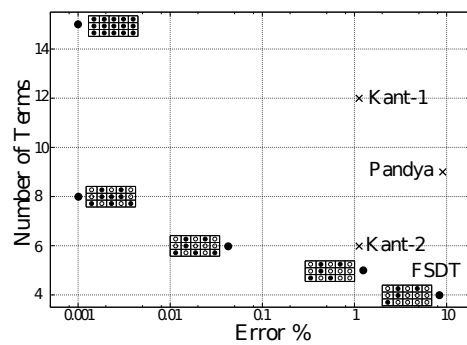
(a) Simply-supported plate. Output u_z .



(b) Simply-supported plate. Output σ_{xz} .

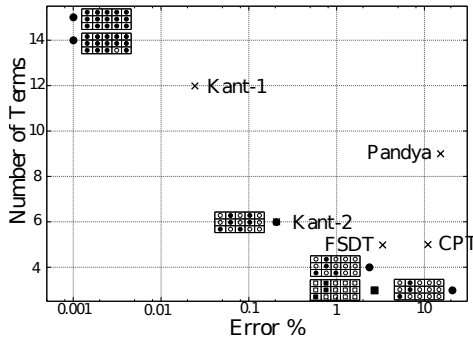


(c) Two clamped e two free edges plate. Output u_z .

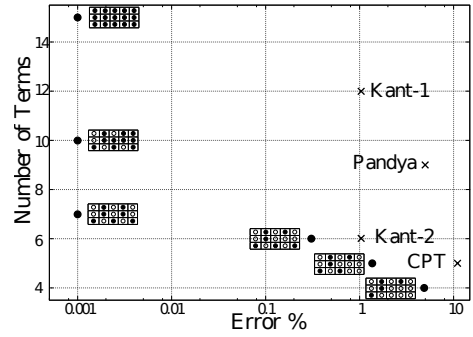


(d) Two clamped e two free edges plate. Output σ_{xz} .

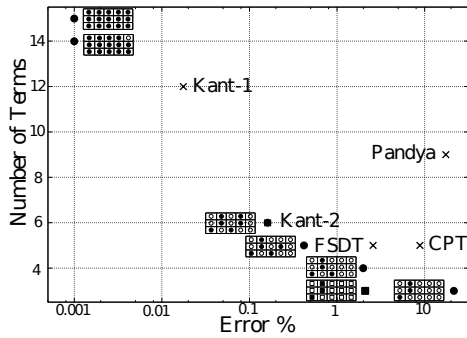
Figure 4.3 Number of terms vs. error for different output variables by various models for a simply-supported plate and two edges free and two edges clamped plate with a distributed load, $a/h = 10$. ■ model with the thickness locking corrected.



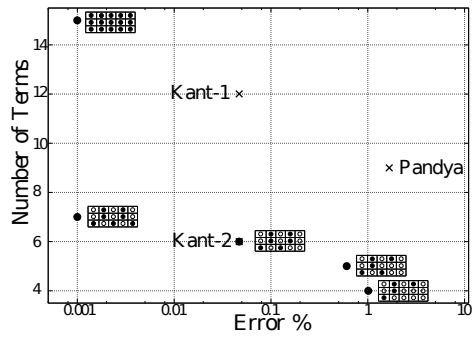
(a) Clamped Plate. Output u_z .



(b) Clamped Plate. Output σ_{xz} .



(c) Two simply-supported and two clamped edges plate. Output u_z .



(d) Two simply-supported and two clamped edges plate. Output σ_{xz} .

Figure 4.4 Number of terms vs. error for different output variables by various models for a clamped plate and two simply-supported edges and two clamped edges plate with a distributed load, $a/h = 10$. ■ model with the thickness locking corrected.

Table 4.7 Symbols that indicate the status of a displacement variable for different loading conditions.

Active term	Inactive term		
▲	△	Distributed Load	
■	□	Point Load	
▼	▽	Four Point Loads	

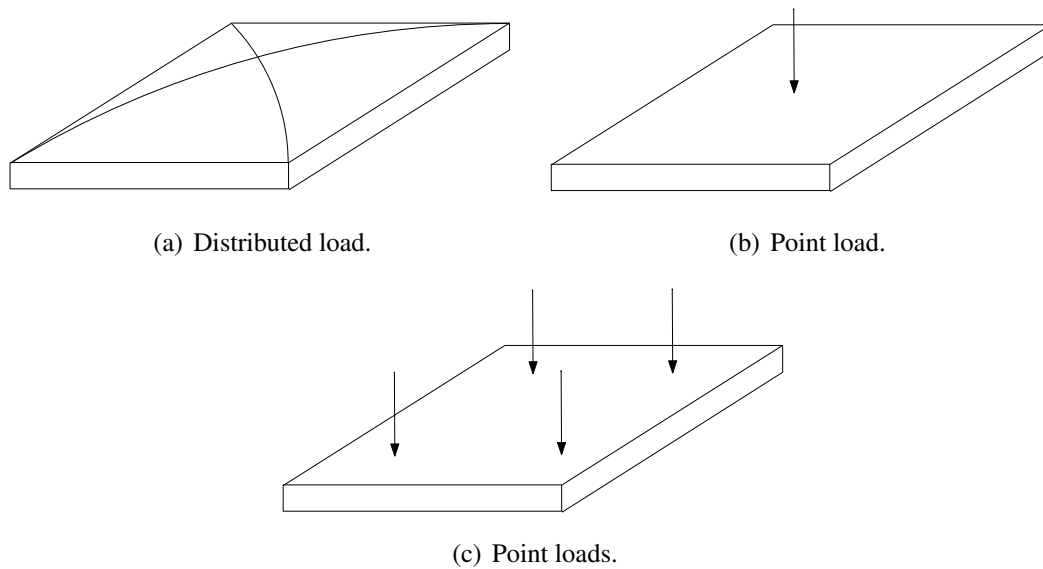


Figure 4.5 Adopted loading conditions.

Table 4.8 Fourth order FEM model solutions in the case of simply-supported plate subject to point loading conditions, $a/h = 10$.

	$u_{zN=4}$ [m]	$\sigma_{xxN=4}$ [Pa]	$\sigma_{yzN=4}$ [Pa]	$\sigma_{zzN=4}$ [Pa]
Point Load	1.7662×10^{-7}	1.9336×10^5	7.0444×10^3	3.1373×10^4
Four Point Loads	1.7662×10^{-7}	1.9336×10^5	6.2392×10^3	3.1373×10^4

Table 4.9 Comparison of the sets of effective terms for a simply-supported plate subject to different loading conditions.

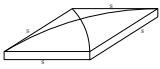
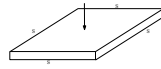
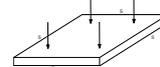
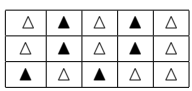
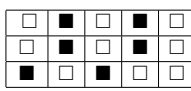
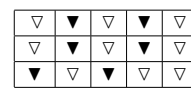
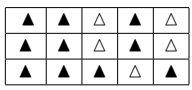
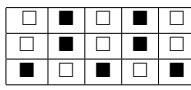
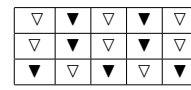
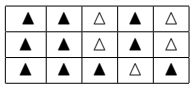
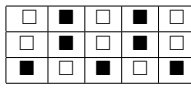
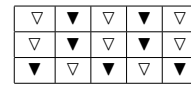
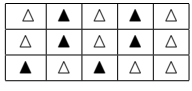
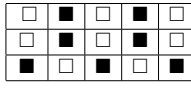
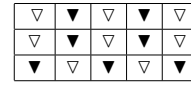
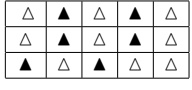
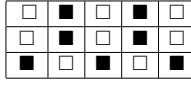
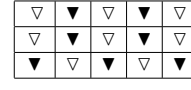
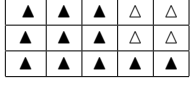
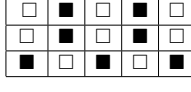
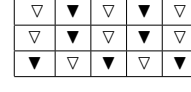
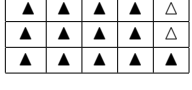
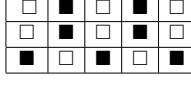
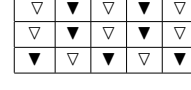
			
	$M_e = 6$	$M_e = 6$	$M_e = 6$
u_z			
	$M_e = 10$	$M_e = 7$	$M_e = 7$
σ_{xx}			
	$M_e = 10$	$M_e = 7$	$M_e = 7$
σ_{yy}			
	$M_e = 6$	$M_e = 7$	$M_e = 7$
σ_{xz}			
	$M_e = 6$	$M_e = 7$	$M_e = 7$
σ_{yz}			
	$M_e = 11$	$M_e = 7$	$M_e = 7$
σ_{zz}			
	$M_e = 13$	$M_e = 7$	$M_e = 7$
<i>COMBINED</i>			

Table 4.10 Accuracy of different plate models for a simply-supported plate subject to various loading conditions, $a/h=10$.

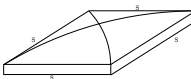
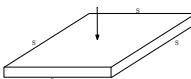
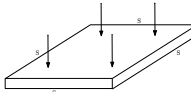
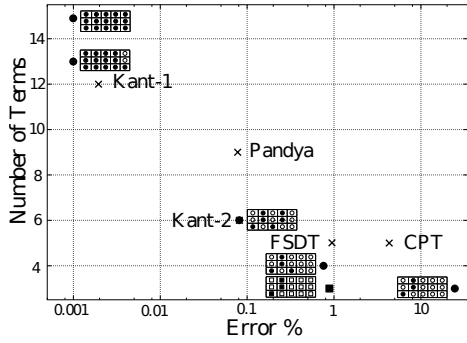
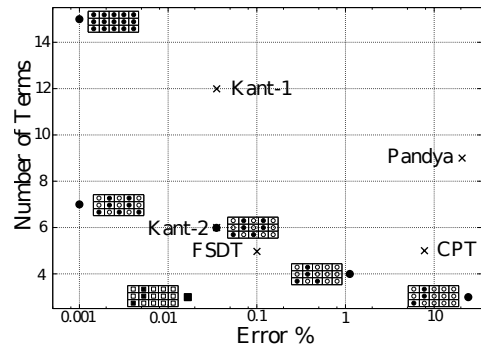
	δ_{u_z} [%]	$\delta_{\sigma_{xx}}$ [%]	$\delta_{\sigma_{yy}}$ [%]	$\delta_{\sigma_{xz}}$ [%]	$\delta_{\sigma_{xz}}$ [%]	$\delta_{\sigma_{zz}}$ [%]															
																					
<table border="1" style="display: inline-table; vertical-align: middle;"> <tr><td>▲</td><td>▲</td><td>▲</td><td>▲</td><td>△</td></tr> <tr><td>▲</td><td>▲</td><td>▲</td><td>▲</td><td>△</td></tr> <tr><td>▲</td><td>▲</td><td>▲</td><td>▲</td><td>▲</td></tr> </table>	▲	▲	▲	▲	△	▲	▲	▲	▲	△	▲	▲	▲	▲	▲	100.0	100.0	100.0	100.0	100.0	100.0
▲	▲	▲	▲	△																	
▲	▲	▲	▲	△																	
▲	▲	▲	▲	▲																	
CPT	96.1	98.4	98.4	66.8	66.8	1974.2															
FSDT	100.9	98.4	98.4	66.8	66.8	1974.2															
Kant-2	99.9	100.3	100.3	100.0	100.0	79.4															
																					
<table border="1" style="display: inline-table; vertical-align: middle;"> <tr><td>□</td><td>■</td><td>□</td><td>■</td><td>□</td></tr> <tr><td>□</td><td>■</td><td>□</td><td>■</td><td>□</td></tr> <tr><td>■</td><td>□</td><td>■</td><td>□</td><td>■</td></tr> </table>	□	■	□	■	□	□	■	□	■	□	■	□	■	□	■	100.0	100.0	100.0	100.0	100.0	100.0
□	■	□	■	□																	
□	■	□	■	□																	
■	□	■	□	■																	
CPT	91.4	83.7	83.7	67.0	67.0	540.1															
FSDT	99.9	83.7	83.7	67.0	67.0	540.1															
Kant-2	100.0	96.5	96.5	99.9	99.9	39.5															
																					
<table border="1" style="display: inline-table; vertical-align: middle;"> <tr><td>▽</td><td>▼</td><td>▽</td><td>▼</td><td>▽</td></tr> <tr><td>▽</td><td>▼</td><td>▽</td><td>▼</td><td>▽</td></tr> <tr><td>▼</td><td>▽</td><td>▼</td><td>▽</td><td>▼</td></tr> </table>	▽	▼	▽	▼	▽	▽	▼	▽	▼	▽	▼	▽	▼	▽	▼	100.0	100.0	100.0	100.0	100.0	100.0
▽	▼	▽	▼	▽																	
▽	▼	▽	▼	▽																	
▼	▽	▼	▽	▼																	
CPT	91.4	83.7	83.7	67.0	67.0	540.1															
FSDT	99.9	83.7	83.7	67.0	67.0	540.1															
Kant-2	100.0	96.5	96.5	99.9	99.9	39.5															

Table 4.11 Sets of effective terms for the considered loading conditions.

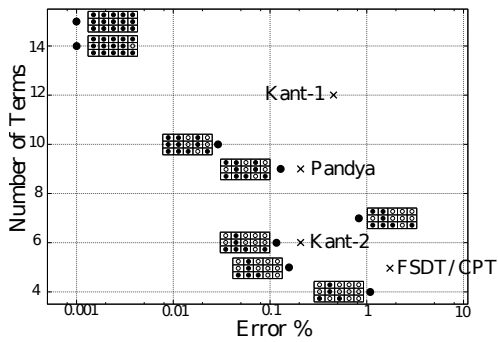
▲ □ ▽	▲ ■ ▽	▲ □ ▽	▲ ■ ▽	△ □ ▽
▲ □ ▽	▲ ■ ▽	▲ □ ▽	▲ ■ ▽	△ □ ▽
▲ ■ ▽	▲ □ ▽	▲ ■ ▽	▲ □ ▽	▲ ■ ▽



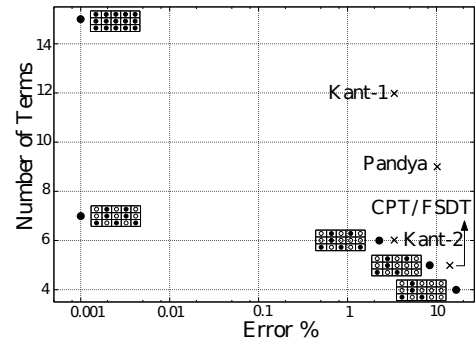
(a) Distributed load. Output u_z .



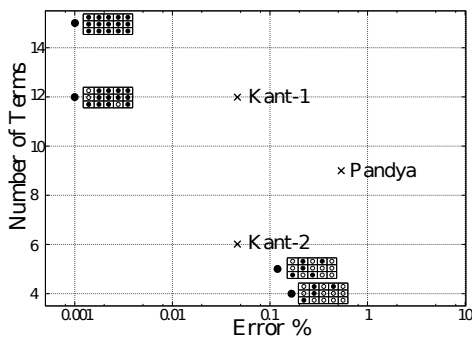
(b) Point load. Output u_z .



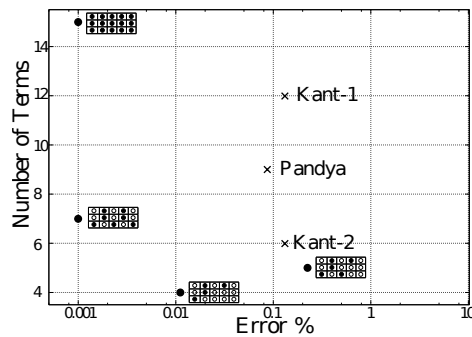
(c) Distributed load. Output σ_{xx} .



(d) Point load. Output σ_{xx} .



(e) Distributed load. Output σ_{xz} .



(f) Point load. Output σ_{xz} .

Figure 4.6 Number of terms vs. error for different output variables and loading conditions by various models for a simply-supported plate, $a/h = 10$. ■ model with the thickness locking corrected.

Table 4.12 Symbols that indicate the status of a displacement variable for different output variables.

Active term	Inactive term	
▲	△	u_z
■	□	σ_{xx}
▼	▽	σ_{xz}
◆	◇	σ_{zz}

Table 4.13 Comparison of the sets of effective terms for plates with different boundary and loading conditions, $a/h = 100$. ▲ = u_z , ■ = σ_{xx} , ▼ = σ_{xz} and ◆ = σ_{zz}

<i>SSSS</i>			
<i>cfcf</i>			
<i>cccc</i>			
<i>SCSC</i>			

Table 4.16 Sets of effective terms for all the considered boundary and loading conditions, $a/h = 10$.

$\triangle \blacksquare \nabla \blacklozenge$	$\blacktriangle \blacksquare \nabla \blacklozenge$	$\triangle \square \nabla \blacklozenge$	$\blacktriangle \blacksquare \nabla \blacklozenge$	$\triangle \square \nabla \diamond$
$\triangle \blacksquare \nabla \blacklozenge$	$\blacktriangle \blacksquare \nabla \blacklozenge$	$\triangle \square \nabla \blacklozenge$	$\blacktriangle \blacksquare \nabla \blacklozenge$	$\triangle \square \nabla \diamond$
$\blacktriangle \blacksquare \nabla \blacklozenge$	$\blacktriangle \blacksquare \nabla \blacklozenge$	$\blacktriangle \blacksquare \nabla \blacklozenge$	$\triangle \square \nabla \blacklozenge$	$\blacktriangle \blacksquare \nabla \blacklozenge$

Table 4.19 where all the considered a/h cases are shown. Table 4.20 presents a comparison of the accuracies given by the plate models obtained and the classical theories. A plate with two clamped and two free edges is considered. For the sake of brevity, the accuracy data which are related to the other boundary conditions are not reported here. The analyses carried out suggest the following comments.

1. The sets of effective displacement variables depend on all the three considered parameters: loadings, boundary conditions, and thickness.
2. The proper analysis of thick plates require more sophisticated models since the total number of expansion terms increases as a/h decreases. This result is analogous to that in Carrera and Petrolo (61).
3. It is confirmed that different output variables require different plate models to be properly detected.

First conclusion and outline Refined models have been hierarchically obtained by means of the Carrera Unified Formulation, CUF. The finite element analysis has been used to deal with arbitrary geometries, loadings, and boundary conditions. Isotropic plates have been considered. A fourth-order solution has been adopted as reference. The accuracy analysis has been conducted via a so-called mixed asymptotic/axiomatic approach which determines the role of each displacement variable in computing a given displacement/stress variable. The present approach has proved its validity in constructing:

1. reduced plate models equivalent to a full higher-order theory;
2. reduced plate models able to fulfil a given accuracy input.

As far as the first type of models is concerned, the following conclusions can be drawn.

- All the parameters considered (loadings, boundary conditions, and thickness) are important to determine the sets of effective terms, that is, as one of these parameters changes, a different plate model is required.
- The influence of the length-to-thickness ratio is particularly strong.
- The use of full models is mandatory when a complete set of results is needed, since only few can be discarded.

The construction of the second type of plate modes has highlighted that Unified Formulation allows us, for a given problem, to obtain a diagram that in terms of accuracy (input) gives an answer to the following fundamental questions (see Figs 4.3, 4.4 and 4.6):

- what is the 'minimum' number of the terms, N_{min} , to be used in a Finite Element Plate model?
- Which are the terms to be retained, that is, which are the generalized displacement variables to be used as FE dof's?

The present method of analysis is able to create plots like the one in Fig. 4.7 that gives the number of terms as function of the permitted error. This plot can be defined as Best finite element Plate Theory Diagram BPTD since it allows us to edit an arbitrary given theory in order to have a lower amount of terms for a given error (vertical shift, Δ_N) or, to increase the accuracy keeping the computational cost constant (horizontal shift, Δ_{error}). Most times, the plot presented appears as an hyperbole. CUF makes the computation of such a plot possible. Note that the diagram has the following properties:

- it changes by changing problems (a/h , loadings, boundary conditions, etc.);
- it changes by changing output variable (displacement/stress components, or a combination of these).

The validity of the BPTD is tested by computing the accuracy of all the plate models obtainable as a combination of the 15 terms of the fourth-order theory. The results are reported in Fig. 4.8 in the case of a simply-supported plate loaded by a distributed load, u_z is considered as output variable. The BPTD perfectly matches the lower boundaries of the region where all the models lie. This confirms that the BPTD represents the best theory (i.e. the least cumbersome) for a given error. The BPTD permits the evaluation of any existing plate FE elements, as in the previous sections. The distance from the BPTD of a given known FE model represents a guideline to recommend any other plate theory.

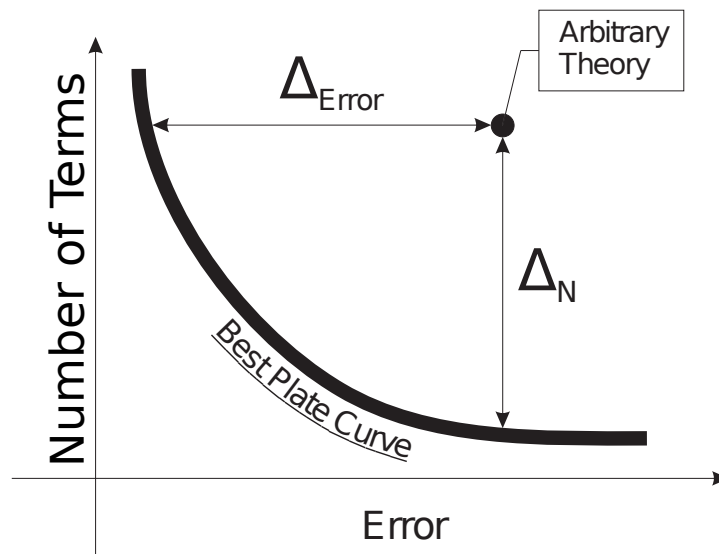


Figure 4.7 An example of Best Plate Theory Diagram (BPTD).

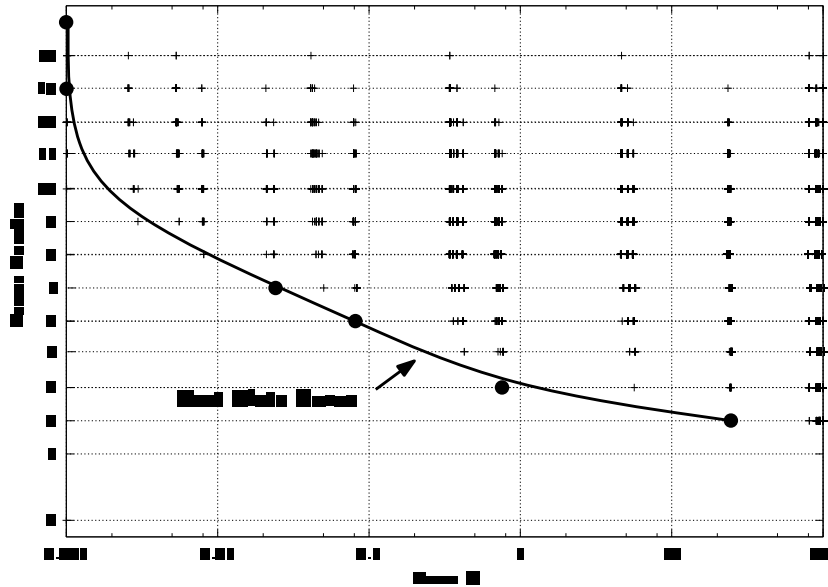


Figure 4.8 Accuracy of all the possible combinations of plate models in computing u_z for the simply-supported plate loaded by a distributed load (each '+' indicates a different plate model).

4.1.2 Orthotropic Plate

The geometry of plate is shown in Fig. 4.9, where a is 0.1 [m], and b is equal to a . A simply-supported orthotropic plate loaded with a distributed load is considered. A bi-sinusoidal transverse distributed load P_z is applied at the top surface:

$$P_z = p_z \sin\left(\frac{mx}{a}\right) \cos\left(\frac{ny}{b}\right) \quad (4.2)$$

where load amplitude p_z is equal to 1 [kPa]; m and n are the wave numbers in the two in-plane plate directions, both of them equal to 1. $u_z, \sigma_{xx}, \sigma_{yy}$ and σ_{zz} are computed at $[a/2, b/2, 0]$, while σ_{xz} is computed at $[0, b/2, h/2]$ and σ_{yz} is computed at $[a/2, 0, h/2]$. Stresses are computed directly from the constitutive equations. Four-node plate elements have been used, and a uniform mesh of 15 x 15 elements has been adopted. Shear locking problems have been solved by using mixed interpolation of tensorial components (previous extended to CUF in (72)). A fourth-order Layer Wise model has been adopted as the reference for the following analysis.

Table 4.21 shows the comparison of the analytical solution, obtained from the work of Carrera and Petrolo, (61) and the present FEM one. The solutions obtained via FEM model are very closed to the solution obtained via 3D models or close form. Moreover the finite elements solutions converge to the 3D solutions with increasing the numbers of elements. Comparison between some available results from literature and the present FE formulation is considered in Table 4.22. The solutions obtained by considered plate theories underline that the different considered theories are able to compute the various required output with a different accuracy. For example the CLT theory is able to detect almost exactly the normal stress σ_{xx} while it is not able to detect correctly the transversal displacement u_z and the shear stress σ_{yz} . Further comparison between the reference model and the equivalent single layer fourth-order plate model is given in Fig. 4.10. In this figure, various variable are plotted across the thickness direction. The figure

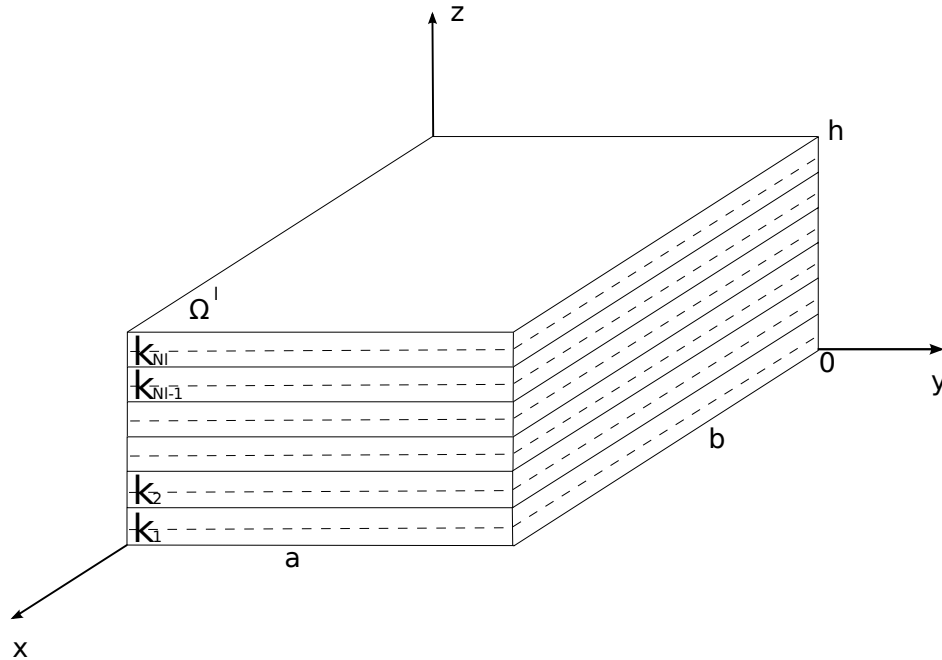


Figure 4.9 Plate geometry.

plots various variables along the thickness for the different outputs. These results constitute an assessment of the present FE plate model as detailed in the analysis below.

Length-to-thickness ratio effects The role of each displacement variable for different length-to-thickness ratio plates is conducted as a first assessment. Three different length-to-thickness ratio (a/h) sets are considered:

1. very thick plates ($a/h = 2.5$);
2. thick plates ($a/h = 5$);
3. thin plates ($a/h = 50$).

The effectiveness of each term is investigated for each length-to-thickness ratio. An unsymmetrical cross-ply (0/90) square plate is considered. E_L is equal to 40 GPa. E_T and E_z are equal to 1 GPa. ν_{LT} and ν_{Lz} are equal to 0.5 and 0.6 respectively. Fig. 4.11 illustrates the influence of each variable with respect to reference solution for the three considered plates. The x-axis represents the terms which are discarded and the related marker represents the error of the consequent reduced model compared to the reference model. The reference error, that is, the error determined through Eq. (2.40), is reported for all outputs and it is represented by the continuous line. From Fig. 4.11 it is possible to obtain different reduced models, one from each output, discarding all those terms for which the error marker is under the continuous line. For example from Fig. 4.11

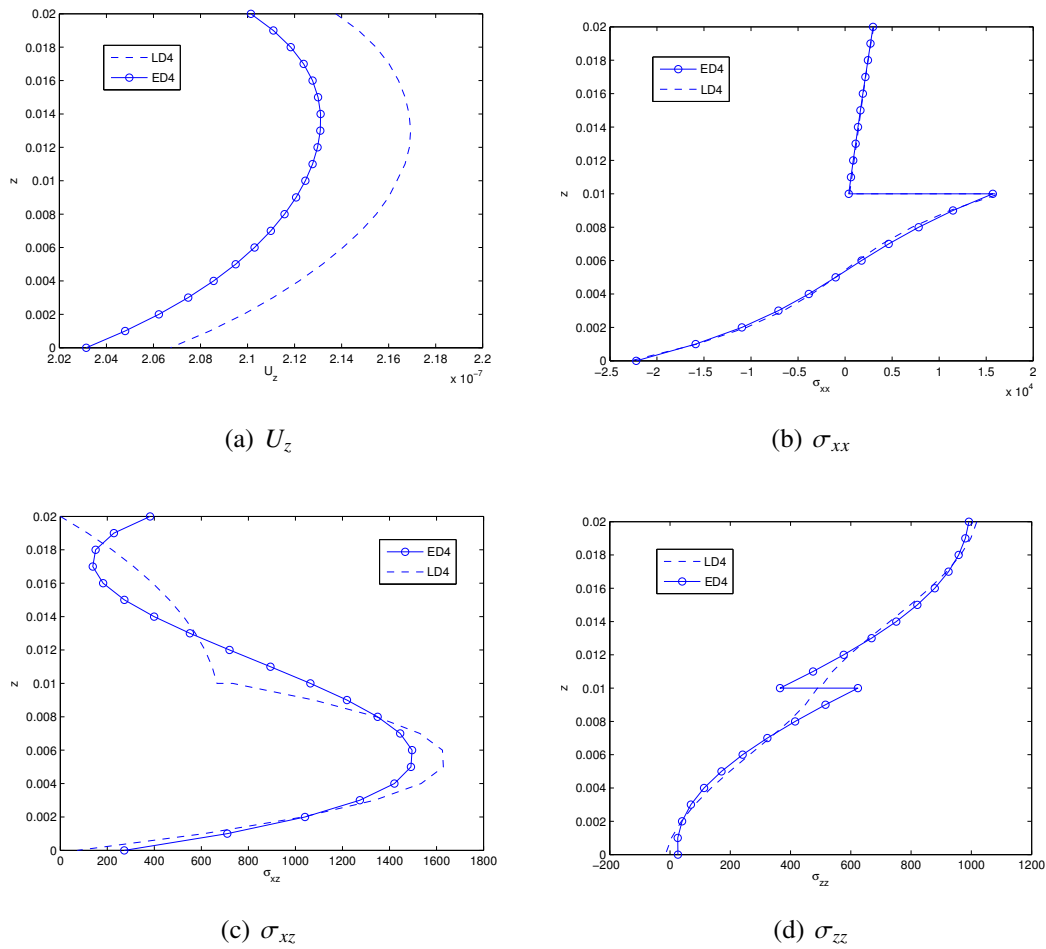


Figure 4.10 Comparison of the solutions obtained via Equivalent Single Layer fourth-order FEM model (ED4) and a Layer Wise fourth-order FEM model (LD4) in the case of an unsymmetrical (0/90) cross ply square simply-supported plate under distributed load.

it is possible to obtain for the output σ_{xz} and $a/h = 2.5$ the following displacement model

$$\begin{aligned} u_x &= u_{x1} + z u_{x2} + z^2 u_{x3} + z^3 u_{x4} + z^4 u_{x5} \\ u_z &= u_{z1} \end{aligned} \quad (4.3)$$

where only the terms having the error marker above the continuous line are considered. Table 4.23 has been obtained exploiting Fig. 4.11. It shows the reduced models obtained for the thin plate, the moderately thick plate and for the thick plate. For each reduced displacement model the error is reported and, for a comparison with the models present in literature, the errors given by the FSDT model and the Kant-2 (70) model are reported always with respect to the Layer Wise reference model. By varying the accepted error, that is, by varying the height of the continuous line, it is possible to determine further theories which provide solutions with a certain degree of error compared to the reference one. The procedure used to obtain the reduced models can be graphically described (see Fig. 4.12); positioning the continuous line on the lowest error marker and moving it upwards with discrete steps it is possible to

determine different reduced models neglecting all the terms which are under the continuous line. Fig. 4.13 has been built through this procedure. It shows the number of terms which are needed to detect an output variable with a given error. The corresponding plate models are also indicated. Models from open literature have also been included. In the figure the evolutions of the considered outputs along the thickness, compared with the reference model, are also reported for the reduced model which shows the lowest error in order to give a more realistic idea of the reduced model behaviour. It is possible to observe that in some cases the evolution along the thickness of the output obtained through the reduced model is very different from the output obtained through the reference model. The analysis undertaken suggests the following discussion:

1. The reduced plate models which are equivalent to a fourth-order theory vary significantly if different output variables are considered.
2. The influence of length-to-thickness ratio is significant.
3. In some cases the reduced models present errors smaller than those of the full model.

Orthotropic ratio effects The effect of the orthotropic ratio is herein investigated. An unsymmetrical cross ply (0/90) square plate is considered. E_T and E_z are equal to 1 GPa. ν_{LT} and ν_{Lz} are equal to 0.5 and 0.6 respectively. Each layer is 0.01 m thick. Three different orthotropic ratios are considered ($E_L/E_T = 5$, $E_L/E_T = 40$, $E_L/E_T = 100$). The effectiveness of each term is investigated for each orthotropic ratio. Fig. 4.14 illustrate the influence of each term on, the normal stress σ_{xx} and the shear stress σ_{xz} . Table 4.24 has been obtained through the same procedure describe in the previous paragraph from Fig. 4.14. It reports the reduced models obtained for all the considered outputs. In Table 4.24 the errors relative to the reduced model and the errors relative to models from the open literature are also reported. Varying the accepted error is possible to develop further theories which provide solutions with a certain degree of error when compared to the reference one. Figure 4.15 illustrate the number of terms needed to compute an output variable with a given error. The corresponding plate models are also indicated together with models retrieved from open literature. The analyses carried out suggest the following comments :

1. The influence of each term varies significantly according to the considered output.
2. The influence of each term depends weakly on the orthotropic ratio.

Table 4.19 Influence of a/h on the displacement field terms for combined boundary and loading conditions.

$a/h = 100$	$\triangle \square \nabla \diamond$	$\blacktriangle \blacktriangledown \blacklozenge$	$\triangle \square \nabla \diamond$	$\blacktriangle \blacktriangledown \blacklozenge$	$\triangle \square \nabla \diamond$
	$\triangle \square \nabla \diamond$	$\blacktriangle \blacktriangledown \blacklozenge$	$\triangle \square \nabla \diamond$	$\blacktriangle \blacktriangledown \blacklozenge$	$\triangle \square \nabla \diamond$
	$\blacktriangle \blacktriangledown \blacklozenge$	$\triangle \square \nabla \diamond$	$\blacktriangle \blacktriangledown \blacklozenge$	$\triangle \square \nabla \diamond$	$\triangle \square \nabla \diamond$
$a/h = 10$	$\triangle \blacktriangle \blacktriangledown \blacklozenge$	$\blacktriangle \blacktriangledown \blacklozenge$	$\triangle \square \nabla \diamond$	$\blacktriangle \blacktriangledown \blacklozenge$	$\triangle \square \nabla \diamond$
	$\triangle \blacktriangle \blacktriangledown \blacklozenge$	$\blacktriangle \blacktriangledown \blacklozenge$	$\triangle \square \nabla \diamond$	$\blacktriangle \blacktriangledown \blacklozenge$	$\triangle \square \nabla \diamond$
	$\blacktriangle \blacktriangledown \blacklozenge$	$\blacktriangle \blacktriangledown \blacklozenge$	$\blacktriangle \blacktriangledown \blacklozenge$	$\triangle \square \nabla \diamond$	$\blacktriangle \blacktriangledown \blacklozenge$
$a/h = 5$	$\blacktriangle \blacktriangledown \blacklozenge$	$\blacktriangle \blacktriangledown \blacklozenge$	$\triangle \square \nabla \diamond$	$\blacktriangle \blacktriangledown \blacklozenge$	$\triangle \square \nabla \diamond$
	$\blacktriangle \blacktriangledown \blacklozenge$	$\blacktriangle \blacktriangledown \blacklozenge$	$\triangle \square \nabla \diamond$	$\blacktriangle \blacktriangledown \blacklozenge$	$\triangle \square \nabla \diamond$
	$\blacktriangle \blacktriangledown \blacklozenge$	$\blacktriangle \blacktriangledown \blacklozenge$	$\blacktriangle \blacktriangledown \blacklozenge$	$\triangle \square \nabla \diamond$	$\blacktriangle \blacktriangledown \blacklozenge$

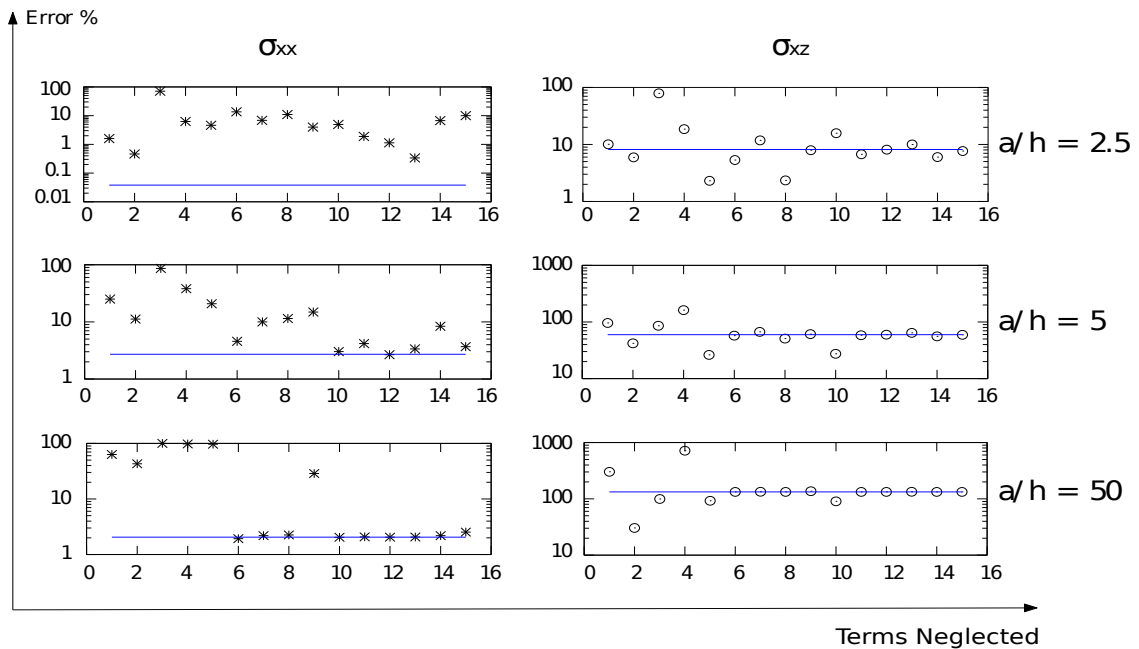


Figure 4.11 Influence of each displacement variable with respect to the reference ratio $ED4/LD4$ for different length-to-thickness ratios.

Table 4.20 Accuracy of different displacement models in the case of a plate with two clamped and two free edges subject to a point load.

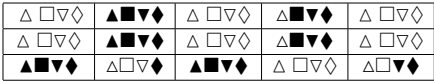
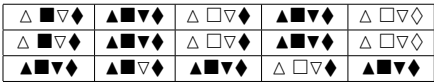
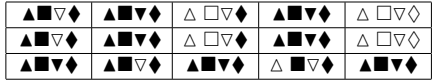
	δ_{u_z} [%]	$\delta_{\sigma_{xx}}$ [%]	$\delta_{\sigma_{yy}}$ [%]	$\delta_{\sigma_{xz}}$ [%]	$\delta_{\sigma_{yz}}$ [%]	$\delta_{\sigma_{zz}}$ [%]
<i>a/h = 100</i>						
	100.0	100.0	100.0	100.0	100.0	100.0
CPT	102.7	98.5	98.0	158.6	710.2	1337.4
FSDT	102.9	98.5	98.0	80.0	114.3	1337.6
Kant-2	100.0	100.0	100.0	99.9	117.9	99.0
<i>a/h = 10</i>						
	100.0	100.0	100.0	100.0	100.0	100.0
CPT	86.2	82.5	79.2	202.9	-106.014	449.824
FSDT	101.6	82.7	80.24	83.6	72.7	453.2
Kant-2	100.0	96.2	95.7	98.7	97.7	39.8
<i>a/h = 5</i>						
	100.0	100.0	100.0	100.0	100.0	100.0
CPT	60.7	70.6	65.7	228.9	-90.6	189.9
FSDT	102.8	70.9	68.1	88.7	71.6	193.5
Kant-2	100.4	89.7	88.7	96.0	99.1	-23.1

Table 4.21 Comparison of the solutions obtained via 3D models, closed form and a Layer Wise fourth order FEM model in the case of simply-supported orthotropic plate loaded with a Distributed Load. $\bar{u}_z = u_z \frac{100E_T h^3}{p_z a^4}$.
 $\bar{\sigma}_{xx} = \frac{\sigma_{xx}}{\bar{p}_z(a/h)}$ · $\bar{\sigma}_{xz} = \frac{\sigma_{xz}}{\bar{p}_z(a/h)^2}$ · $\bar{\sigma}_{zz} = \frac{\sigma_{zz}}{\bar{p}_z(a/h)}$

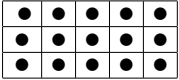
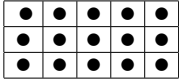
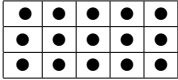
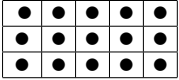
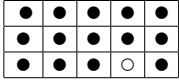
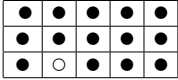
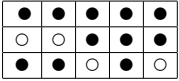
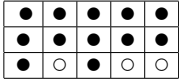
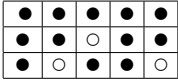
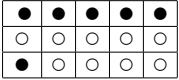
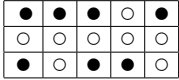
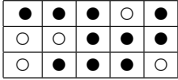
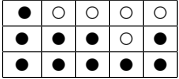
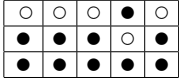
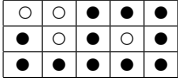
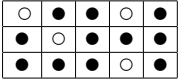
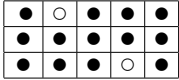
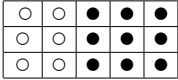
	\bar{u}_z	$\bar{\sigma}_{xx}$	$\bar{\sigma}_{yz}$
3D (61)	0.6970	0.5827	0.0472
Closed form (61)	0.6970	0.5827	0.0472
Present FEM			
<i>FEM(mesh15x15)</i>	0.6948	0.5831	0.0474
<i>FEM(mesh19x19)</i>	0.6956	0.5830	0.0473
<i>FEM(mesh23x23)</i>	0.6960	0.5829	0.0473
<i>FEM(mesh27x27)</i>	0.6963	0.5828	0.0473
<i>FEM(mesh31x31)</i>	0.6964	0.5828	0.0472

Table 4.22 Comparison of the solutions obtained via different plate theories for a simply-supported unsymmetric cross-ply (0°/90°) square plate under bi-sinusoidal distributed load. $\bar{u}_z = u_z \frac{100E_T h^3}{p_z a^4}$ · $\bar{\sigma}_{xx} = \frac{\sigma_{xx}}{\bar{p}_z(a/h)}$ · $\bar{\sigma}_{xz} = \frac{\sigma_{xz}}{\bar{p}_z(a/h)^2}$ · $\bar{\sigma}_{zz} = \frac{\sigma_{zz}}{\bar{p}_z(a/h)}$

	\bar{u}_z	$\bar{\sigma}_{xx}$	$\bar{\sigma}_{yz}$
<i>Present ED4</i>	1.5297	0.1132	0.1958
<i>Present LD4*</i>	1.5548	0.1163	0.1158
<i>Present CLT</i>	0.7586	0.1026	0.0167
<i>Present FS DT</i>	1.5168	0.1221	0.1992
<i>HOT – 1 by Kant (69)</i>	1.4625	0.1141	0.1965
<i>HOT – 2 by Kant (70)</i>	0.8713	0.0469	0.2275
<i>HOT – 3 by Pandya (68)</i>	1.4959	0.1016	0.2044

(* Reference solution.)

Table 4.23 Comparison of the sets of effective terms for an isotropic simply-supported plate loaded with a distributed load, $\theta = 0/90$, for different length-to-thickness ratio

	$a/h = 2.5$		$a/h = 5$		$a/h = 50$	
	<i>Theory</i>	$\delta \%$	<i>Theory</i>	$\delta \%$	<i>Theory</i>	$\delta \%$
u_z		99.9		98.3		99.0
	<i>FSDT</i>	72.7	<i>FSDT</i>	76.9	<i>FSDT</i>	84.9
	<i>Kant - 2</i>	70.7	<i>Kant - 2</i>	57.4	<i>Kant - 2</i>	34.6
σ_{xx}		100.0		97.3		98.1
	<i>FSDT</i>	47.4	<i>FSDT</i>	86.8	<i>FSDT</i>	146.3
	<i>Kant - 2</i>	50.0	<i>Kant - 2</i>	40.1	<i>Kant - 2</i>	29.6
σ_{yy}		100.4		97.0		100.3
	<i>FSDT</i>	65.5	<i>FSDT</i>	85.7	<i>FSDT</i>	91.1
	<i>Kant - 2</i>	92.6	<i>Kant - 2</i>	82.7	<i>Kant - 2</i>	65.4
σ_{xz}		76.7		67.8		0.2
	<i>FSDT</i>	77.4	<i>FSDT</i>	119.7	<i>FSDT</i>	185.0
	<i>Kant - 2</i>	98.0	<i>Kant - 2</i>	169.5	<i>Kant - 2</i>	277.4
σ_{yz}		78.0		98.0		256.1
	<i>FSDT</i>	103.1	<i>FSDT</i>	134.2	<i>FSDT</i>	185.4
	<i>Kant - 2</i>	130.7	<i>Kant - 2</i>	190.1	<i>Kant - 2</i>	277.9
σ_{zz}		100.1		93.9		64.3
	<i>FSDT</i>	45.0	<i>FSDT</i>	180.5	<i>FSDT</i>	1.0 10 ⁴
	<i>Kant - 2</i>	74.1	<i>Kant - 2</i>	86.0	<i>Kant - 2</i>	68.6

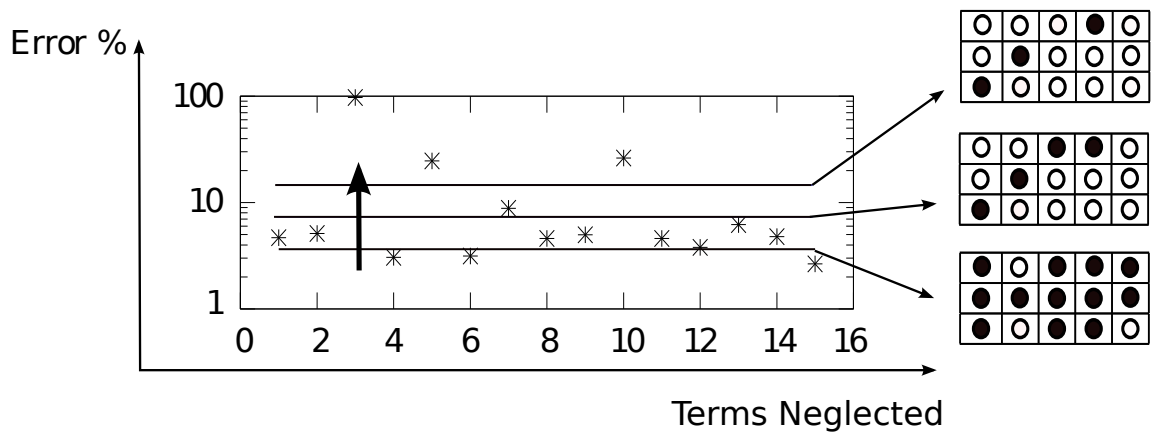


Figure 4.12 Example of different displacement fields obtained varying the accepted error.

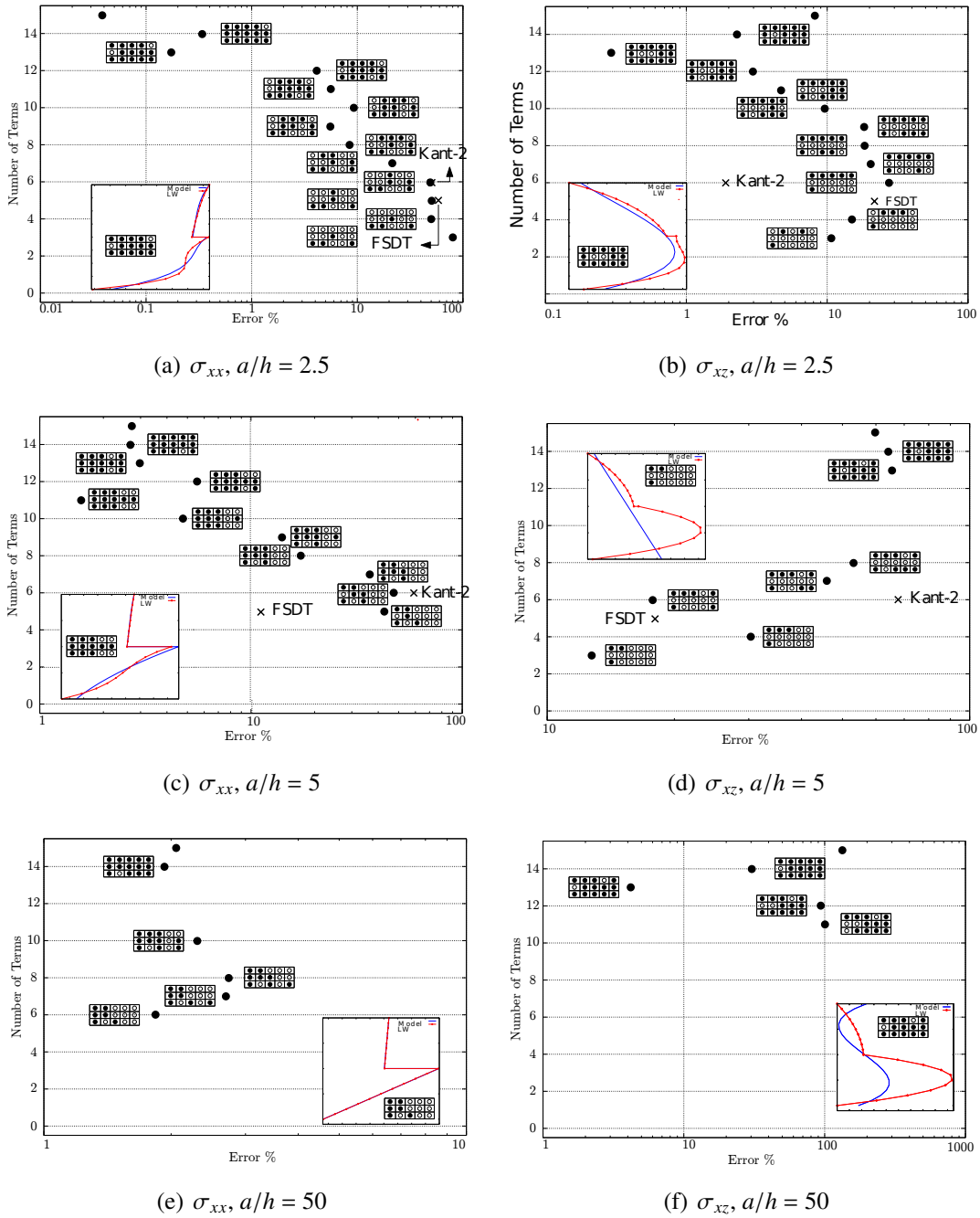


Figure 4.13 Number of terms vs. error for different output variable and different length-to-thickness ratio by various models for a simply-supported plate with a distributed load.

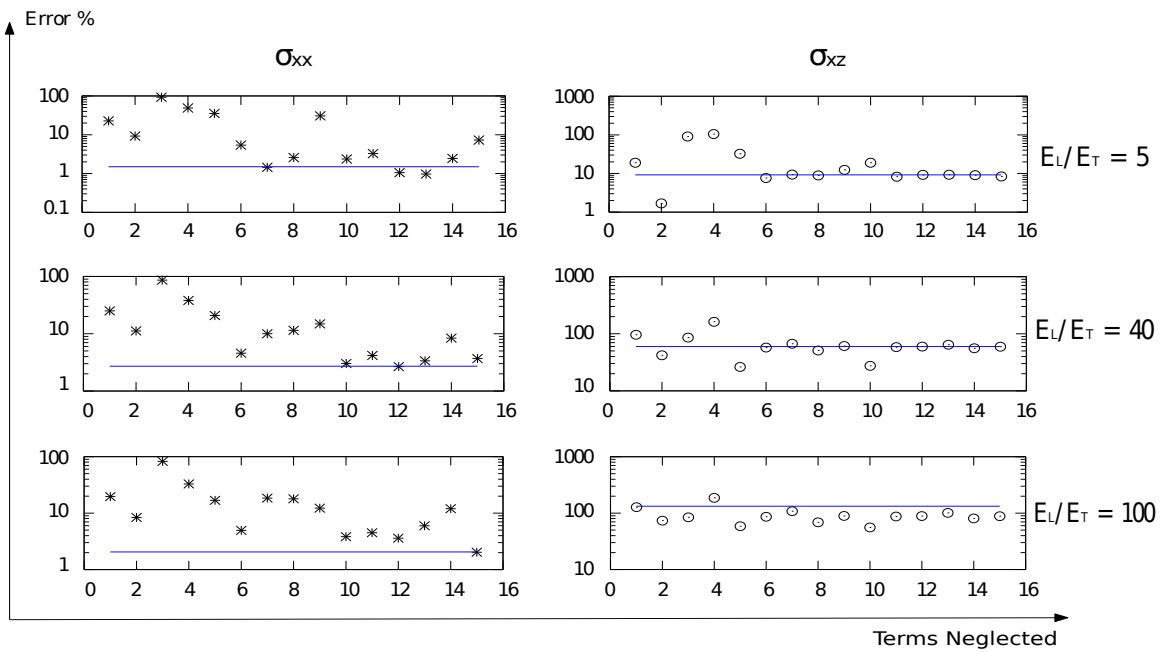
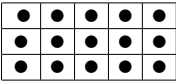
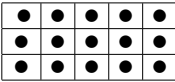
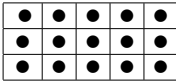
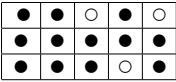
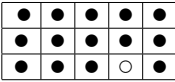
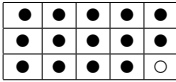
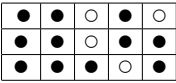
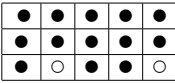
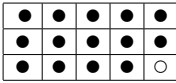
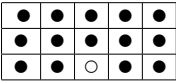
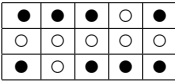
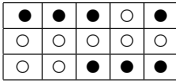
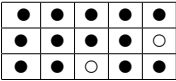
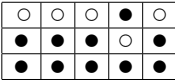
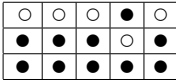
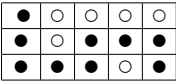
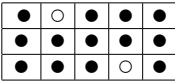
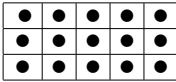
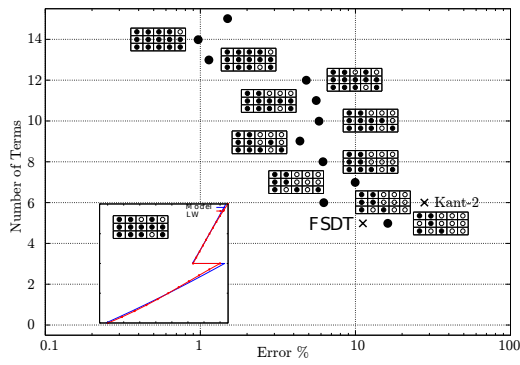


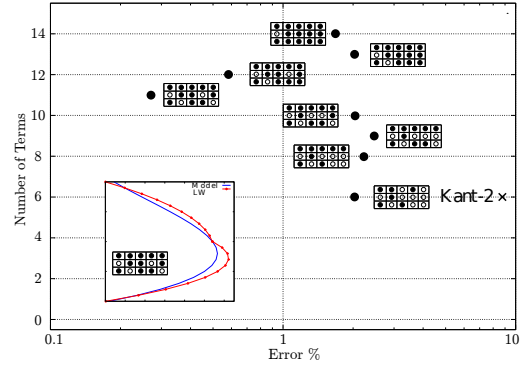
Figure 4.14 Influence of each displacement variable with respect to the reference ratio ED_4/LD_4 for different orthotropic ratios.

Table 4.24 Comparison of the sets of effective terms for an isotropic simply-supported plate loaded with a distributed load, $\theta = 0/90$, for different ortotropic ratios

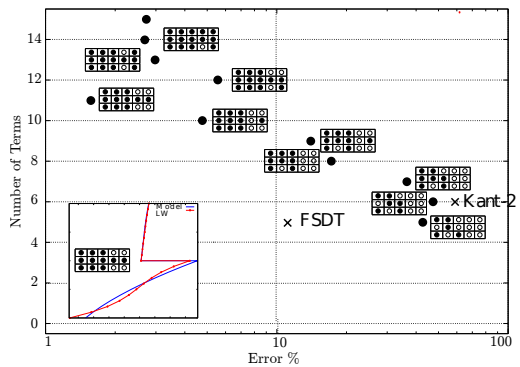
	$E_L/E_T = 5$		$E_L/E_T = 10$		$E_L/E_T = 100$	
	<i>Theory</i>	$\delta \%$	<i>Theory</i>	$\delta \%$	<i>Theory</i>	$\delta \%$
u_z		99.9		98.3		97.5
	<i>FSDT</i>	71.4	<i>FSDT</i>	76.9	<i>FSDT</i>	68.5
	<i>Kant - 2</i>	78.0	<i>Kant - 2</i>	57.4	<i>Kant - 2</i>	56.3
σ_{xx}		95.2		98.6		102.0
	<i>FSDT</i>	113.5	<i>FSDT</i>	86.8	<i>FSDT</i>	56.5
	<i>Kant - 2</i>	70.3	<i>Kant - 2</i>	40.1	<i>Kant - 2</i>	34.3
σ_{yy}		98.8		98.6		94.1
	<i>FSDT</i>	91.5	<i>FSDT</i>	85.3	<i>FSDT</i>	76.6
	<i>Kant - 2</i>	111.3	<i>Kant - 2</i>	82.7	<i>Kant - 2</i>	78.2
σ_{xz}		112.4		67.7		7.0
	<i>FSDT</i>	73.8	<i>FSDT</i>	119.7	<i>FSDT</i>	148.1
	<i>Kant - 2</i>	109.0	<i>Kant - 2</i>	169.5	<i>Kant - 2</i>	198.7
σ_{yz}		115.1		101.2		108.9
	<i>FSDT</i>	79.5	<i>FSDT</i>	134.2	<i>FSDT</i>	139.6
	<i>Kant - 2</i>	117.2	<i>Kant - 2</i>	190.1	<i>Kant - 2</i>	187.2
σ_{zz}		101.9		93.9		100.2
	<i>FSDT</i>	417.2	<i>FSDT</i>	180.5	<i>FSDT</i>	95.2
	<i>Kant - 2</i>	98.1	<i>Kant - 2</i>	86.0	<i>Kant - 2</i>	79.3



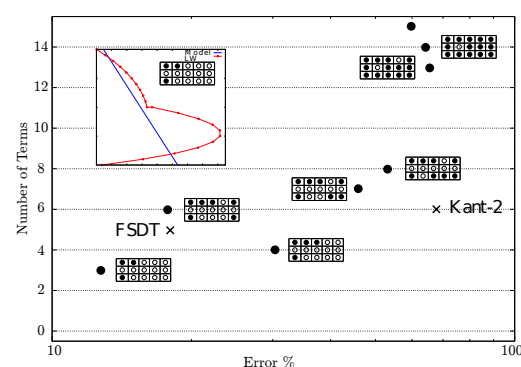
(a) $\sigma_{xx}, E_L/E_T = 5$



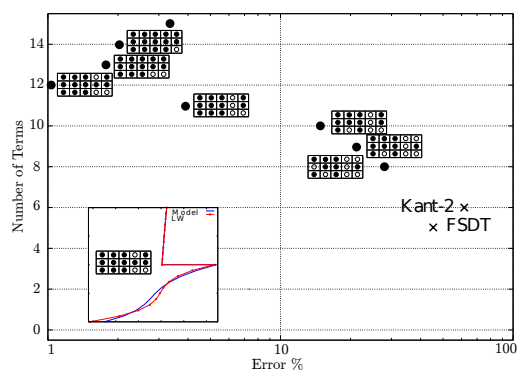
(b) $\sigma_{xz}, E_L/E_T = 5$



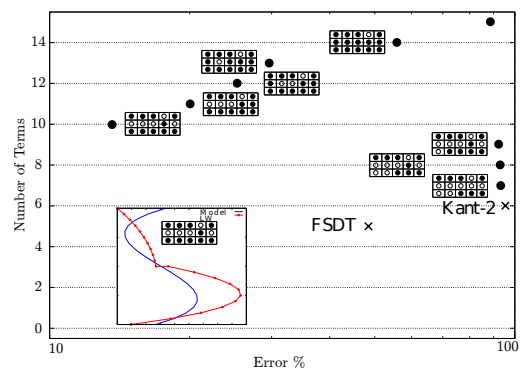
(c) $\sigma_{xx}, E_L/E_T = 40$



(d) $\sigma_{xz}, E_L/E_T = 40$



(e) $\sigma_{xx}, E_L/E_T = 100$



(f) $\sigma_{xz}, E_L/E_T = 100$

Figure 4.15 Number of terms vs. error for different output variables and different orthotropy ratios via various models for a simply-supported plate under a distributed load.

Angle ply effect The effect of the ply angle is herein investigated. An antisymmetric two layer plate is considered. E_L is equal to 40 GPa. E_T and E_z are equal to 1 GPa. ν_{LT} and ν_{Lz} are equal to 0.5 and 0.6 respectively. Each layer is 0.01 m thick. Three different plates are considered ($\theta = -15/15$, $\theta = -30/30$, $\theta = -45/45$). The effectiveness of each term is investigated for each ply angle condition. Fig. 4.16 shows the influence of each term. Table 4.25 has been obtained exploiting Fig. 4.16 with the same procedure describe in paragraph 4.1.2. For each output the reduced model obtained and its error are reported. In order to show a comparison the errors relative to the models from open literature are also reported. Varying the accepted error it is possible to determine further theories which provide solutions whit a certain degree of error compared to the reference one. Fig. 4.17 shows the obtained theories together with models retrieved from open literature. The analysis undertaken suggests the following comments:

1. The reduced plate model which are equivalent to the reference model required a great number of terms in many cases.
2. The influence of ply angle is not significant.
3. A significant computational cost reduction is detected if only one output is considered.

Effect of symmetry in lamination scheme The effect of symmetry in lamination is herein investigated. Three different square plates are considered. E_L is equal to 40 GPa. E_T and E_z are equal to 1 GPa. ν_{LT} and ν_{Lz} are equal to 0.5 and 0.6 respectively. Each layer is 0.01 m thick. The plates taken into account are ($\theta = 90/0/90$, $\theta = 90/90/0$, $\theta = 90/0/90/0$) For each plate the effectiveness of each term is investigated. The influence of each term is illustrate in Fig. 4.18. Table 4.26 has been obtained exploiting Fig. 4.18 with the same procedure described in paragraph 4.1.2 and reports the reduced model obtained with the relative error for each reduced displacement field. Fig. 4.19 shows the theories obtained varying the accepted error with models retrieved from open literature. It can be concluded that:

1. The lamination symmetry has a significant influence on the response especially for the stress output.
2. A significant computational cost reduction is detected if only one output is considered.

Second conclusion and outline A laminated plate has been considered. Layer wise fourth-order solution has been adopted as reference. The accuracy analysis has been conducted via an axiomatic approach which determines the role of each variable computing a given displacement/stress variable. In this work an approach able to construct reduced plate models equivalent to a full higher-order theory has been presented. For a given problem, we developed a procedure that is able to find the best plate theory in order to minimize computational costs. As far as the first type of models is concerned, the following conclusion can be drawn:

1. All parameters considered (thickness, orthotropic ratio, angle ply, lamination, boundary conditions and loading conditions) are important to determine the set of effective terms, that is, if only one of these parameters changes, a different plate model will be required.

2. Computing the output value in a single position, $[a/2, b/2, 0]$ for the normal stress σ_{xx} and $[0, b/2, h/2]$ for the shear stress σ_{xz} can lead to an unrealistic value of the error.
3. The different reduced models found for each parameter and for each output describe a curve that correlates the number of terms (the computational cost) and the error committed.

From Fig. 4.13, 4.15, 4.17 and 4.19 it is possible to draw a curve close to the best plate diagram BPTD. From the presented results it is possible to see that the "Influence of each terms" method is not able to draw the BPTD for composite plate.

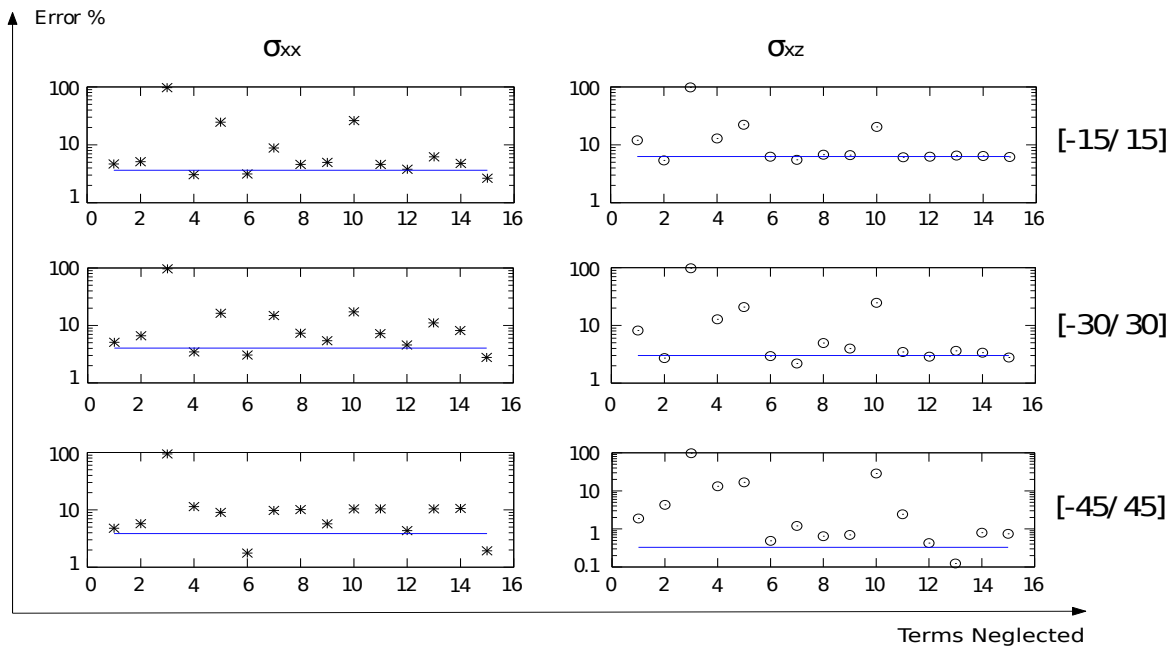
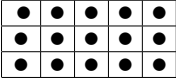
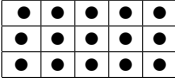
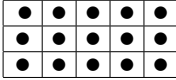
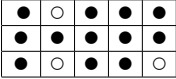
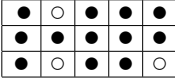
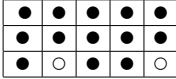
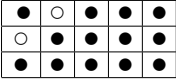
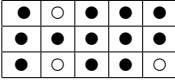
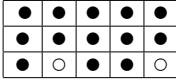
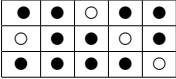
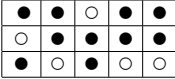
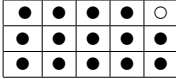
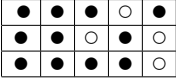
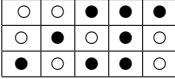
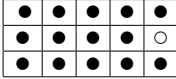
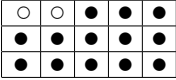
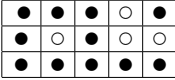
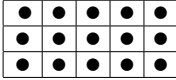
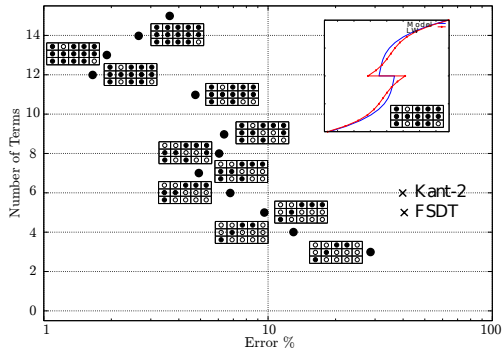


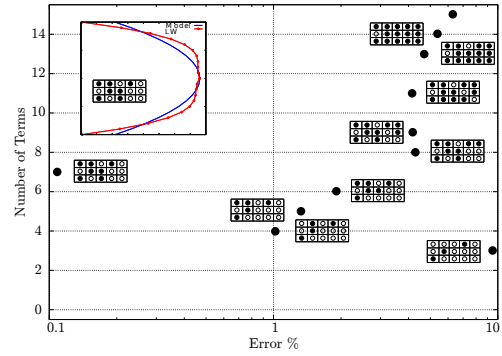
Figure 4.16 Influence of each displacement variable with respect to the reference ratio $ED4/LD4$ for different ply angle.

Table 4.25 Comparison of the sets of effective terms for an isotropic simply-supported plate loaded with a distributed load, for different anisotropy values

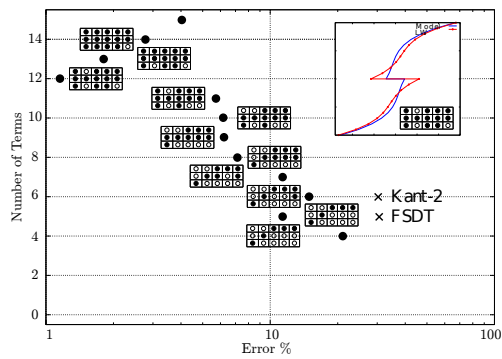
	-15 15		-30 30		-45 45	
	<i>Theory</i>	δ %	<i>Theory</i>	δ %	<i>Theory</i>	δ %
u_z		98.7		98.5		98.9
	<i>FSDT</i>	80.9	<i>FSDT</i>	75.1	<i>FSDT</i>	74.2
	<i>Kant - 2</i>	77.4	<i>Kant - 2</i>	69.4	<i>Kant - 2</i>	69.3
σ_{xx}		98.3		98.8		100.2
	<i>FSDT</i>	63.2	<i>FSDT</i>	66.4	<i>FSDT</i>	72.0
	<i>Kant - 2</i>	73.8	<i>Kant - 2</i>	67.1	<i>Kant - 2</i>	77.6
σ_{yy}		99.2		104.5		100.2
	<i>FSDT</i>	82.3	<i>FSDT</i>	68.8	<i>FSDT</i>	72.0
	<i>Kant - 2</i>	73.1	<i>Kant - 2</i>	65.1	<i>Kant - 2</i>	77.7
σ_{xz}		104.1		102.3		99.9
	<i>FSDT</i>	75.2	<i>FSDT</i>	74.2	<i>FSDT</i>	72.8
	<i>Kant - 2</i>	100.7	<i>Kant - 2</i>	99.5	<i>Kant - 2</i>	95.1
σ_{yz}		97.0		106.5		99.9
	<i>FSDT</i>	83.3	<i>FSDT</i>	85.8	<i>FSDT</i>	72.8
	<i>Kant - 2</i>	133.6	<i>Kant - 2</i>	122.1	<i>Kant - 2</i>	95.1
σ_{zz}		100.0		99.0		100.0
	<i>FSDT</i>	142.4	<i>FSDT</i>	107.0	<i>FSDT</i>	92.8
	<i>Kant - 2</i>	84.3	<i>Kant - 2</i>	82.6	<i>Kant - 2</i>	81.6



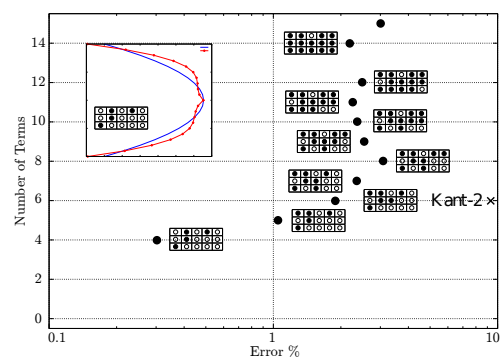
(a) $\sigma_{xx}, \theta = -15/15$



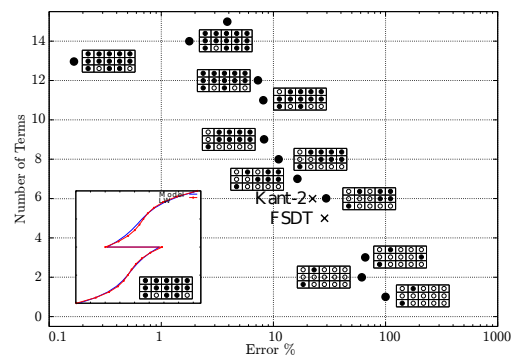
(b) $\sigma_{xz}, \theta = -15/15$



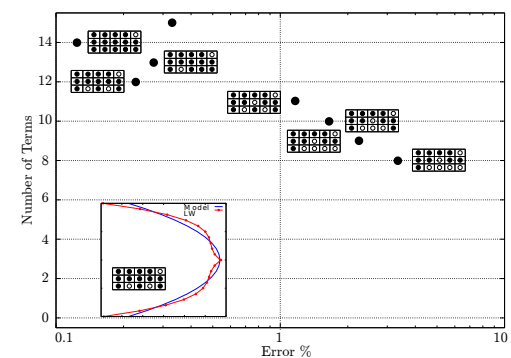
(c) $\sigma_{xx}, \theta = -30/30$



(d) $\sigma_{xz}, \theta = -30/30$



(e) $\sigma_{xx}, \theta = -45/45$



(f) $\sigma_{xz}, \theta = -45/45$

Figure 4.17 Number of terms vs. error for different output variable and different anisotropy conditions via various models for a simply-supported plate under a distributed load.

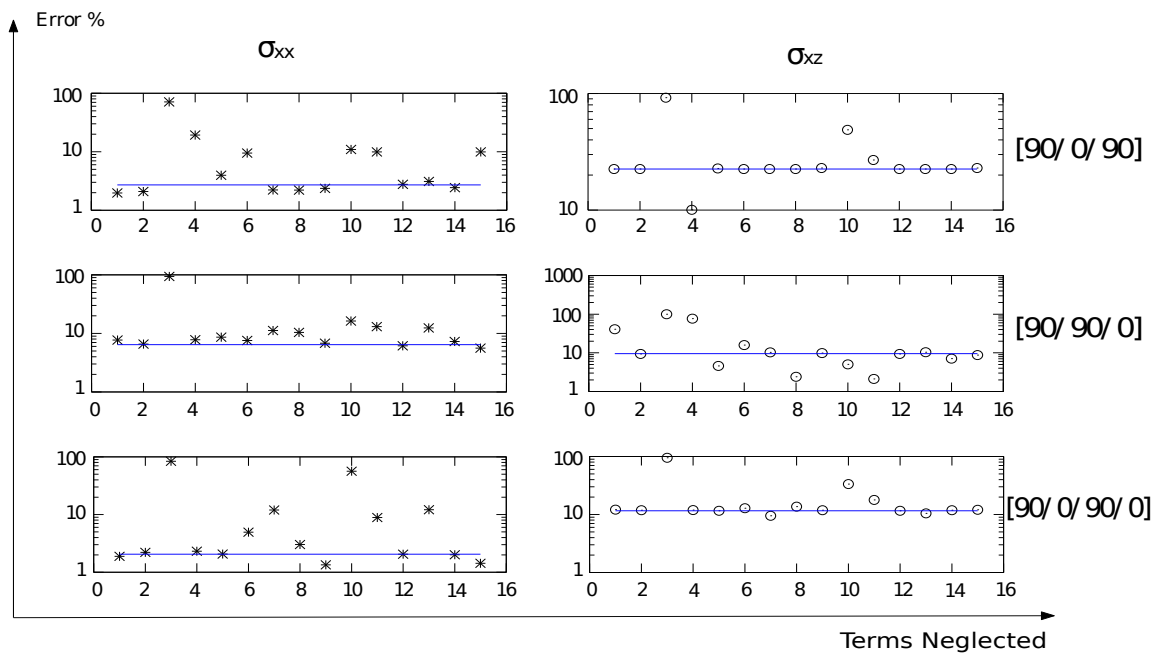
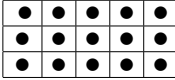
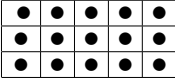
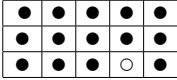
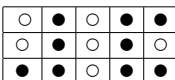
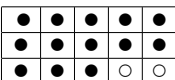
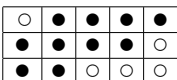
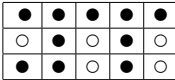
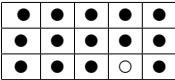
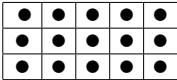
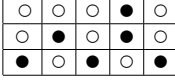
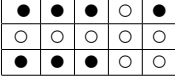
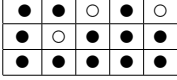
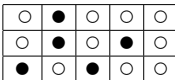
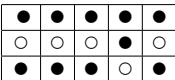
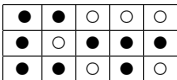
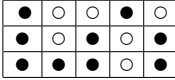
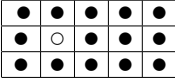
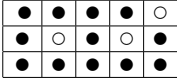


Figure 4.18 Influence of each displacement variable with respect to the reference ratio $ED4/LD4$ for different symmetric plate.

Table 4.26 Comparison of the sets of effective terms for an isotropic simply-supported plate loaded with a distributed load, for different lamination values

	90/0/90		90/90/0		90/0/90/0	
	<i>Theory</i>	δ %	<i>Theory</i>	δ %	<i>Theory</i>	δ %
u_z		97.8		98.6		98.9
	<i>FSDT</i>	84.3	<i>FSDT</i>	76.6	<i>FSDT</i>	76.7
	<i>Kant - 2</i>	91.9	<i>Kant - 2</i>	65.3	<i>Kant - 2</i>	69.6
σ_{xx}		104,1		94.7		99.0
	<i>FSDT</i>	51.9	<i>FSDT</i>	80.3	<i>FSDT</i>	45.5
	<i>Kant - 2</i>	91.7	<i>Kant - 2</i>	91.7	<i>Kant - 2</i>	100.3
σ_{yy}		93.8		105.5		100.4
	<i>FSDT</i>	44.1	<i>FSDT</i>	29.1	<i>FSDT</i>	13.9
	<i>Kant - 2</i>	90.2	<i>Kant - 2</i>	50.0	<i>Kant - 2</i>	58.0
σ_{xz}		110.1		66.7		89.7
	<i>FSDT</i>	134.9	<i>FSDT</i>	100.7	<i>FSDT</i>	63.1
	<i>Kant - 2</i>	197.2	<i>Kant - 2</i>	155.1	<i>Kant - 2</i>	80.0
σ_{yz}		98.4		92.6		94.2
	<i>FSDT</i>	79.2	<i>FSDT</i>	64.8	<i>FSDT</i>	74.8
	<i>Kant - 2</i>	93.9	<i>Kant - 2</i>	66.1	<i>Kant - 2</i>	94.8
σ_{zz}		100.4		99.2		101.3
	<i>FSDT</i>	77.9	<i>FSDT</i>	66.0	<i>FSDT</i>	22.3
	<i>Kant - 2</i>	84.8	<i>Kant - 2</i>	80.4	<i>Kant - 2</i>	74.8

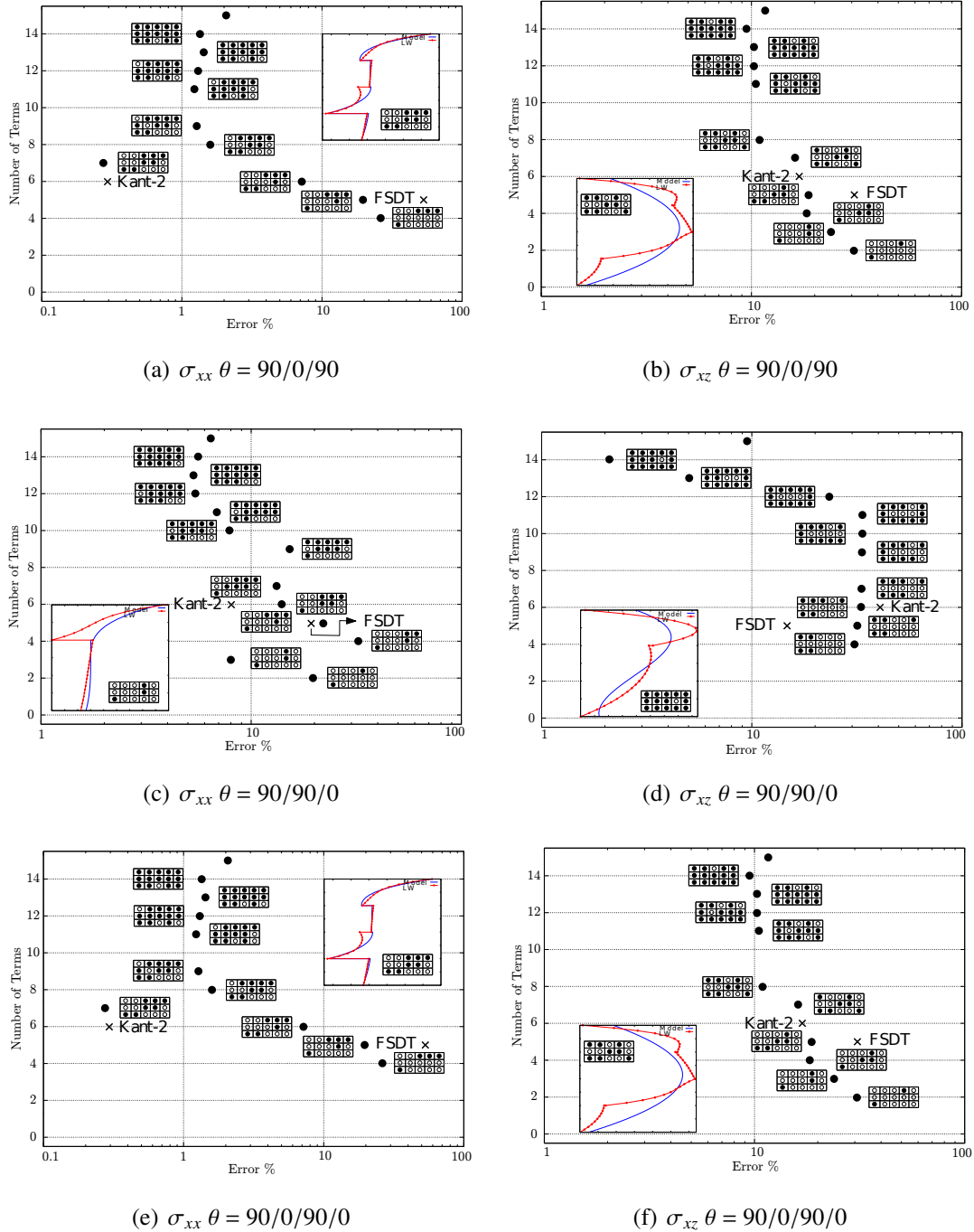


Figure 4.19 Number of terms vs. error for different output variables and different lamination conditions via various models for a simply-supported plate under a distributed load.

4.2 Genetic optimization method

4.2.1 Laminated Plates

A laminated plate was considered. The geometry of the plate is shown in Fig. 4.9, where a is 0.1 [m], and b is equal to a . σ_{xx} is computed at $[a/2, b/2, z]$ with $0 < z < h$. Stresses are computed directly from the constitutive equations. Four-node plate elements were used, and a uniform mesh of 15×15 elements was adopted. Shear locking problems were solved by using mixed interpolation of tensorial components (previously extended to CUF in (72)). A fourth-order Layer Wise model was adopted as the reference for the following analysis. A simply-supported orthotropic plate loaded with a distributed load was considered. A bi-sinusoidal transverse distributed load P_z was applied at the top surface:

$$P_z = p_z \sin\left(\frac{mx}{a}\right) \cos\left(\frac{ny}{b}\right) \quad (4.4)$$

where load amplitude p_z is equal to 1 [kPa]; m and n are the wave numbers in the two in-plane plate directions, both of them equal to 1. The variation of different parameters was investigated.

Effect of Length-to-thickness ratio Three different length-to-thickness ratio (a/h) sets were considered:

1. very thick plates ($a/h = 50$);
2. thick plates ($a/h = 5$);
3. thin plates ($a/h = 2.5$).

An unsymmetrical cross-ply (0/90) square plate were considered. E_L was considered equal to 40 GPa. E_T and E_z were set equal to 1 GPa. ν_{LT} and ν_{Lz} were defined equal to 0.5 and 0.6 respectively. An initial population of one hundred and fifty different displacement models was created in a random way. The genetic algorithm was applied on these initial displacement models in order to obtain the Best Plate Theory Diagram after several generations. In Fig. 4.20 the evolution of the initial population through twenty generations for a very thick plate is shown. There are five generations between each graph. Each individual is represented in the figure by a circular marker. The abscissa axis reports the number of active terms of the plate models and the ordinate axis reports the error that each individual makes. Twenty generations were used, since the populations reach convergence at this number. Each generation has approximately three hundred individuals. This number ensures good biodiversity and at the same time keeps computational time low. The application of the genetic code leads to the results shown in Fig. 4.21 for plates with a different length to thickness ratio. The figures were obtained considering the stress σ_{xx} as output. The figure shows the best plate theory diagram and for three different plate theories the evolutions of the considered outputs along the thickness are illustrated and, compared with the reference model. These graphs are reported in order to demonstrate that the stress computed through the reduced models is very close to the stress computed through the reference model. Furthermore, through the genetic algorithm it is possible to obtain the influence of each term expansion in function of the number of active terms and the problem.

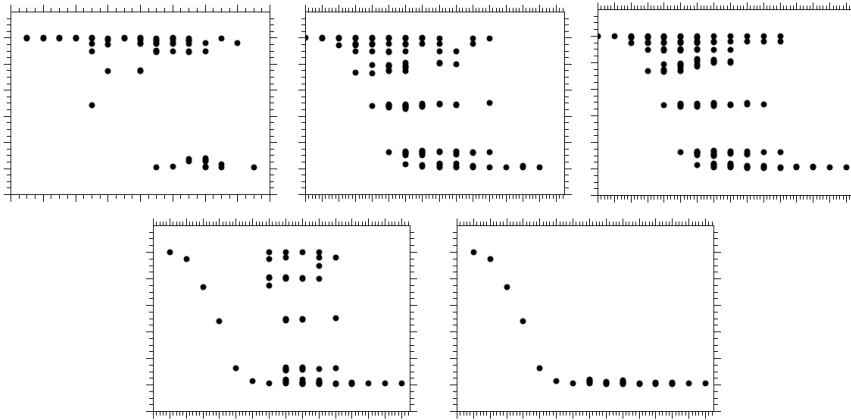
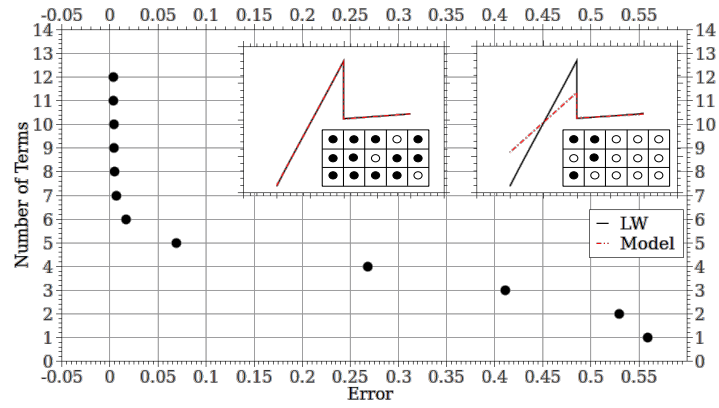


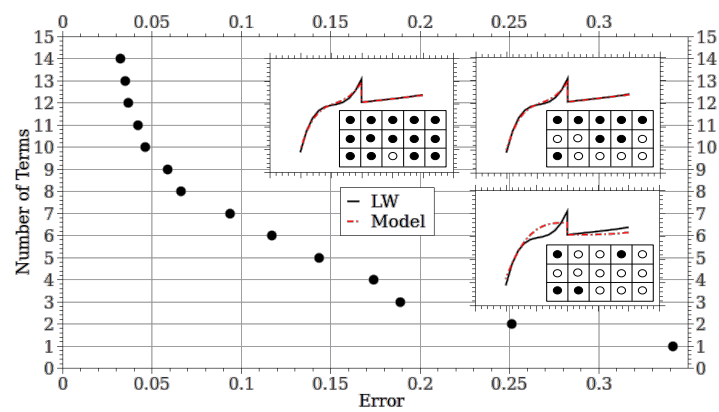
Figure 4.20 Evolution of an initial population through twenty generations; there are five generations between each graph.

Monitoring the best individual of each generation and recording their “DNA” it is possible to draw the graphs of Fig. 4.22 which report the influence of each displacement variable in function of the number of active terms. For example in Fig. 4.22 (b) it can be seen that the term 4, u_3x^4 , is fundamental if the number of active terms are two while it is useless if the number of active terms is six or seven. The scale of the graphics has been normalized in order to separate the influence of terms from the number of generation. In Fig. 4.23 the BPTDs and the plate theories obtained from the literature are shown in the same graphs. From Fig. 4.23 it is possible to see that the theories obtained from the literature are not the best for the three problems considered.

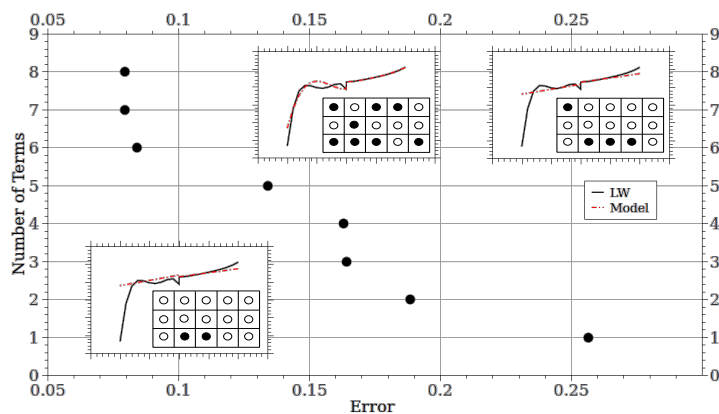
Effect of Orthotropic ratio An unsymmetrical cross ply (0/90) square plate was considered. E_T and E_z were set equal to 1 GPa. ν_{LT} and ν_{Lz} were defined equal to 0.5 and 0.6 respectively. Each layer was 0.01 m thick. Three different orthotropic ratios were considered ($E_L/E_T = 5$, $E_L/E_T = 40$, $E_L/E_T = 100$). A genetic optimization code was used to compute the Best Plate Theory diagram. Twenty generations were used. Each generation is made up of approximately three hundred individuals. Considering σ_{xx} as the output, the BPTD obtained is shown in Fig. 4.24. The figure shows the best plate theory diagram and the evolutions of the considered outputs along the thickness compared with the reference model for three different plate theories. Fig. 4.25 shows the importance of each term expansion in function of the number of active terms and the problem considered. It is possible to see that some terms are either essential or useless in function of the number of active terms. Fig. 4.26 illustrates the comparison between the present best plate theory diagrams and some known theories from open literature. For the three orthotropic ratios considered, the optimization genetic code found the best models in terms of accuracy vs. computational times. An example can be derived from Fig. 4.26(a); using the



(a) $a/h = 50$

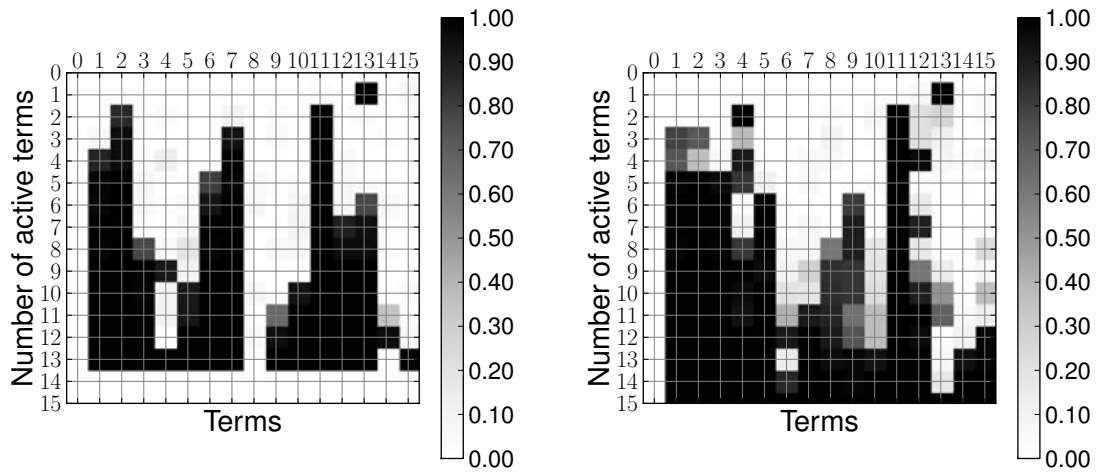


(b) $a/h = 5$



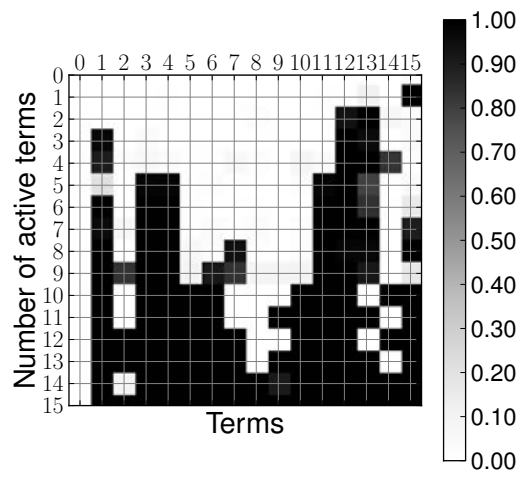
(c) $a/h = 2.5$

Figure 4.21 Best Plate Theory Diagram for the different length to thickness ratio.



(a) $a/h = 50$

(b) $a/h = 5$



(c) $a/h = 2.5$

Figure 4.22 Influence of the expansion variable in function of the number of active terms and the problem.

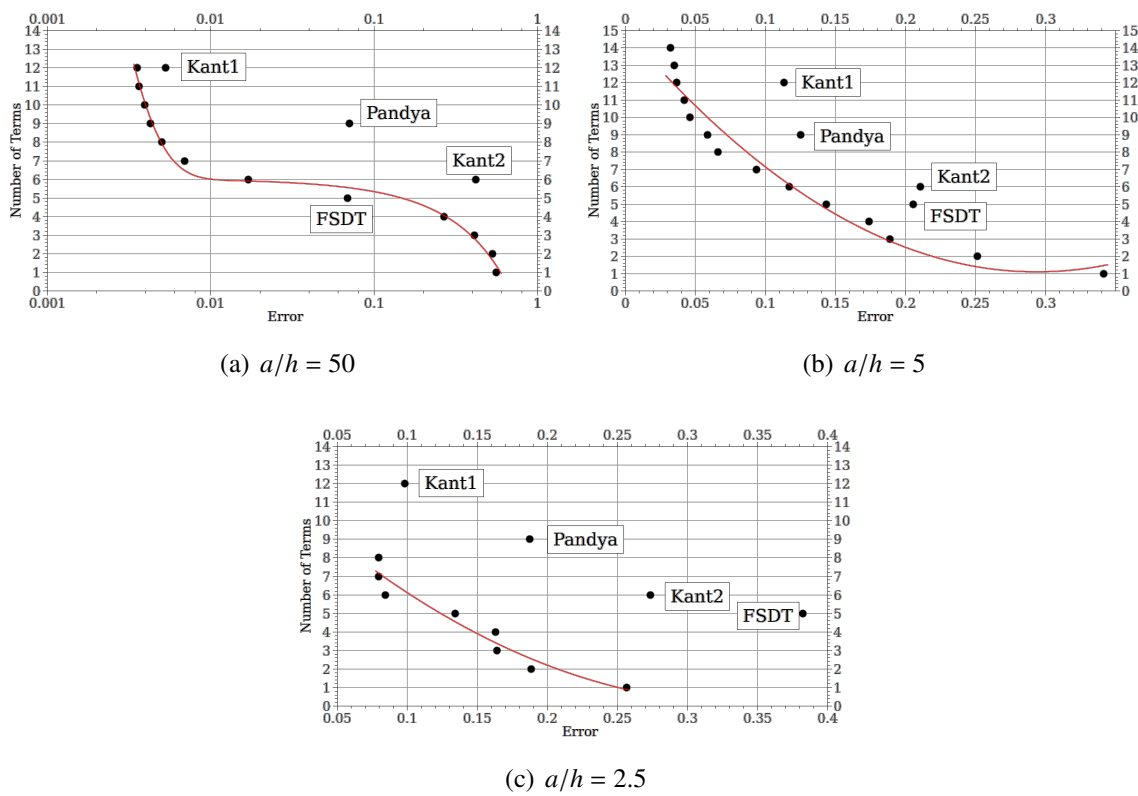
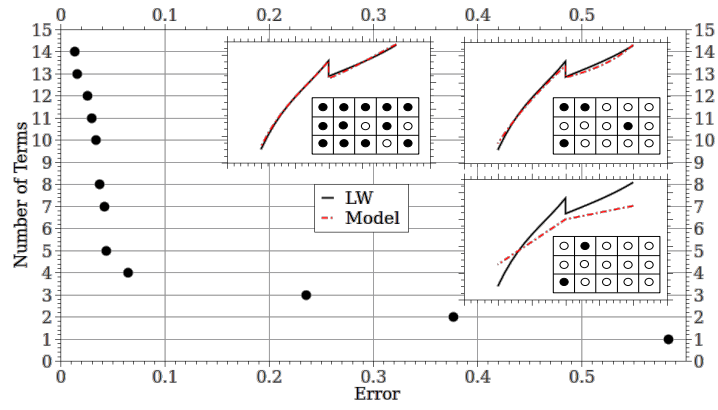
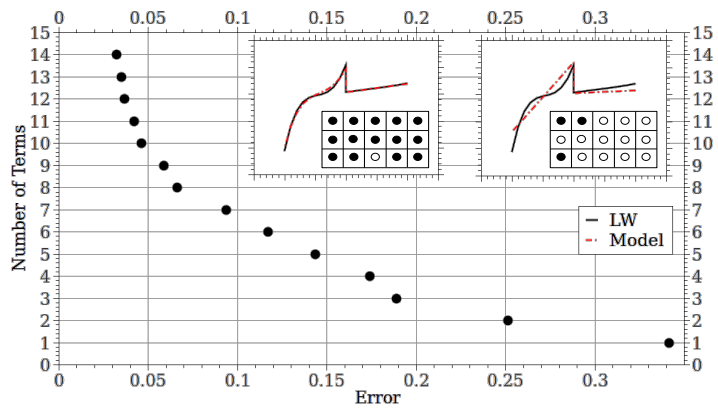


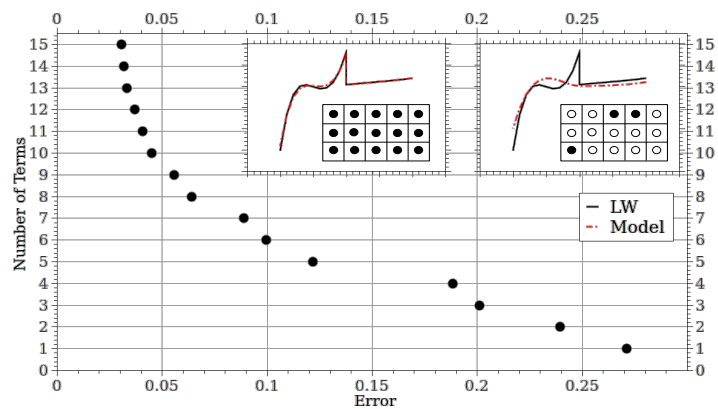
Figure 4.23 Comparison between present best plate theory diagrams and some known theories from open literature.



(a) $E_L/E_T = 5$

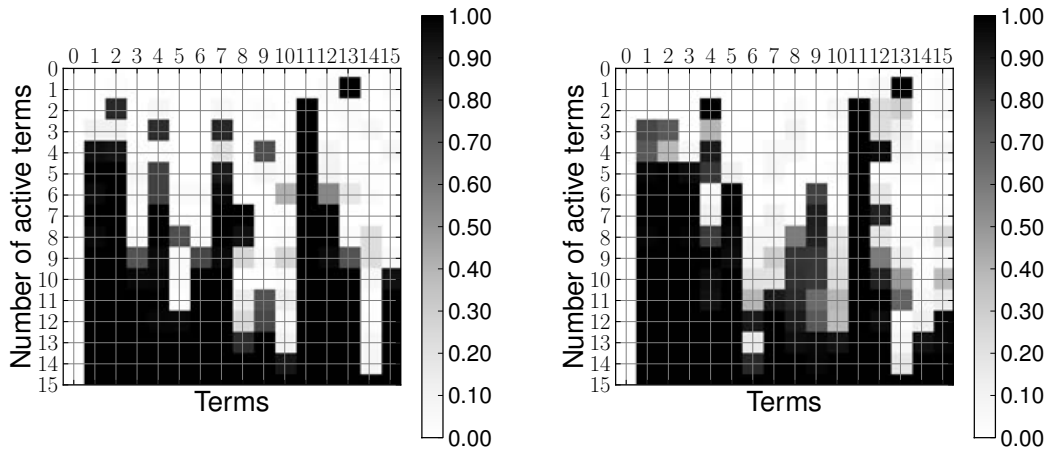


(b) $E_L/E_T = 40$



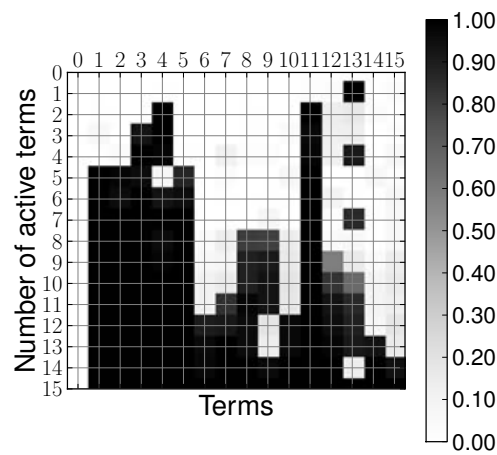
(c) $E_L/E_T = 100$

Figure 4.24 Best Plate Theory Diagram for the different orthotropic ratio.



(a) $E_L/E_T = 5$

(b) $E_L/E_T = 40$



(c) $E_L/E_T = 100$

Figure 4.25 Influence of the expansion variable in function of the number of active terms and the problem.

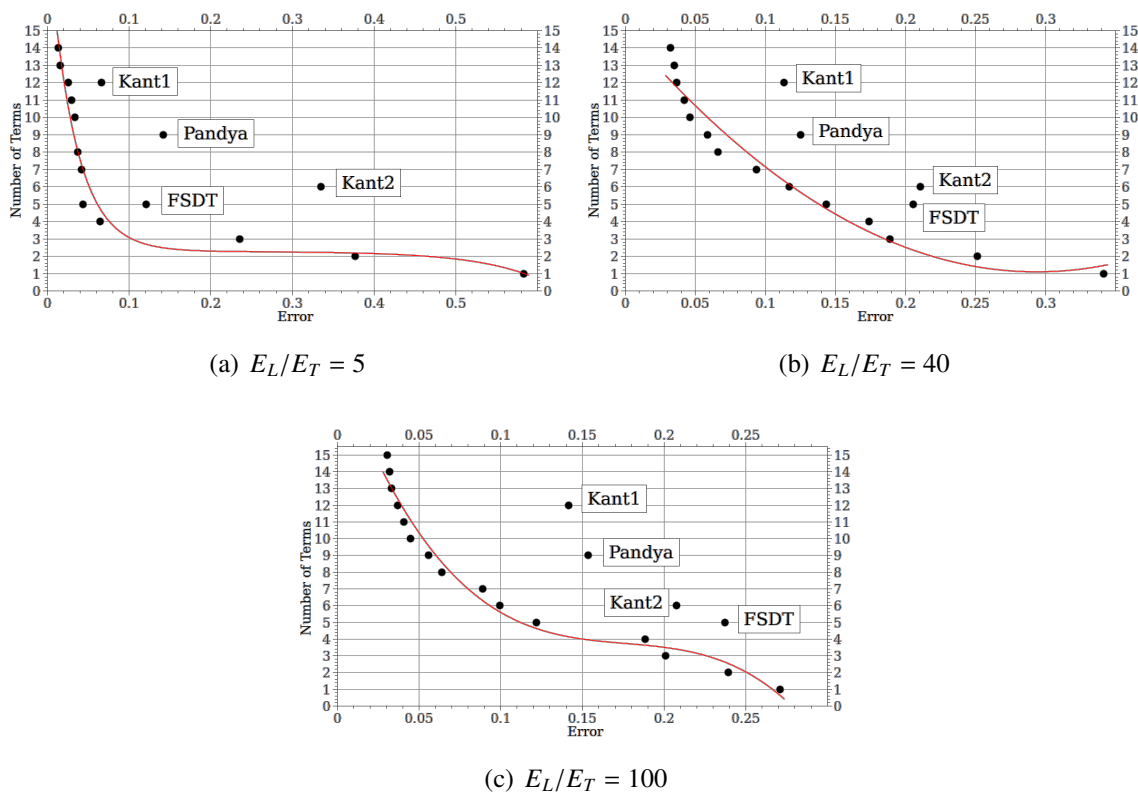


Figure 4.26 Comparison between present best plate theory diagrams and some known theories from open literature.

model obtained through the genetic code:

$$\begin{aligned}
 u_x &= u_{x0} + z u_{x1} + z^2 u_{x2} + z^3 u_{x3} + z^4 u_{x4} \\
 u_y &= u_{y0} + z u_{y1} + z^3 u_{y3} \\
 u_z &= u_{z0} + z u_{z1} + z^2 u_{z2} + z^4 u_{z4}
 \end{aligned} \tag{4.5}$$

instead of the Kant1 (see Kant (69)):

$$\begin{aligned}
 u_x &= u_{x1} + z u_{x2} + z^2 u_{x3} + z^3 u_{x4} \\
 u_y &= u_{y1} + z u_{y2} + z^2 u_{y3} + z^3 u_{y4} \\
 u_z &= u_{z1} + z u_{z2} + z^2 u_{z3} + z^3 u_{z4}
 \end{aligned} \tag{4.6}$$

it is possible to decrease the error with the same computational time.

Angle ply-plate An antisymmetric two layer plate was considered. E_L was considered equal to 40 GPa. E_T and E_z were defined equal to 1 GPa. ν_{LT} and ν_{Lz} were set equal to 0.5 and 0.6 respectively. Each layer was 0.01 m thick. Three different plates were considered ($\theta = -15/15$, $\theta = -30/30$, $\theta = -45/45$). The genetic optimization code was used to draw the best plate theory diagram for the three plates considered. The BPTDs are reported in Fig 4.27. In the same graph the plate theories obtained from the bibliography are also reported.

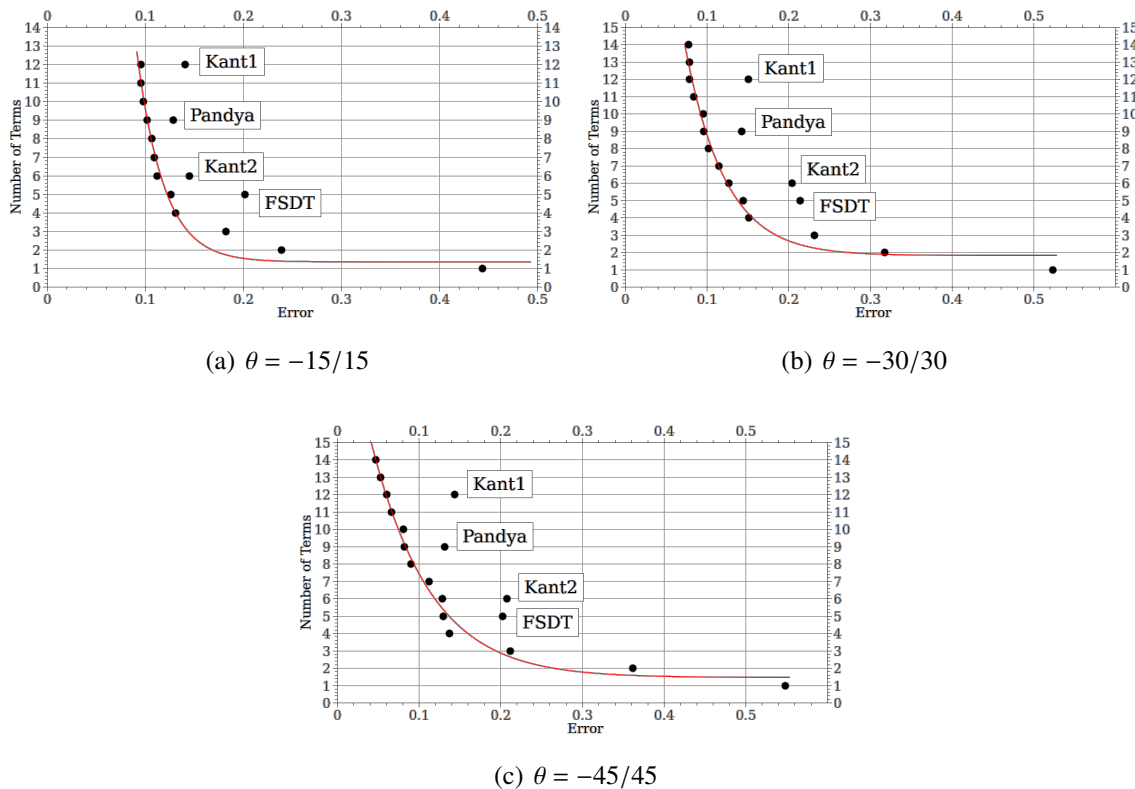


Figure 4.27 Comparison between present best plate theory diagrams and some known theories from open literature.

Symmetry in lamination scheme Three different square plates were considered. E_L was equal to 40 GPa. E_T and E_z were considered equal to 1 GPa. ν_{LT} and ν_{Lz} were set equal to 0.5 and 0.6 respectively. Each layer was 0.01 m thick. The plates taken into account were ($\theta = 90/0/90$, $\theta = 90/90/0$) The genetic optimization code was used to draw the best plate theory diagram for the three plates considered. The BPTDs are reported in Fig 4.28. In the same graph the plate theories obtained from the bibliography are displayed.

4.2.2 Sandwich plate

A sandwich-thin, rectangular plate was considered. The plate was simply supported in correspondence to its four edges. The plate geometry was as follows: width $a = 100$ [mm], length b

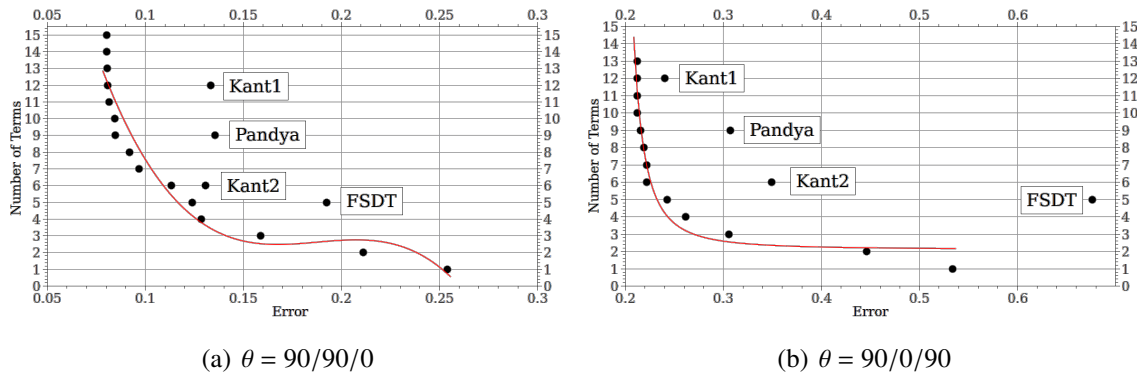


Figure 4.28 Comparison between present best plate theory diagrams and some known theories from open literature.

= 200 [mm], total thickness $h = 12$ [mm]. The faces of the same material had different thicknesses: top face thickness $h_3 = 0.1$ [mm], bottom face thickness $h_1 = 0.5$ [mm]. The core thickness was $h_2 = 11.4$ [mm]. The geometry of the plate is shown in Fig. 4.29. Four-node

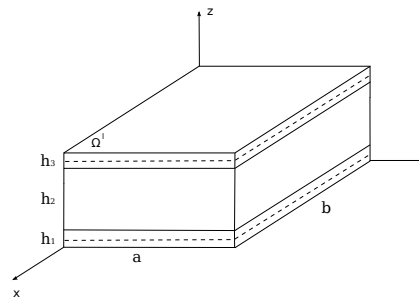


Figure 4.29 Sandwich Plate Geometry

plate elements were used, and a uniform mesh of 15×15 elements was adopted. Shear locking problems were solved by using mixed interpolation of tensorial components (previously extended to CUF in (72)). A fourth-order Layer Wise model has been adopted as the reference for the following analysis. A bi-sinusoidal transverse distributed load P_z was applied at the top surface:

$$P_z = p_z \sin\left(\frac{mx}{a}\right) \cos\left(\frac{ny}{b}\right) \quad (4.7)$$

where load amplitude p_z was equal to 1 [kPa]; m and n are the wave numbers in the two in-plane plate directions, both of them equal to 1. The two faces had the following material properties: $E_1 = 70000$ [MPa], $E_2 = 71000$ [MPa], $E_3 = 69000$ [MPa], $G_{13} = 26000$ [MPa], $G_{23} = 26000$ [MPa], $G_{12} = 26000$ [MPa], $\nu_{13} = 0.3$ [MPa], $\nu_{23} = 0.3$ [MPa] and $\nu_{12} = 0.3$ [MPa]. The core consisted of metallic foam which had the following material properties: $E_1 = 3$ [MPa], $E_2 = 3$ [MPa], $E_3 = 2.8$ [MPa], $G_{13} = 1$ [MPa], $G_{23} = 1$ [MPa], $G_{12} = 1$ [MPa], $\nu_{13} = 0.25$ [MPa], $\nu_{23} = 0.25$ [MPa], $\nu_{12} = 0.25$ [MPa]. A genetic optimization code was used to computed the Best

Plate Theory diagram. Twenty generations were imposed. Each generation was composed approximately of three hundred individuals Fig. 4.30 was obtained considering the stress σ_{xx} as output . Fig. 4.30 shows the Best Plate Theory Diagram and, for two different plate, theories the evolutions of the considered outputs along the thickness, compared with the reference model. The BTPD and some plate theories obtained from bibliography are reported in Fig. 4.31.

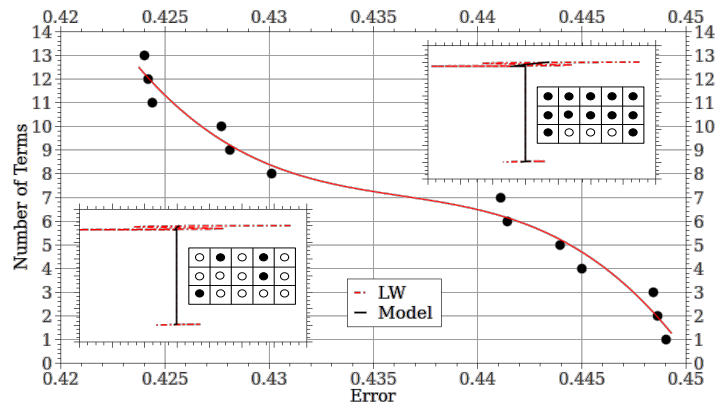


Figure 4.30 Best Plate Theory Diagram

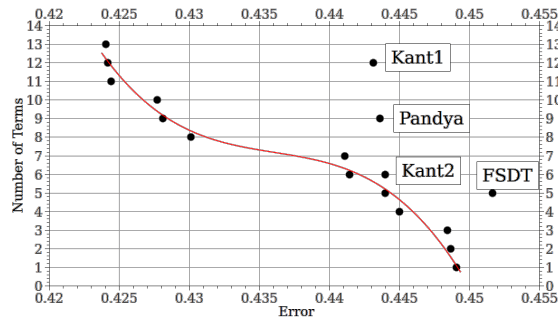


Figure 4.31 Comparison between present best plate theory diagrams and some known theories from open literature.

Conclusion and outline The presented results have highlights that it is possible to build a method able to answer to the following fundamental questions :

- what is the 'minimum' number of the terms, N_{min} , to be used in a Finite Element Plate model?
- Which are the terms to be retained, that is, which are the generalized displacement variables to be used as FE DOFs?

The answer to these questions is summarized in the plots like the one displayed in Fig. 4.7 that gives the number of terms in function of the allowed error. This plot can be defined as Best finite

element Plate Theory Diagram (BPTD), since it allows to edit an arbitrary given theory in order to have a lower amount of terms for a given error (vertical shift, Δ_N) or to increase the accuracy while keeping the computational cost constant (horizontal shift, Δ_{error}). For simple problems it is possible to build the BPTD only evaluating the influence of each terms, neglecting the an-useful. For more complicated problems, like for instance the laminated plate, it is necessary use the genetic optimization method. It is important to understand that the BPTD is strongly problem dependent, and it has the following properties:

- it changes by changing the problem characteristics (a/h , loadings, boundary conditions, etc.);
- it changes by changing output variables (displacement/stress components, or a combination of these).

In the present work the space solutions considered are bi-dimensional but it is possible to expand them to an N-dimensional space in order to identify a best plate theory diagram that is able to satisfy more than one output at the same time. The use of CUF , which makes it possible to build in a different reduced automatic manner, along with a genetic optimization code, has led to the possibility of identifying a tool that build up the BPTD.

4.3 Piezoelectric analysis

This section deals with structural analysis of isotropic and composite structures. The aim of this section is to provide numerical examples able to highlight the enhanced capabilities of the 1D electro-mechanical formulation. The following set of results aims to verify the present method for cases where piezoelectric material in the structure is used for actuation or sensors.

Piezoelectric polyvinylidene (PVDF) bimorph beam.

Actuator case The structure is a cantilever beam consisting of two layers of PVDF placed back to back with opposite polarities. The total height or thickness is 0.001 m, the length is 0.1 m and the width is 0.005 m. The cantilever is fixed on the left end and electric potential of 1 V is applied across the thickness. The relevant data are shown in Table 4.27. The

Table 4.27 Properties for bimorph cantilever beam.

	PVDF	
Elastic modulus	2.00×10^9	<i>Pa</i>
Shear modulus	7.75×10^8	<i>Pa</i>
Mass density	1.80×10^3	<i>Kgm⁻³</i>
Poisson's ratio	0.29	--
e_{31} Piezo	0.046	<i>Cm⁻²</i>
e_{32} Piezo	0.046	<i>Cm⁻²</i>
Elec. perm. χ_{11}	1.06×10^{-10}	<i>Fm⁻¹</i>
Elec. perm. χ_{22}	1.06×10^{-10}	<i>Fm⁻¹</i>
Elec. perm. χ_{33}	1.06×10^{-10}	<i>Fm⁻¹</i>
<i>L</i> length	0.1	<i>m</i>
<i>h</i> height	0.001	<i>m</i>
<i>b</i> width	0.005	<i>m</i>

geometry of the beam is reported in Fig. 4.32. The numerical results for the present method are

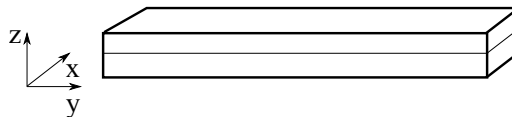


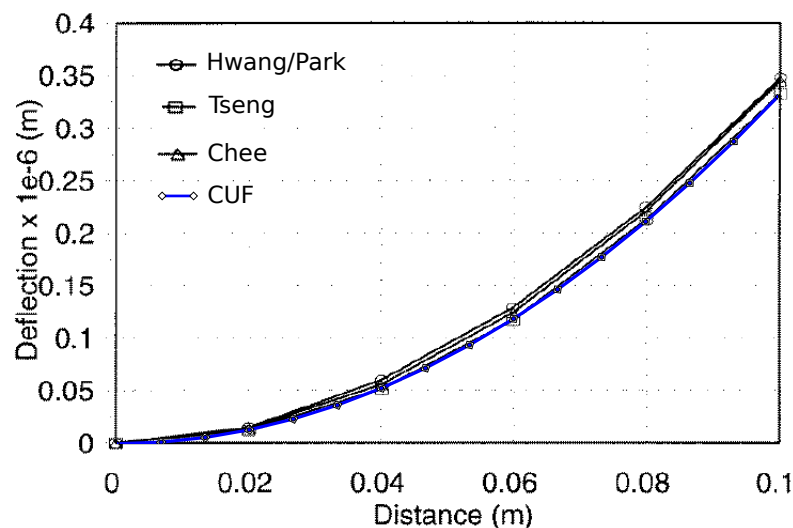
Figure 4.32 Geometry of the bimorph cantilever beam.

compared with results from other methods in Table 4.28 Veley and Rao (86) used a 2D plane stress element modified with pseudo-nodes to include the electric potential DOF. Tzou and Ye (85), using triangular shell elements which have both mechanical (using FOSDT) and electrical DOFs, showed that they produced better results than the thin solid linear elements used by Tzou. Both Veley and Rao and Tzou and Ye compared their results with Tzou's shell theory.

Table 4.28 Deflections along length of beam. 1V

Position (m)	Chee-tong (84) w(m)	Theory-Tzou (85) w(m)	FEM-Veley (86) w(m)	Solid FE-Tzou (85) w(m)	Shell FE-Tzou/Ye (85) w(m)	CUF 1D w(m)
0.00	0.000	0.000	0.000	0.000	0.000	0.000
0.02	1.380×10^{-8}	1.380×10^{-8}	1.38×10^{-8}	1.24×10^{-8}	1.32×10^{-8}	1.316×10^{-8}
0.04	5.520×10^{-8}	5.520×10^{-8}	5.520×10^{-8}	5.08×10^{-8}	5.280×10^{-8}	5.266×10^{-8}
0.06	1.242×10^{-7}	1.242×10^{-7}	1.242×10^{-7}	1.16×10^{-7}	1.190×10^{-7}	1.185×10^{-7}
0.08	2.208×10^{-7}	2.210×10^{-7}	2.210×10^{-7}	2.10×10^{-7}	2.110×10^{-7}	2.106×10^{-7}
0.10	3.450×10^{-7}	3.450×10^{-7}	3.450×10^{-7}	3.30×10^{-7}	3.300×10^{-7}	3.2920×10^{-7}

Chee et.al. (84) uses Hermitian beam elements with electric potential incorporated via the layerwise formulation, has a high correlation with Tzou's theoretical shell solutions and the results of Veley and Rao. Hwang and Park (87) used a classical displacement field with five plate elements for the same problem. Separate actuator and sensor equations were used to calculate control forces for actuation and to calculate charges for sensing which were not incorporated into their FE analysis. The deflection of the cantilever bimorph along the length (same model as above) using the present method is compared with Hwang and Park (87) (including Tseng's data) in fig. 4.33. In addition, the effect of varying the input actuation voltage (0-200 V) was

**Figure 4.33** Actuator configuration. Deflection of the bimorph cantilever along its length.

found to be linearly proportional to the tip displacements of the bimorph cantilever. This finding agrees very well with Hwang and Park (87) and Tseng and Tzou (data by Tzou and Tseng were obtained from the 1993 article of Hwang and Park) as shown in fig. 4.34. This cantilever bimorph PVDF model does not include the e_{33} , e_{15} piezoelectric constants hence their effects are neglected. Thus the linearity between tip displacement and voltage found in this case study may not necessarily hold for other structural configurations with different property types and boundary conditions.

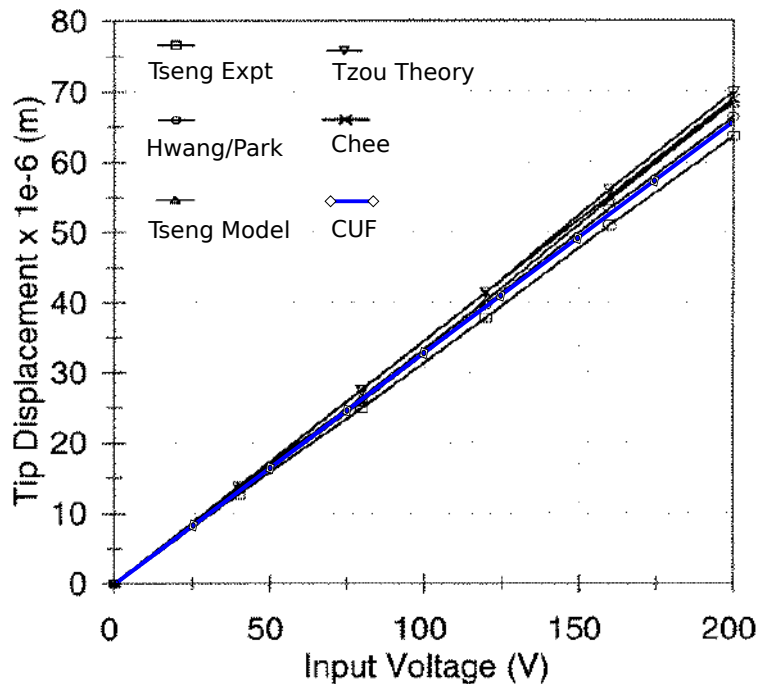


Figure 4.34 Actuator configuration. Tip deflection of the bimorph cantilever as a function of input actuator voltage.

Sensor case The bimorph is now acting as a sensor and the problem is defined as a cantilever with a vertical tip displacement of 1 cm. The aim is to determine the voltage difference across the top and bottom layers of the PVDF cantilever. The implementation of this case is the same as case before, except for the boundary (electrical and mechanical) conditions. The total voltage difference across the PVDF bimorph cantilever is plotted along the length of the cantilever as shown in Fig. 4.35. In the model of Hwang and Park there are five pieces of separate electrodes that cover the entire length of the beam. Each piece of electrode, being an equipotential surface, must have a constant voltage, hence the step distribution in Fig. 4.35. However, in practice, it should be possible to have point electrodes located at positions of interest.

Three-layer active cantilever.

Actuator Case This three-layered cantilever structure, studied by Saravanos and Heyliger (88), consists of a substrate (bottom layer), adhesive (middle layer) and piezoelectric material (top layer). The piezoelectric will act as an actuator with an applied voltage difference of 12.5 kV across the thickness direction (Saravanos and Heyliger used such a high voltage in order to compare their results with Robbins and Reddy (89) who applied an induced strain actuation of 0.1%). The substrate is isotropic aluminum or Gr/epoxy composite [0] T300/934. The material properties and the relevant data are found in Table 4.29. The geometry of the beam is reported in Fig 4.36. The length and width of the three layers are the same but the thickness of the substrate and piezoelectric are 1/10 and 1/100 of the length respectively. Two scenarios were studied: an aluminum substrate and a unidirectional T300/934 substrate. The results are displayed in Fig.

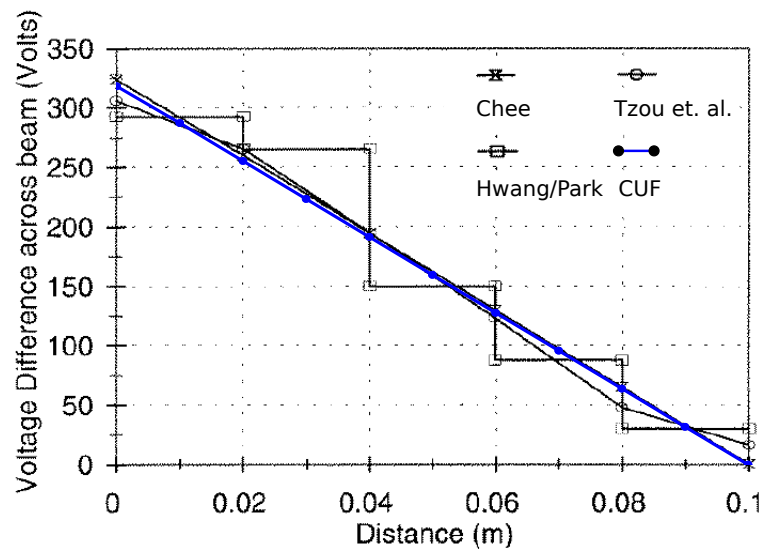


Figure 4.35 Sensor configuration. Voltage difference across thickness of PVDF at various points along the length of the cantilever.

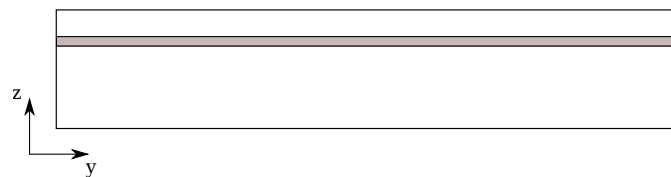


Figure 4.36 Three-layer actuator/sensor cantilever beam.

4.37 together with the results obtained by Saravanos and Heyliger (88) and Chee et.al. (84). The aluminum beam is deflected more than the Gr/epoxy beam as expected because the latter is stiffer in the x-direction. From the graph it is possible to see that the CUF formulations is able to reproduce the results.

Sensor Case In this section, the sensory capability is investigated. The electric potential at the top and the middle level of the piezoelectric material were taken as free/sensing variables. A load of 1000 N upwards was applied to the cantilever tip to make the beam bend upwards. Due to the electro-mechanical coupling, charges were generated on the piezoelectric which resulted in a potential difference. The mid-plane deflections along the beam and the total voltage across the thickness of the piezoelectric are plotted in Fig. 4.38 and Fig. 4.39 respectively.

Aluminum cantilever beam with two thin piezo-ceramic PSI-5A-S3 sheets An aluminium beam with two thin piezo-ceramic sheets considered in the works of Yocum and Abramovich (91) is studied. The material property and the geometry of the beam are reported in Table 4.30 and Fig. 4.40. The comparison between the experiment and ADINA results obtained from the work of Yocum and Abramovich (91) and the present model are reported in Fig. 4.41 and 4.42. The comparison when one piezo-actuator is activated is reported in Fig. 4.41. The comparison

Table 4.29 Properties for three-layer cantilever (data obtained from Saravanos and Heyliger (88), Saravanos (90))

	Aluminium	T300/934	Adhesive	PZT-4	
E_{33}	6.8900×10^{10}	1.3238×10^{11}	6.9000×10^9	8.1300×10^{10}	<i>Pa</i>
E_{11}	6.8900×10^{10}	1.0760×10^{10}	6.9000×10^9	6.4500×10^{10}	<i>Pa</i>
ν_{13}	0.25	0.24	0.4	0.43	–
G_{13}	2.7600×10^{10}	5.6500×10^9	2.4600×10^9	2.5600×10^{10}	<i>Pa</i>
d_{32}	–	–	–	-1.22×10^{-10}	<i>m/V</i>
<i>Elec. Perm.</i> χ_{22}	–	3.0989×10^{-11}	–	1.3059×10^{-8}	<i>F/m</i>
<i>Elec. Perm.</i> χ_{33}	–	2.6562×10^{-11}	–	1.1510×10^{-8}	<i>F/m</i>
<i>Length L</i>	0.1524	0.1524	0.1524	0.1524	<i>m</i>
<i>Thickness h</i>	0.01524	0.01524	0.000254	0.001524	<i>m</i>
<i>Width b</i>	0.0254	0.0254	0.0254	0.0254	<i>m</i>

Table 4.30 Properties cantilever beam with two thin piezoceramic PSI-5A-S3 sheets

Piezo	
Composition	Single sheet 5A-S3 (PZT)
Thickness	0.191 ± 0.013 <i>mm</i>
Length	54.5 <i>mm</i>
Width	54.5 <i>mm</i>
Distance form clamped side	30 <i>mm</i>
beam	
Composition	Aluminium
Thickness	1.6 <i>mm</i>
Length	356 <i>mm</i>
Width	54.5 <i>mm</i>

when both piezo-actuator is activated is reported in Fig. 4.42. It is possible to see that the presented model is able to give the same results of the commercial code ADINA. Moreover the two FEM code are able to capture the experimental results.

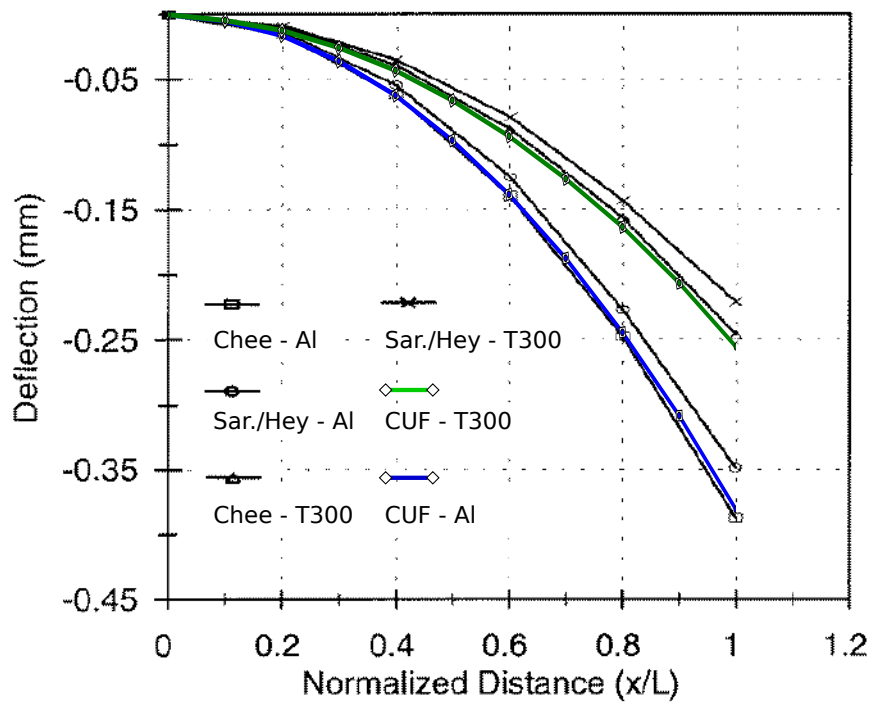


Figure 4.37 Actuator configuration. Deflection by piezoelectric actuation along the normalized length of the cantilever.

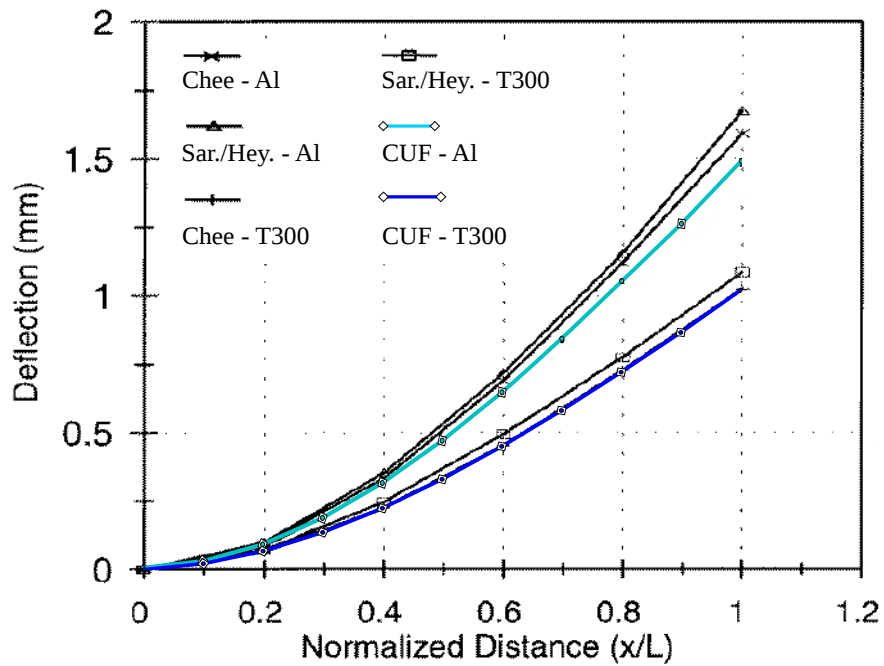


Figure 4.38 Sensor configuration. Deflection due to load at cantilever tip. The layer of piezoelectric material will act as a sensor.

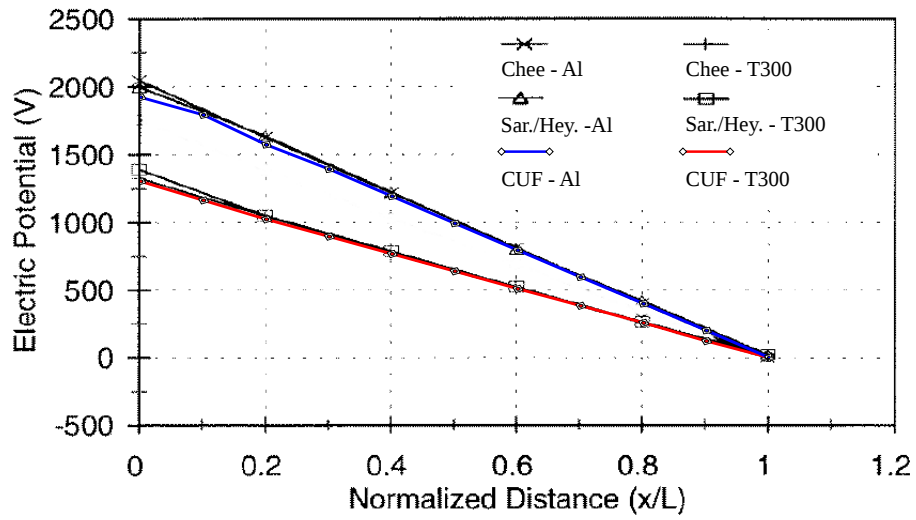


Figure 4.39 Sensor configuration. Voltage difference across the piezoelectric material as a function of normalized length of cantilever.

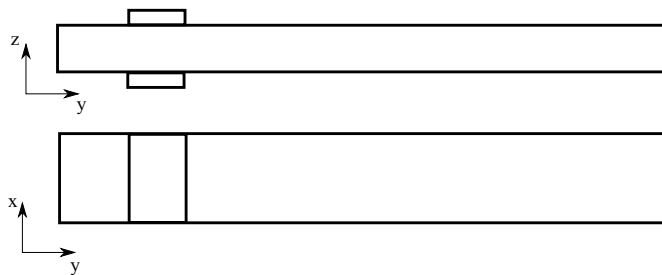


Figure 4.40 Cantilever beam with two thin piezoceramic PSI-5A-S3 sheets geometry

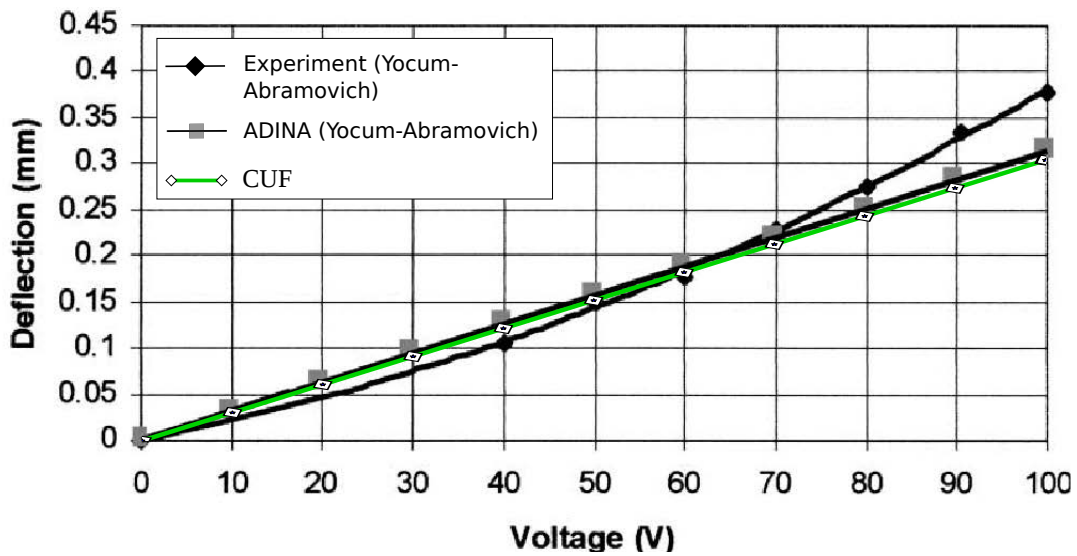


Figure 4.41 Deflection versus applied voltage, one piezo-patch activated.

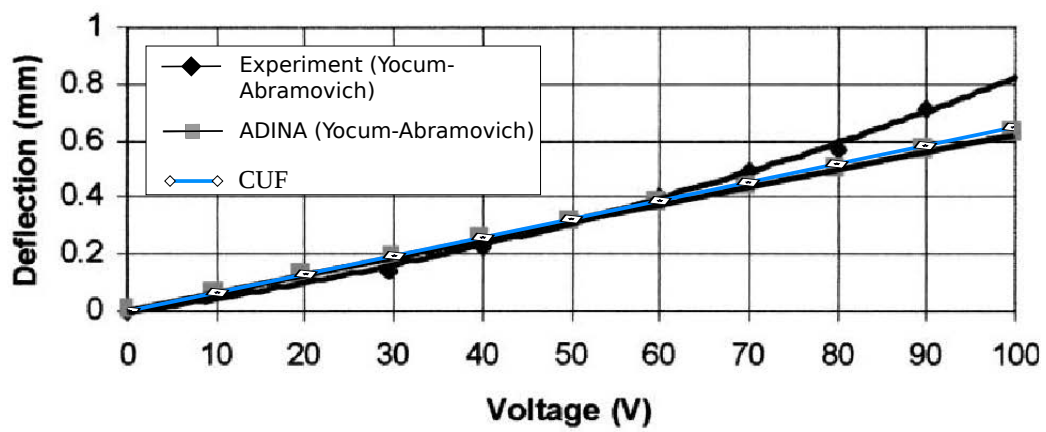


Figure 4.42 Deflection versus applied voltage, one piezo-patch activated.

Bibliography

- [1] G. Reich, B. Sanders, Introduction to morphing aircraft research., *Journal of Aircraft* 44.
- [2] D. Wagg, I. Bond, P. W. M. Friswell, *Adaptive Structures - Engineering Applications.*, John Wiley and Sons.
- [3] J. W. Smith, W. P. Lock, G. A. Payene, Variable-camber integration and operational performance of the afti/f-111 mission adaptive wing., *Nasa technical memorandum* 4370.
- [4] S. Powers, L. Webb, E. Friend, W. Lokos, Fligh test results from a supercritical mission adaptive wing with smooth variable camber, *Nasa technical memorandum* 4415.
- [5] S. Thornton, Reduction of structural loads using maneuver load control on the advanced fighter technology integration (afti)/f-111 mission adaptive wing, *NASA Technical Memorandum* 4526.
- [6] H. Monner, Realization of an optimized wing camber by using formvariable flap structures, *Aerosp. Sci. Technol.* 5 (2001) 445–455.
- [7] S. Kota, Compliant systems using monolithic mechanisms., *Smart Mater Bull.* 3 (2001) 7–10.
- [8] S. Kota, Compliant systems using monolithic mechanisms., *Smart Mater Bull.* 3 (2001) 7–10.
- [9] S. Kota, J. Hetricka, R. Osborna, D. Paul, E. Pendleton, P. Flick, C. Tilmann, Design and application of compliant mechanisms for morphing aircraft structures., *Smart Structures and Materials* 5054.
- [10] L. Campanile, S. Anders, Aerodynamic and aeroelastic amplification in adaptive belt-rib airfoils., *Aerospace Science and Technology* 9 (2005) 55–63.
- [11] C. Diaconu, P. Weaver, F. Mattoni, Concepts for morphing airfoil sections using bi-stable laminated composite structures., *Thin-Walled Struct* 46 (2008) 689–701.
- [12] F. Austin, M. Rossi, W. Nostrand, G. Knowles, Static shape control for adaptive wings., *AIAA Journal* 32 (1994) 1895–1901.
- [13] J. Joo, B. Sanders, Optimal location of distributed actuators within an in-plane multi-cell morphing mechanism., *Journal of Intelligent Material and System Structure* 20 (2009) 481–492.

- [14] J. Strelec, D. Lagoudas, M. Khan, J. Yen, Design and implementation of a shape memory alloy actuated reconfigurable airfoil., *Journal of Intelligent Material Systems and Structures* 14 (2003) 257–273.
- [15] Y. Dong, Z. Boming, L. Jun, A changeable aerofoil actuated by shape memory alloy springs., *Materials Science and Engineering: A* 485 (2008) 243–250.
- [16] T. Georges, V. Brailovski, D. Coutu, P. Terriault, Experimental validation of the 3d numerical model for an adaptive laminar wing with flexible extradors., *Proceedings of the international conference on shape memory and superelastic technol*, SMST, Tsukuba City, Japan.
- [17] J. Pinkerton, A feasibility study to control airfoil shape using thunder., *NASA Technical Memorandum* 4767.
- [18] R. Hellbaum, R. Bryant, R. Fox, J. Jalink, W. Rohrbach, Thin layer composite unimorph ferroelectric driver and sensor., *US Patent* 5.
- [19] D. Wang, J. Bartley-Cho, C. Martin, B. Hallam, Development of high-rate, large deflection, hingeless trailing edge control surface for the smart wing wind tunnel model., *Smart structures and materials 2001: industrial and commercial applications of smart structures technologies*.
- [20] R. Vos, R. Barrett, R. Breuker, P. Tiso, Post-buckled precompressed elements: a new class of control actuators for morphing wing uavs., *Smart Material Structures* 16 (2007) 191–926.
- [21] S. Lim, S. Lee, H. Park, K. Yoon, N. Goo, Design and demonstration of a biomimetic wing section using a lightweight piezo-composite actuator (lipca)., *Smart Material Structures* 14 (2005) 496–503.
- [22] S. Heinze, M. Karpel, Analysis and wind tunnel testing of a piezoelectric tab for aeroelastic control applications., *Journal of Aircraft* 43 (2006) 1799–1804.
- [23] A. Sofla, D. Elzey, H. Wadley, Two-way antagonistic shape actuation based on the one-way shape memory effect., *Journal of Intelligent Material System Structures* 19 (2008) 1017–1027.
- [24] A. Sofla, D. Elzey, H. Wadley, Cyclic degradation of antagonistic shape memory actuated structures., *Smart Material and Structures* 17.
- [25] D. Elzey, A. Sofla, H. Wadley, A bio-inspired, high-authority actuator for shape morphing structures., *Smart structures and materials 2003: active materials: behavior and mechanics*.
- [26] D. Elzey, A. Sofla, H. Wadley, A shape memory-based multifunctional structural actuator panel., *International Journal of Solids and Structures* 42 (2005) 1943–1955.

-
- [27] B. Berton, Shape memory alloys application: trailing edge shape control., NATO OTAN RTO-MP-AVT-141.
- [28] S. Yang, J. Han, I. Lee, Characteristics of smart composite wing with sma actuators and optical fiber sensors., *International Journal of Applied Electromagnetics and Mechanics* 23 (2006) 177–186.
- [29] S. Liu, W. Ge, S. Li, Optimal design of compliant trailing edge for shape changing., *Chinese Journal of Aeronautics* 21 (2008) 187–192.
- [30] E. Carrera, Developments, ideas and evaluations based upon the reissner’s mixed theorem in the modeling of multilayered plates and shells, *Applied Mechanics Review* 54 (4) (2001) 301–330.
- [31] S. Lekhnitskii, *Anisotropic Plates*, 2nd Edition, Bordon and Breach, 1968.
- [32] S. Ambartsumian, Contributions to the theory of anisotropic layered shells, *Applied Mechanics Review* 15 (1962) 245–249.
- [33] S. Ambartsumian, *Theory of anisotropic shells*, translated from russian, nasa ttf–118 Edition, Fizmatzig, Moskwa, 1964.
- [34] S. Ambartsumian, *Theory of anisotropic plates*, translated from russian by t. cheron and edited by j.e. ashton Edition, Tech. Pub. Co, 1969.
- [35] S. Ambartsumian, *Fragments of the theory of anisotropic shells*, World Scientific Publishing Co, Singapore, 1991.
- [36] E. Grigolyuk, F. Kogan, State of art of the theory of multilayer shells, *International Applied Mechanics* 8 (6) (1972) 583–595.
- [37] A. Leissa, A review of laminated composite plate buckling, *Applied Mechanics Review* 40 (5) (1987) 575–592.
- [38] L. Librescu, J. Reddy, A critical review and generalization of transverse shear deformable anisotropic plates, *Euromech Colloquium 219, Kassel, Sept 1986, Refined dynamical Theories of Beams, Plates and Shells and their Applications*, Elishakoff and Irretier (1987) 32–34.
- [39] E. Grigolyuk, G. Kulikov, General directions of the development of theory of shells, *Mekhanika Kompozitnykh Materialov* 24 (1988) 287–298.
- [40] R. Kapania, S. Raciti, Recent advances in analysis of laminated beams and plates, *American Institute of Aeronautics and Astronautics Journal* 27 (1989) 923–946.
- [41] R. Kapania, A review on the analysis of laminated shells, *Journal of Pressure Vessel Technology* 111 (1989) 88–96.
- [42] V. Vasilive, S. Lur’e, On refined theories of beams, plates and shells, *Journal of Composite Materials* 26 (1992) 422–430.

- [43] A. Noor, W. Burton, Assessment of shear deformation theories for multilayered composite plates, *Applied Mechanics Review* 41 (1989) 1–18.
- [44] A. Noor, W. Burton, Assessment of computational models for multilayered composite shells, *Applied Mechanics Review* 43 (1990) 67–97.
- [45] A. Noor, S. Burton, C. Bert, Computational model for sandwich panels and shells, *Applied Mechanics Review* 49 (1996) 155–199.
- [46] G. Jemlelita, On kinematical assumptions of refined theories of plates: A survey, *Journal of Applied Mechanics* 57 (1990) 1080–1091.
- [47] J. Reddy, D. Robbins, Theories and computational models for composite laminates, *Applied Mechanics Review* 47 (1994) 147–165.
- [48] S. Lur'e, N. Shumova, Kinematic models of refined theories concerning composite beams, plates and shells, *Mechanics of Composite Materials* 32 (1996) 422–240.
- [49] Y. Grigorenko, Approaches to numerical solution of linear and nonlinear problems in shell theory in classical and refined formulations, *International Applied Mechanics* 32 (6) (1996) 409–442.
- [50] Y. Grigorenko, A. Vasilenko, Solution of problems and analysis of the stress strain state of non-uniform anisotropic shells (survey), *International Applied Mechanics* 33 (1997) 851–880.
- [51] H. Altenbach, Theories for laminated and sandwich plates. a review, *International Applied Mechanics* 34 (1998) 243–252.
- [52] E. Carrera, Historical review of zig-zag theories for multilayered plates and shells, *Applied Mechanics Review* 56 (2003) 287–308.
- [53] J. Reddy, *Mechanics of laminated composite plates and shells. Theory and Analysis*, CRC Press, 2004.
- [54] M. Qatu, *Vibration of Laminated Shells and Plates*, Elsevier, 2004.
- [55] E. Carrera, Theories and finite elements for multilayered plates and shells: A unified compact formulation with numerical assessment and benchmarking, *Archives of Computational Methods in Engineering* 10 (2003) 215–197.
- [56] E. Carrera, Mixed layer-wise models for multilayered plates analysis, *Composite Structures* 43 (1998) 57–70.
- [57] E. Carrera, Evaluation of layer-wise mixed theories for laminated plates analysis, *AIAA Journal* 26 (1998) 830–839.
- [58] E. Carrera, Transverse normal stress effects in multilayered plates, *Journal of Applied Mechanics* 66 (1999) 1004–1012.

- [59] E. Carrera, L. Demasi, Multilayered finite plate element based on reissner mixed variational theorem. part i: Theory., *International Journal for Numerical Methods in Engineering* 55 (2002) 191–231.
- [60] E. Carrera, L. Demasi, Multilayered finite plate element based on reissner mixed variational theorem. part ii: Numerical analysis., *International Journal for Numerical Methods in Engineering* 55 (2002) 253–296.
- [61] E. Carrera, M. Petrolo, Guidelines and recommendations to construct refinements of classical theories for metallic and composite plates, *AIAA Journal*.
- [62] G. Kirchhoff, *Über das Gleichgewicht und die Bewegung einer elastischen Scheibe*, *J. Angew. Math.* 40 (1850) 51–58.
- [63] E. Reissner, The effect of transverse shear deformation on the bending of elastic plates, *Journal of Applied Mechanics* 12 (1945) 51–58.
- [64] Mindlin, Influence of rotatory inertia and shear in flexural motions of isotropic elastic plates, *Journal of Applied Mechanics* 18 (1951) 1031–1036.
- [65] S. Tsai, *Composites Design*, 4th Edition, Think Composites, Dayton, 1988.
- [66] E. Carrera, S. Brischetto, Analysis of thickness locking in classical, refined and mixed theories for layered shells, *Composite Structures* 85 (2008) 83–90.
- [67] E. Carrera, S. Brischetto, Analysis of thickness locking in classical, refined and mixed multilayered plate theories, *Composite Structures* 82 (2008) 549–562.
- [68] B. Pandya, T. Kant, Finite element analysis of laminated composite plates using high-order displacement model, *Composites Science and Technology* 32 (1988) 137–155.
- [69] T. Kant, B. Manjunatha, An unsymmetric frc laminate $c\hat{A}^\circ$ finite element model with 12 degrees of freedom per node, *Eng Comput* 5 (3) (1988) 292–308.
- [70] T. Kant, Numerical analysis of thick plates, *Comput Meth Appl Mech Eng* 31 (1982) 1–18.
- [71] E. Dvorkin, K. Bathe, A continuum mechanics based four-node shell element for general nonlinear analysis, *Eng. Computations* 1 (1984) 77–88.
- [72] E. Carrera, C. Cinefra, P. Nali, Mlc technique extended to variable kinematic multilayered plate elements, *Composite Structures* 92 (2010) 1888–1895.
- [73] M. Fonseca, P. Fleming, Genetic algorithm for multiobjective optimization: Formulation, discussion and generalization, *Genetic Algorithms : Proceedings of the Fifth International Conference*.
- [74] *Advanced materials and smart structures*.
- [75] *Fundamentals of piezoelectricity*.

- [76] J. Reddy, *Mechanics of laminated composite plates and shells. Theory and Analysis*, 2nd Edition., CRC Press, 2004.
- [77] E. Carrera, G. Giunta, Refined beam theories based on Carrera's unified formulation., *International Journal of Applied Mechanics* 2(1).
- [78] E. Carrera, M. Petrolo, On the effectiveness of higher-order terms in refined beam theories., *International Journal of Applied Mechanics* 78(2).
- [79] E. Carrera, G. Giunta, P. Nali, M. Petrolo, Refined beam elements with arbitrary cross-section geometries., *Computers and Structures* 88(5-6) (2010) 283–293.
- [80] E. Carrera, M. Petrolo, P. Nali, Unified formulation applied to free vibrations finite element analysis of beams with arbitrary section., *Shock and Vibration* 18(3) 485–502.
- [81] E. Carrera, M. Petrolo, A. Varello, Advanced beam formulations for free vibration analysis of conventional and joined wings., *Journal of Aerospace Engineering*.
- [82] E. Carrera, M. Petrolo, E. Zappino, Performance of CUF approach to analyze the structural behavior of slender bodies., *Journal of Structural Engineering*.
- [83] E. Onate, *Structural Analysis with the Finite Element Method: Linear Statics*, Volume 1.
- [84] C. Chee, L. Tong, G. Steven, A mixed model for composite beams with piezoelectric actuators and sensors, *Smart material and structures*.
- [85] H. Tzou, R. Ye, Analysis of piezoelectric structures with laminated piezoelectric triangle shell elements, *AIAA Journal*.
- [86] D. Valey, S. Rao, Two-dimensional finite element modeling of composites with embedded piezoelectrics, *Collection Tech. Papers Proc. AIAA/ASME/ASCE/AHS/ASC Structures, Structural Dynamics and Materials Conf. 5* (1994) 2629–2633.
- [87] W. Hwang, H. Park, Finite element modelling of piezoelectric sensors and actuators, *AIAA Journal*.
- [88] D. Sarvanos, P. Heyliger, Coupled layerwise analysis of composite beams with embedded piezoelectric sensors and actuators, *Journal of Intelligent Material System and Structures*.
- [89] J. N. R. D. Robbins, Analysis of piezoelectrically actuated beams using a layer-wise displacement theory, *Computer and Structures* 41 (1991) 265–279.
- [90] D. A. Sarvanos, Mixed laminate theory and finite element for smart piezoelectric composite shell structures, *AIAA Journal* 35 (1997) 1327–1333.
- [91] M. Yocum, H. Abramovich, Static behaviour of piezoelectric actuated beams, *Computes and Structures* 80 (2002) 1797–1808.